Impact of Point Defects on Reaction Kinetics of Systematically Doped Ceria

Von der Fakultät Chemie der Universität Stuttgart
Zur Erlangung der Würde eines

Doktors der Naturwissenschaften (*Dr. rer. nat.*)
Genehmigte Abhandlung

Vorgelegt von

MAXIMILIAN SCHAUBE
aus Herzlake

Hauptberichter:	Prof. Dr. Joachim Maier
Mitberichter:	Prof. Dr. Rainer Niewa
Prüfungsvorsitzender:	Prof. Dr.-Ing. Elias Klemm
Tag der Einreichung:	24.10.2019
Tag der Disputation:	31.01.2020

Max-Planck-Institut für Festkörperforschung

Stuttgart, **2020**

Erklärung

Die vorliegende Dissertation wurde vom Autor selbstständig in der Abteilung von Prof. J. Maier am Max-Planck-Institut für Festkörperforschung im Zeitraum von November 2015 bis Oktober 2019 angefertigt. Der Inhalt ist die eigene Arbeit des Autors -Ausnahmen sind gekennzeichnet- und wurde noch nicht zur Erlangung einer Qualifikation oder eines Titels an einer akademischen Institution eingereicht.

Declaration

This dissertation was written by the author himself in the department of Prof. J. Maier at the Max Planck Institute for Solid State Research in the period from November 2015 to Oktober 2019. The content is the author's own work - exceptions are marked - and have not yet been submitted to an academic institution for a qualification or title.

Stuttgart, October 24th 2019 Maximilian Schaube

ACKNOWLEDGEMENTS

This work was not possible to conduct without the expertise and help of several people to which I would like to express my sincere and honest gratitude:

Prof. Dr. Joachim Maier, who gave me the opportunity to do my Ph.D on this project in impressive research conditions in his department. Thanks for this great challenge and the opportunity.

Dr. Rotraut Merkle, my day-to-day supervisor. I will never forget her patience, her unbelievable knowledge, her advices, and her dedication to science.

Prof. Dr. Rainer Niewa and Prof. Dr. Elias Klemm for finding time reviewing this dissertation and being on my examination committee and Dr. Thomas Keller for being my external thesis advisor.

Dr. Helga Hoier for conducting all XRD measurements. Annette Fuchs, who synthesized Fe–doped strontium titanate, conducted BET measurements and SEM imaging. Kathrin Küster, for performing XPS measurements. Tolga Acartürk, who conducted ToF-SIMS investigations. Samir Hammoud, for checking the cation stoichiometry of my samples by ICP-OES. Wilfried Sigle, for performing TEM-EDX investigations. Armin Schulz, who conducted Raman spectroscopy. The technicians Udo Klock, Florian Kaiser and Armin Sorg, who were always available and helpful in time of need. Uwe Traub, who helped me with IT-related issues. Barbara Baum, who cut and polished a lot of my pellets. The glass-blower workshop for the realization of many glass reactors and vessels. Dr. Hans-Georg Libuda, Sofia Weiglein and finally Madeleine Burkhardt for administrative support.

TABLE OF CONTENTS

KURZFASSUNG

In der vorliegenden Arbeit wird das Zusammenspiel zwischen ionischen sowie elektronischen Punktdefekten und der katalytischen Aktivität für heterogene Reaktionen experimentell untersucht. Es werden insbesondere die Einflüsse von Sauerstoffleerstellen, Elektronen oder Elektronenlöchern auf die Kinetik der Sauerstoffaustauschreaktion, Kohlenstoffmonoxid– und Methanoxidation behandelt. Die Reaktionskinetik wurde an circa 30 unterschiedlich dotierten Proben (Cerdioxid, Strontiumtitanat und Zirkondioxid) untersucht, wobei der Schwerpunkt auf Cerdioxid als Modellmaterial liegt. Grundlegende Zusammenhänge zwischen katalytischer Aktivität und Defektchemie konnten dadurch aufgeklärt werden. Sie unterstreichen die wichtige Rolle der Defektchemie in der heterogenen Katalyse.

Für die Sauerstoffaustauschkinetik wurde ein Aufbau für den gepulsten $^{16}O/^{18}O$ Isotopenaustausch entwickelt und optimiert. Dieser Aufbau ermöglicht ein vergleichsweise schnelles Screening und damit eine systematische Untersuchung der Abhängigkeit der Sauerstoffaustauschkinetik von Punktdefekten und Sauerstoffpartialdrücken. Die Kohlenstoffmonoxid- und Methanoxidation wurden ebenfalls in Festbettreaktoren im gleichen Versuchsaufbau untersucht. Die katalytische Aktivität eines Metalloxids hängt stark von den herrschenden Oberflächenbedingungen ab. Daher ist es extrem wichtig Messreihen zu erstellen bei denen die Proben unter gleichen Bedingungen synthetisiert, vorbereitet und gemessen werden. Dies bildet eine zuverlässige Grundlage für konsistente und weiterführende Schlussfolgerungen.

Die Behandlung der Volumen-Defektchemie von dotiertem Cerdioxid folgt einer ausführlichen Diskussion des zu erwarteten defektchemischen Regimes an der Probenoberfläche. Thermogravimetrische und Raman-spektroskopische Messungen zeigen eine klare Korrelation der Volumen-Sauerstoffleerstellenkonzentration mit der Gd- und Pr-Konzentration in dotiertem Cerdioxid. In Nb-dotiertem Cerdioxid hingegen sind keine Sauerstoffleerstellen vorhanden. Zusätzliches Dotieren von Gd- und Pr-dotiertem Cerdioxid mit Nb verringert die Leerstellenkonzentration im Vergleich zu Proben ohne Nb. Oberflächenempfindliche H_2O- und CO_2-Sorptionsexperimente zeigen, dass die Adsorbatkonzentration eindeutig mit Art und Menge des Dotierkations korreliert. Die Konzentration von adsorbiertem H_2O und CO_2 korreliert klar mit der Sauerstoffleerstellenkonzentration in Gd- und Pr-dotiertem Cerdioxid (GDC, PDC). PDC und GDC zeigen identische CO_2 Adsorbat-konzentrationen, während CO_2- und H_2O- Adsorption bei Nb-dotiertem Cerdioxid

(NDC) kaum stattfindet. Bei hohen Pr Konzentrationen wurde in Pr-dotiertem Cerdioxid und Zirkondioxid die Bildung eines Pr-Störstellenbandes mittels UV-Vis Spektroskopie beobachtet.

Die Gleichgewichtsaustauschrate der Sauerstoffeinbaureaktion korreliert eindeutig mit der Art des Dotierkations und seiner Konzentration. Die höchsten Reaktionsraten wurden gemessen, wenn sowohl Sauerstoffleerstellen als auch redox-aktive Zentren/elektronische Ladungsträger verfügbar waren. Dieser Befund wird dadurch gestützt, dass zusätzliches Dotieren von PDC oder GDC mit Nb die Gleichgewichtsaustauschrate auf das Niveau von undotiertem Cerdioxid senkt. Ein Mechanismus der Sauerstoffeinbaureaktion konnte abgeleitet werden, in dem molekulare Sauerstoffspezies im geschwindigkeitsbestimmenden Schritt (*rds*) beteiligt sind und Sauerstoffleerstellen in *oder* vor dem *rds* auftreten. Entweder ist das Zusammentreffen von adsorbiertem 0_2^- mit einer Sauerstoffleerstelle, der anschließende Einbau des 0_2^- in eine Sauerstoffleerstelle, oder die Leerstellen-unterstützte Dissoziation der molekularen adsorbierten Sauerstoffspezies ratenlimitierend.

Der stärkste Anstieg der Gleichgewichtsaustauschrate der Sauerstoffeinbau-reaktion wurde bei PDC festgestellt. Im Vergleich zu undotiertem Cerdioxid ist die Gleichgewichtsaustauschrate für 20 mol% Pr-dotiertes Cerdioxid bei 700 °C um einen Faktor von fast 100000 erhöht. Dieser steile Anstieg ist auf die Kombination von hoher Sauerstoffleerstellenkonzentration und erleichtertem Elektronentransfer zu adsorbiertem Sauerstoff zurückzuführen. Letzteres wird durch die Bildung eines Pr-Störstellenbandes begünstigt. Angesichts der ähnlichen Defektchemie verhält sich Tb-dotiertes Cerdioxid (TDC) analog zu PDC. Zusammen mit der klaren Korrelation der Gleichgewichtsaustauschrate mit der Fe- und Pr-Konzentration in Fe-dotiertem Strontiumtitanat und Pr-dotiertem Zirkoniumdioxid wird die Bedeutung der redox-aktiven Dotierung (bzw. Kationen mit leichte Valenzwechsel) für eine verbesserte Sauerstoffaustauschaktivität verdeutlicht.

Bei höher dotiertem PDC und TDC wird im O_2 Isotopenaustauschexperiment kein $^{34}O_2$ gebildet. Dieser Befund deutet auf eine schnellere Sauerstoffionen-diffusion im Vergleich zu GDC hin. Dies wurde durch ^{18}O Diffusionsexperimente in keramischen Proben bestätigt. Die Erhöhung des Sauerstoffdiffusionskoeffizienten hängt wahrscheinlich mit dem Valenzwechsel in Pr- oder Tb-dotiertem Cerdioxid zusammen. Es wird angenommen, dass sich entlang der $Pr^{3+/4+}$/$Tb^{3+/4+}$ Plätze ein schneller Sauerstoffmigrationspfad bildet, da der Valenzwechsel, der auch den Kationradius verändert, zu verminderten Migrationsbarrieren führt.

Darüber hinaus wurde gezeigt, dass die Oberflächenreaktionsrate viel empfindlicher als Volumen-Eigenschaften auf experimentelle Details wie beispielsweise Oberflächenvergiftungen oder katalytische Verunreinigungen reagiert. Dies unterstreicht die Notwendigkeit, systematisch dotierte Probenreihen zu untersuchen welche nach der gleichen Methode hergestellt und unter identischen experimentellen Bedingungen behandelt wurden.

Die Analyse der CO-Oxidationskinetik ergab, dass die Redox-Aktivität des Katalysators entscheidend für eine hohe Reaktionsrate ist. Interessanterweise sind die intrinsische Redox-Aktivität und die Sauerstoffleerstellenkonzentration an der Oberfläche von undotiertem Cerdioxid bereits so hoch, dass Pr- oder Gd-Dotierung die Reaktionsrate kaum weiter steigert. Im Gegensatz dazu verringern das Fehlen von Redox-Aktivität in Yttrium-stabilisiertem Zirkoniumdioxid und die verminderte Reduktionsfähigkeit in Donor-dotiertem NDC die Reaktionsrate. Aufgrund der Konkurrenz von Reduktion (durch CO) und Re-oxidation (durch O_2) bildet sich innerhalb der Katalysatorpartikel ein kinetisch bestimmter verminderter effektiver Sauerstoffpartialdruck aus, der mit abnehmender Konzentration der Dotierkationen stärker ausgeprägt ist. Dies beschleunigt die Sauerstoffeinbaureaktion, bis die Reaktionsraten der CO-Oxidation und Sauerstoffeinbaureaktion ausgeglichen sind. Es wurde der Schluss gezogen, dass der ratenbestimmende Schritt der CO-Oxidation die Reaktion von adsorbiertem CO^+ mit Oberflächen-Gittersauerstoff beinhaltet, gefolgt von einer schnellen CO_2-Desorption und Bildung einer Sauerstoffleerstelle.

Die Methanoxidationskinetik von dotiertem Cerdioxid ist im Vergleich zur CO-Oxidation und Sauerstoffeinbaureaktion langsamer. Die CH_4-Oxidationsrate hängt nur mäßig von der Konzentration der Dotierkationen ab. Es wurde kein signifikanter Unterschied zwischen Gd- und Pr-Dotierung gefunden. Dies deutet darauf hin, dass der Valenzwechsel/Reduktionsfähigkeit von Pr die CH_4-Oxidation nicht weiter fördert. Die Dotierung von Cerdioxid mit Gd oder Pr hat jedoch einen Einfluss auf die Elektronenlochkonzentration. Die Elektronenlöcher treten hier als reaktive Spezies im oder vor dem ratenbestimmenden Schritt auf, welcher die Spaltung der ersten C-H Bindung ist. Im Gegensatz zur CO-Oxidation entsteht in den Katalysatorpartikeln kein verminderter effektiver Sauerstoffpartialdruck. Dies lässt sich auf die wesentlich langsamere Methanoxidationskinetik im Vergleich zur schnelleren Sauerstoffeinbaukinetik zurückführen.

ABSTRACT

This thesis investigates the interplay between ionic and electronic point defects such as oxygen vacancies, electrons or holes, and the catalytic activity for heterogeneous reactions, in particular oxygen exchange, carbon monoxide and methane oxidation. The importance of point defects for reaction kinetics is demonstrated for more than 30 differently doped ceria, strontium titanate and zirconia samples, whereby the focus is set in doped ceria. Fundamental relationships between catalytic activity and defect chemistry are elucidated emphasizing the importance of defect chemistry in heterogeneous catalysis.

For oxygen exchange kinetics, a setup for pulsed $^{16}O/^{18}O$ isotope exchange (PIE) was assembled and optimized. This setup allows for a comparably fast screening and thus systematic investigation of the dependence of oxygen exchange kinetics on point defects. Carbon monoxide and methane oxidation were studied in fixed bed reactors with the same experimental setup. Since the catalytic activity of an oxide is extremely sensitive to the exact surface conditions, it was important to establish a consistent data set from samples prepared and measured under the same experimental conditions as the basis for further conclusions.

First, the bulk defect chemistry of doped ceria is reviewed, followed by an extensive discussion of expected surface defect chemical regimes. Thermogravimetry and Raman spectroscopy yield clear correlation of the bulk oxygen vacancy concentration to Gd and Pr concentration in doped ceria. Nb doping leads to an absence of oxygen vacancies and additional co-doping of Gd– and Pr–doped ceria with Nb decreases the vacancy concentration when compared to samples without Nb. Surface sensitive H_2O and CO_2 sorption experiments show that the adsorbate concentration clearly correlates to the dopant type and amount. The amount of adsorbed H_2O and CO_2 correlates with the concentration of surface oxygen vacancies in Gd–doped ceria (GDC) and Pr–doped ceria (PDC). PDC and GDC show identical adsorbed CO_2 concentrations, while CO_2 and H_2O adsorption is not favorable on Nb–doped ceria (NDC). The formation of a Pr impurity band in Pr–doped ceria and zirconia at high Pr concentration was verified by UV-Vis spectroscopy.

The equilibrium exchange rate of oxygen incorporation clearly correlates with the dopant concentration, and highest reaction rates were found when both oxygen vacancies and redox-active centers/electronic carriers are available. Additional doping of PDC/GDC with Nb decreased the equilibrium exchange rate, supporting

this interpretation. A mechanism of oxygen incorporation was deduced, in which molecular oxygen is involved in the rate–determining step (*rds*) and oxygen vacancies appear in *or* before the *rds*. Either the encounter of adsorbed O_2^- and oxygen vacancies, the subsequent incorporation of O_2^- into an oxygen vacancy, or the vacancy assisted dissociation of molecular oxygen species is rate-limiting.

The strongest increase of the equilibrium exchange rate was observed on PDC. At 700 °C, 20 mol% Pr–doped ceria accelerates the equilibrium exchange rate by five orders of magnitude compared to undoped ceria. This steep increase is assigned to the combination of high oxygen vacancy concentration with facilitated electron transfer to adsorbed oxygen due to the formation of a Pr impurity band. Due to its closely related defect chemical behavior compared to PDC, Tb–doped ceria (TDC) behave similar. Together with the clear correlation of the equilibrium exchange rate with Fe and Pr concentration in Fe–doped strontium titanate and Pr–doped zirconia, this emphasizes the importance of doping with redox-active cations (or rather cations with facilitated valance change between 3+ and 4+) for higher oxygen exchange activity. The absence of $^{34}O_2$ formation in case of highly doped PDC and TDC indicates faster oxygen ion diffusivity compared to GDC, probably related to the easy valance change of Pr or Tb in doped ceria, which was confirmed by isothermal isotope exchange line profiling. It is hypothesized that an oxygen migration path forms along a percolating path close to $Pr^{3+/4+}$/$Tb^{3+/4+}$ in which the facile valance change, which also changes the dopant radius leads to decreased migration barriers. Furthermore, it was shown that the surface reaction rate is much more sensitive to experimental details like surface poisoning or catalytically impurities than bulk properties, emphasizing the importance to investigate a systematically doped set by the same method, and in identical experimental conditions.

The investigation of the CO oxidation kinetics revealed that the redox-activity of the catalyst is crucial for good CO oxidation performance. Interestingly, the intrinsic redox-activity and surface oxygen vacancy concentration of undoped ceria are already sufficiently high, such that Pr– or Gd–doping hardly increase the reaction rate. In contrast, absence of redox-activity in yttria–stabilized zirconia and decreased reducibility in donor–doped NDC decreases the rate. Due to the competition of reduction by CO and re–oxidation, a kinetically determined decreased effective oxygen partial pressure prevails inside the catalyst particles, which is more pronounced with decreasing dopant concentration. This accelerates the oxygen incorporation reaction until the CO oxidation and O incorporation

reactions are balanced. It was concluded that the rate–determining step of the CO oxidation involves the reaction of adsorbed CO^+ with surface lattice oxygen followed by fast CO_2 desorption and oxygen vacancy formation.

The methane oxidation kinetics of doped ceria is slower when compared to the CO oxidation and oxygen incorporation. The CH_4 oxidation rate depends moderately on the dopant concentration. No significant difference between Gd– and Pr–doping was found, indicating that the reducibility of Pr does not further promote CH_4 oxidation. Gd and Pr have an impact on the electron hole concentration, which is assigned here as a reactive species in *or* before the *rds* of the first C-H bond cleavage. In contrast to CO oxidation, inside the catalyst particles no decreased effective oxygen partial pressure develops, which is attributed due to the lower methane oxidation rate compared to the rate of oxygen incorporation.

ABBREVIATIONS AND SYMBOLS

Abbreviations

Ac	Acceptor dopant
BET	Brunauer-Emmet-Teller
C	Check valve
CA	Citric acid
CPE	Constant phase element
d.c.	Direct current
EDX	Energy–dispersive X–ray spectroscopy
EG	Ethylene glycol
GDC	Gd–doped ceria
GNDC	Gd and Nb double–doped ceria
H	Heater
ICP-OES	Inductively plasma optical emission spectroscopy
M1, M2	Mechanism 1 and 2
Me	Metal
MFC	Mass flow controller
MHRS	Multifunctional heterogeneous reaction setup
MIEC	Mixed ionic and electronic conductor
MP	Membrane pump
MS	Mass spectrometer
NDC	Nb–doped ceria
P	Pressure probe
PBR	Plug flow reactor
PDC	Pr–doped ceria
PDZ	Pr–doped zirconia
PIE	Pulsed isotope exchange
PNDC	Pr and Nb double–doped ceria
R	Rotameter
rds	Rate-determining step
EIS	Electrochemical impedance spectroscopy
ESR	Electron spin resonance
FT–IR	Fourier-transform infrared spectroscopy
SCL	Space charge layer
SEM	Scanning electron microscopy
SFT	Iron–doped strontium titanate
SIMS	Secondary ion mass spectrometry
SOFC	Solid oxide fuel cell
SPS	Spark plasma sintering
TDC	Tb–doped ceria
TEM	Transmission electron microscopy
TPD	Temperature programmed desorption
V	Valve
XPS	X–ray photoelectron spectroscopy
XRD	X–ray diffraction
YSZ	Yttrium stabilized zirconia

Symbols

A	Peak area
a, b, c	Lattice constants
B	Scattering coefficient

c	Concentration
C	Capacitance
C_B	Bulk capacitance
C_{chem}	Chemical capacitance
C_{GB}	Grain boundary capacitance
$c_{j,s}$	Surface concentration of defect j
$c_{j,s}$	Bulk concentration of defect j
D^*	Oxygen ion tracer diffusion coefficient
D_{V}	Oxygen vacancy diffusion coefficient
δ	oxygen non-stoichiometry
$\Delta\varphi$	Space charge potential
e	Elementary charge
e'	Electron according to Kröger-Vink notation
E_a	Activation energy
ε_0	Vacuum permittivity
ε_{r}	Relative permittivity
f	Fraction
${}^{32}f_{\mathrm{g}}$, ${}^{34}f_{\mathrm{g}}$, ${}^{36}f_{\mathrm{g}}$	Molar gas phase fraction of $^{32}O_2$, $^{34}O_2$ and $^{36}O_2$
${}^{18}f_{\mathrm{g}}$, ${}^{18}f_{\mathrm{s}}$	Molar fraction of ^{18}O in gas (g) or solid (s) phase
F	Faraday constant
$\mathcal{F}$	Tracer correlation factor
γ	Pre-exponential factor
$h^{\bullet}$	Electron hole according to Kröger-Vink notation
H_r	Enthalpy of reduction
I	Ion current
Im	Imaginary part of the resistance
k	Reaction rate constant
k_B	Boltzmann's constant
k^*	Effective tracer surface exchange reaction rate constant
k^{δ}	Effective chemical surface exchange reaction rate constant
k^q	Effective electrical surface exchange reaction rate constant
K	Equilibrium constant
κ	Absorption coefficient
l_0	Characteristic length
L	Thickness
m	Influence of point defects on the overall oxygen partial pressure exponent n
$M(t)$	Accumulated ^{16}O in the sample at time t
$\mathrm{Me}_{\mathrm{Me}}^{\bullet}$	Metal cation on a Metal lattice site, positively charged relative to the perfect lattice, according to Kröger-Vink notation
$\mathrm{Me}_{\mathrm{Me}}^{\mathrm{x}}$	Metal cation on a Metal lattice site, neutral relative to the perfect lattice, according to Kröger-Vink notation
$\mathrm{Me}_{\mathrm{Me}}'$	Metal cation on a Metal lattice site, negatively charged relative to the perfect lattice, according to Kröger-Vink notation
$\tilde{\mu}_{\mathrm{b}}$	Electrochemical potential of a bulk defect
μ_j°	Standard electrochemical potential of defect j
μ_{O}	Gas phase oxygen chemical potential
$\tilde{\mu}_{\mathrm{s}}$	Electrochemical potential of a surface defect
n_j	Oxygen partial pressure exponent of the defect species j

N	Normalized peak area
ν	Volume flow rate
ω	Peak frequency
p	Partial pressure
P	The exponent of CPE
$p(O_2)_{\mathrm{eff}}$	Kinetically determined decreased effective $p(O_2)$
p_{sat}	Saturating pressure
φ_{s}	Electrostatic potential at the interface
φ_{b}	Electrostatic potential in the bulk
Q	The admittance constant of CPE
r_{p}	Mean particle radius
R	Universal gas constant or resistance
R_∞	Absolute reflectance of an infinitely thick sample
$\Re_0$	Equilibrium exchange rate
$R_{\mathrm{CH_4}}$	Apparent reaction rate of CH_4 oxidation
R_{CO}	Apparent reaction rate of CO oxidation
R_B	Bulk resistance
$\Re_{\mathrm{da}}$	Exchange rate of dissociative adsorption
R_{GB}	Resistance of the grain boundary
$\Re_{\mathrm{i}}$	Exchange rate of incorporation adsorption
R_{rds}	Reaction rate of the rate–determining step
Re	Real part of the resistance
ρ	Charge density
S	Total surface area
S_r	Entropy of reduction
σ	General conductivity
σ_{b}	Bulk conductivity
σ_{e}	Electronic conductivity
σ_{ion}	Ionic conductivity
$\sigma_{\mathrm{GB}}^{\mathrm{spec}}$	Specific grain boundary conductivity
σ_{Pr}	Conductivity due to small polaron hopping in PDC
σ_{tot}	Total conductivity (sum of all conductivities)
σ_{V}	Oxygen vacancy conductivity
Σ_{SCL}	Total charge within the space charge layer
T	Temperature
T_{R}	Reference temperature where no oxygen isotope exchange occurs
τ	Mean residence time of the pulse in the packed bed
θ	Adsorbate surface concentration
u_{V}	Mobility of oxygen vacancies
V	Volume
$\mathrm{V}_{\mathrm{O}}^{\bullet\bullet}$	Oxygen vacancy according to Kröger–Vink notation
w	Thermodynamic factor
x	Distance
X_i	Conversion of species i
Z	Complex Impedance

1 INTRODUCTION

Heterogeneous reactions of gases at a solid catalyst or reaction partner occur at the surface. The surface of a solid is a highly complex defective two-dimensional structure. Even on a hypothetical perfect surface plane of a metal oxide, oxygen ions are bound less strongly and are more active for undergoing reactions compared to bulk oxygen. Also higher-dimensional imperfections such as dislocations, kinks, or steps further decrease the coordination of surface atoms and increase their reactivity. Moreover, positive and negative charge carriers are not found in equal number near the surface, implying the formation of a surface space charge.

Point defects represent centers of increased local free energy and thus enhanced reactivity. For example, in metal oxides a surface oxygen vacancy is not only a site where oxygen can enter the material. Since it is surrounded by cations, it represents a strongly acidic center. Generally, such ionic defects represent strong acid-base active centers[1]. All in all, it is not surprising that physicochemical properties of surfaces differ strongly from bulk properties.

One of the earliest studies, which investigates the impacts of defect chemistry (especially ionic point defects) on heterogeneous catalysis was conducted by Wagner und Simkovich[2] in 1962. They performed dehydrohalogenating of alkyl halides on the surface of AgCl. It was demonstrated that doping of AgCl with $CdCl_2$ increases the silver vacancy concentration, which accelerates the reaction kinetics whereby electronic defects are minimized due to the insulating character of AgCl.

At present, heterogeneous catalysis occupies almost 80 % of the global market share[3] in terms of base and fine chemicals production and pharmaceutical compounds, emphasizing the importance of interfacial reactions and influences of surface point defects. But studies which intensively exploit fundamental influence of both electronic and ionic point defects on heterogeneous reaction kinetics are rare, and hardly cover a systematically varied set of materials suggesting the underestimated role of defect chemistry in the catalysis community which is also addressed in refs[4-6].

Therefore, this work aims to elucidate fundamental relationships between catalytic activity and defect chemistry for an extended set of a systematically doped model system. As model material, ceria (CeO_2) was used in this study since ceria based materials are well suited for fundamental investigations. Undoped and doped ceria adopt a simple face-centered cubic crystal structure (fluorite type) with 8–fold coordinated Ce^{4+} and 4-fold coordinated O^{2-}. A benefit of this simple structure is that it has only one cation site facilitating controlled doping and avoiding

complications from varying cation site occupation as *e.g.* in perovskites. Owing to the intrinsic redox–activity of Ce (Ce^{3+}/Ce^{4+}) oxygen transport and catalytic activity is present already for the undoped material. On account of the large solubility of acceptor, donor and redox-active dopants with comparable ion sizes, a controlled tuning of bulk point defect concentrations over a large range is possible. For example, doping of ceria with Gd^{3+} leads to oxygen vacancy formation, $Pr^{3+/4+}$ creates oxygen vacancies and redox activity, and Nb^{5+} causes the formation of conduction electrons and/or oxygen interstitials. While quantitative studies of surface defect concentrations are scare, the available data indicated that the relative changes *e.g.* upon doping or variation of oxygen partial pressure are similar as in bulk. In view of its use as catalyst material in automotive industry in the late 1970's, CeO_2 has been intensively investigated. Owing to its intrinsic redox–activity and high abundance of cerium in the earth crust, ceria based materials find an extremely wide range of applications beyond exhaust gas emission control and soot oxidation in automotive industry, *e.g.*, solid electrolyte in solid oxide fuel cells (SOFC), oxygen permeating membranes, catalyst for steam reforming, water gas shift and oxidation reactions, whereby the defect chemistry was only extensively addresses in the SOFC or oxygen permeating membrane community (see, *e.g.,* the review articles in refs.[7-11]). However, in the last years the importance of point defects in catalysis seems to be more recognized. For instance, in a recent review article[12] it was demonstrated that oxygen vacancies in ceria are key factors of the oxidation of volatile organic compounds.

The incorporation of oxygen is one major research field in solid state ionics since a deep understanding of this mechanism results into well-directed design of materials applicable, *e.g.,* energy storage, permeation membranes or as catalysts. The exchange of oxygen on metal oxides proceeds via a complex network of reaction steps such as chemisorption, dissociation and incorporation. The actual reaction rates depend on the surface defect concentrations which are coupled to the bulk concentrations and thus also to the oxygen activity in the gas phase.[13]

Consequently, the focus of this work is first to elucidate the impact of ionic and electronic point defects on the oxygen exchange kinetics for an extended set of systematically doped ceria. This is subsequently complemented by catalytic test reactions such as carbon monoxide and methane oxidation to provide a complete picture of point defect impacts on gas-solid reaction kinetics.

2 THEORY

In this chapter, the theoretical considerations required for the understanding and interpretation of the results presented in chapter 4 are given. First, the defect chemistry of doped ceria samples is introduced followed by an extensive discussion of the corresponding surface defect chemistry. Some experimental results are already presented here to give a full overview of the defect chemistry and sample behavior. The last section of this chapter deals with the calculation of the reaction rates for oxygen exchange kinetics, carbon monoxide oxidation and methane oxidation.

2.1 Bulk Defect Chemistry

In the following subchapters, bulk and surface defect chemistry of pure and doped ceria are introduced. The defect chemistry of the bulk material is well understood (Gd–, Pr–, and Nb–doping) and many data sets are available[14-23].

On the other hand, only a few studies are available in which the surface of doped and pure ceria has been investigated with respect to point defect concentrations and their oxygen partial pressure ($p(O_2)$) dependence since it is very challenging to measure under well–defined temperature and $p(O_2)$[24-27].

But if one considers a heterogeneous reaction of either a liquid or a gas phase compound with a solid, the point defects present in the surface layer of the solid are the most reactive and relevant ones (see, *e.g.* [1, 6]) and the oxygen partial pressure dependence has to be considered.

2.1.1 Pure Ceria

One fundamental aspect of $CeO_{2-\delta}$ is the property of changing its oxygen stoichiometry $(2-\delta)$ upon changes in $p(O_2)$ and temperature. The oxygen non-stoichiometry ($\delta \neq 0$) originates from the intrinsic redox activity of Ce and hence, is connected with the valence change between Ce^{3+} and Ce^{4+}. The release of one oxygen atom from the lattice to the gas phase is connected to the reduction of two Ce^{4+} and the formation of one oxygen vacancy in the crystal. Typical values for δ at 800 °C range between 10^{-5} (1 bar O_2) and 0.1 (10^{-20} bar O_2)[28].

In the following, the notation introduced by Kröger–Vink[29] is used which labels the ionic and electronic defects relative to the perfect crystal lattice, where subscripts denote the position and the superscripts the charge. Oxygen vacancies are denoted with $V_O^{\bullet\bullet}$ which means that one vacancy (V) is located on a former oxygen lattice site (0) with a two-fold positive charge relative to the perfect crystal

(••). In this manner, Ce^{4+} and Ce^{3+} are labeled as Ce_{Ce}^{x} and $Ce_{Ce}^{\prime}$, where in this case the superscripts x and ′ stand for neutral and one–fold negative charge, respectively.

In general, the overall incorporation of gas phase oxygen into the bulk material of ceria is expressed via reaction r. 1 where $e^{\prime}$ denotes electrons and O_O^x regular lattice oxygen.

$$1/2O_2 + 2e^{\prime} + V_O^{\bullet\bullet} \rightleftharpoons O_O^x \qquad \text{r. 1}$$

In r. 1, the creation of $e^{\prime}$ corresponds to the reduction of Ce^{4+} (Ce_{Ce}^{x}) to Ce^{3+} ($Ce_{Ce}^{\prime}$) by forming small polarons[30]. Since the reduction enthalpy of ceria (*cf.* r. 1) is positive with a value of approx. 7 eV[31], the intrinsic redox activity is accessible only either at high temperatures and/or very low $p(O_2)$. In this regime, ceria is not only an oxygen ion conductor, but also an electronic conductor; a so–called mixed ionic–electronic conductor (MIEC).

In equilibrium, the concentration of each species is determined by a mass action constant K according to eq. 1 where square brackets denote concentrations (in this section, concentrations/partial pressures are always refer to equilibrium concentrations/partial pressures) and ideally diluted conditions are assumed. It is also possible to formulate the mass action law in terms of electron holes ($h^{\bullet}$), whereby K and $K^{\prime}$ differ by the band gap mass action constant.

$$K(T) = \frac{[O_O^x]}{\sqrt{p(O_2)}[V_O^{\bullet\bullet}][e^{\prime}]^2} \qquad \text{or:} \quad K^{\prime}(T) = \frac{[O_O^x][h^{\bullet}]^2}{\sqrt{p(O_2)}[V_O^{\bullet\bullet}]} \qquad \text{eq. 1}$$

In undoped bulk ceria, the electroneutrality condition $2[V_O^{\bullet\bullet}] = [e^{\prime}]$ ($[Ce_{Ce}^{\prime}]$) holds. Inserting this into eq. 1 and solving for $[V_O^{\bullet\bullet}]$ and $[e^{\prime}]$ yields a $p(O_2)$ dependence of $2[V_O^{\bullet\bullet}] = [e^{\prime}] \propto p(O_2)^{-1/6}$. The knowledge about the $p(O_2)$ dependence of the defect species will be important later in this work since this has to be considered when the $p(O_2)$ dependence of the measured reaction rates are interpreted, *cf.* section 2.3.2.

The concentration of the point defects can deliberately be controlled by doping of ceria (at higher doping concentrations the terminus *substitution* instead of *doping* would be more accurate). In this work, three kinds of dopants are used: (i) Pr for enhancing the redox properties, (ii) Gd as an acceptor dopant and (iii) Nb as a donor dopant. The influence of the defect chemistry of those dopants is discussed in the following sections.

2.1.2 Redox–Doped Ceria

Doping of ceria with a redox–active element with a smaller reduction enthalpy and comparable cation size leads to an enhanced redox–activity compared to pure

ceria while maintaining the fluorite type crystal structure. Such elements are, *e.g.,* praseodymium and terbium. From here on, this kind of doping is denoted as *redox–doping*. Since Pr– and Tb–doped ceria show comparable defect chemical behavior (*cf.* [32]), the following description will focus only on Pr, but it is applicable to Tb as well. In case of redox–doping, the intrinsic oxygen incorporation reaction of ceria in r. 1 is complemented by the redox reaction of Pr. The overall oxygen excorporation (r. 2 and eq. 2) then shows a smaller reduction enthalpy of 1.5 eV[14, 15] compared to pure ceria:

$$O_O^x + 2Pr_{Ce}^x \rightarrow 1/2O_2 + V_O^{\bullet\bullet} + 2Pr_{Ce}' \qquad \text{r. 2}$$

$$K(T)_{Pr} = \frac{\sqrt{p(O_2)}[V_O^{\bullet\bullet}][Pr_{Ce}']^2}{[O_O^x][Pr_{Ce}^x]^2} \qquad \text{eq. 2}$$

With increasing Pr content, the overlap of Pr and O states leads to the formation of a so–called impurity band, which becomes broader as more Pr is introduced. The broadening of the impurity band can be seen in the absorption band of Pr (UV-Vis spectra in figure 1a) at lower energies (≈1.8 eV).

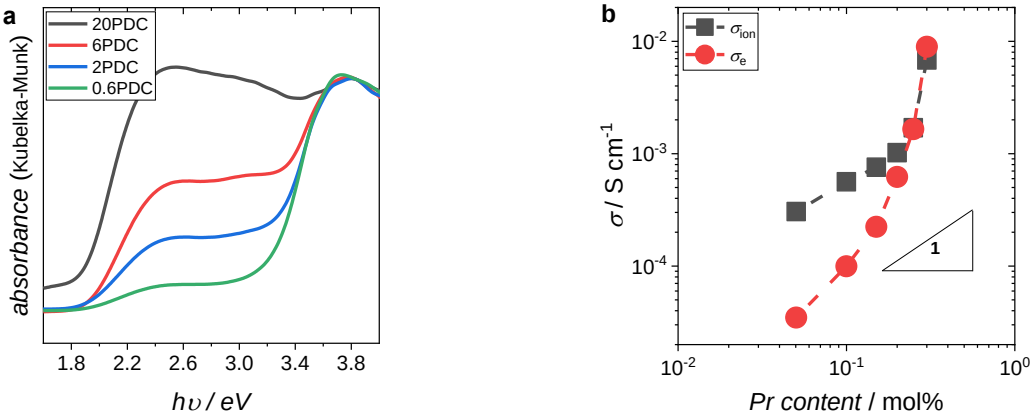

Figure 1: a) Obtained UV–Vis spectra of Pr doped ceria. b) Ionic and electronic conductivity of a series of Pr doped ceria. The electronic conduction increases strongly with increasing Pr concentration. Data was taken from ref.[33].

With increasing Pr concentration, the absorption increases due to $O - Pr^{4+}$ charge transfer processes. This mode becomes more pronounced with increasing dopant concentration indicating the formation of an impurity band. Electronic conductivity in PDC occurs by small polaron hopping and shows a maximum in electronic conductivity at equimolar concentrations of Pr^{4+}/Pr^{3+}[14, 15]. The impurity band also facilitates the electronic conductivity, which increases over–proportionally with increasing concentration of Pr (see electronic conductivity in figure 1b from ref.[33]). It is important to note that the change in the electronic structure leads to deviations from ideally dilute defect chemistry, *e.g.* the reduction enthalpy

becoming dependent on Pr concentration as observed in ref.[14] (H_r^o between 5.2 – 4.0 eV for 20 – 0.2 mol% Pr in doped ceria)

The release of oxygen is connected to the formation of one $V_O^{\bullet\bullet}$ and to the reduction of two Pr^{4+} to Pr^{3+}. Therefore, Pr doping involves electronic and ionic defects (see the Brouwer diagram in figure 2, calculated according to ref.[15]) and shows MIEC behavior like pure ceria, but already at milder conditions.

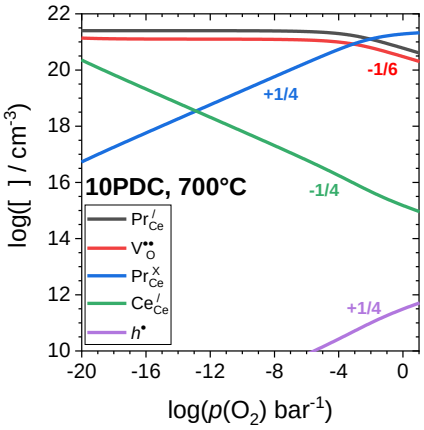

Figure 2: Point defect concentrations calculated for 10PDC at 700 °C according to literature data in ref.[15].

At low $p(O_2)$, all Pr is tetravalent and $[V_O^{\bullet\bullet}]$ is constant according to the condition $[Pr'_{Ce}] \approx 2[V_O^{\bullet\bullet}]$. Considering eq. 2, $[Pr_{Ce}^x]$ scales with $p(O_2)^{1/4}$ and $[Ce'_{Ce}] = [e'] \propto p(O_2)^{-1/4}$ is obtained by considering eq. 1. With increasing $p(O_2)$, more Pr becomes oxidized. In this regime, $[Pr'_{Ce}] \approx 2[V_O^{\bullet\bullet}]$ still holds, but varies with changes of $p(O_2)$. Inserting the condition $[Pr'_{Ce}] \approx 2[V_O^{\bullet\bullet}]$ in eq. 2 yields $[Pr'_{Ce}] \approx 2[V_O^{\bullet\bullet}] \propto p(O_2)^{-1/6}$.

In figure 3, the bulk fraction of Pr^{3+} relative to the total Pr concentration $[Pr]_{tot}$ from TG measurements is plotted at different $p(O_2)$ and temperatures for 20, 6, and 2PDC. For quantification of $Pr^{3+/4+}$ it was assumed that the activity of the intrinsic valance change of $Ce^{3+/4+}$ in the considered temperature and oxygen partial pressure regime is negligible small, and that at high $p(O_2)$ and low T only Pr^{4+} is present.

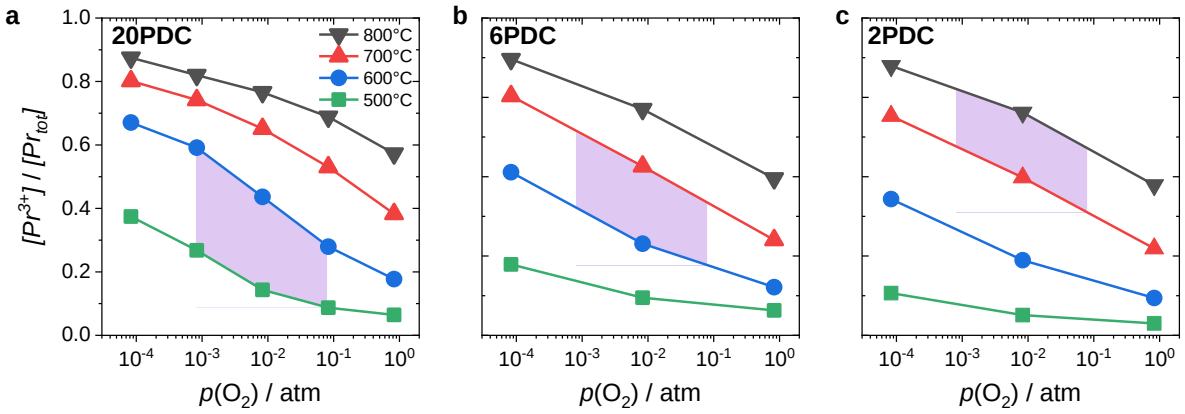

Figure 3: Pr^{3+} fraction relative to the total Pr content as a function of oxygen partial pressure at 500 – 800 °C for a), 20PDC, b) 6PDC, and c) 2PDC.

The magenta area indicates the measurement conditions where later the oxygen exchange kinetics is investigated. In this regime, about 15 – 80 % of Pr is in its 3+ state with a corresponding $V_O^{\bullet\bullet}$ concentration. At high temperature and/or lower oxygen partial pressure, the dependence of the $[Pr'_{Ce}]/[Pr]_{tot}$ ratio flattens and $[Pr'_{Ce}] \rightarrow [Pr]_{tot}$. The ratio varies moderately with $p(O_2)$ and T but the dependence on $[Pr]_{tot}$ is small. Overall, the relation $[V_O^{\bullet\bullet}] \propto [Pr]_{tot}$ is a reasonable approximation to describe the dependence of $[V_O^{\bullet\bullet}]$ with the total Pr content which varies by 1.5 orders of magnitude.

The MIEC behavior of 10 mol% Pr doped ceria is displayed in figure 4 according to ref.[15] by plotting the conductivity of the different defect species as a function of $p(O_2)$. The total conductivity σ_{tot} is purely ionic in an intermediate $p(O_2)$ regime. At higher partial pressures, the total conductivity comprises comparable shares of ionic ($\sigma_{V_O^{\bullet\bullet}}$) and electronic conductivity, whereby the electronic conductivity consists of $Pr^{4+/3+}$ small polaron hopping ($\sigma_{e,trapped}$) and contributions of electrons in the ceria conduction band (σ_e).

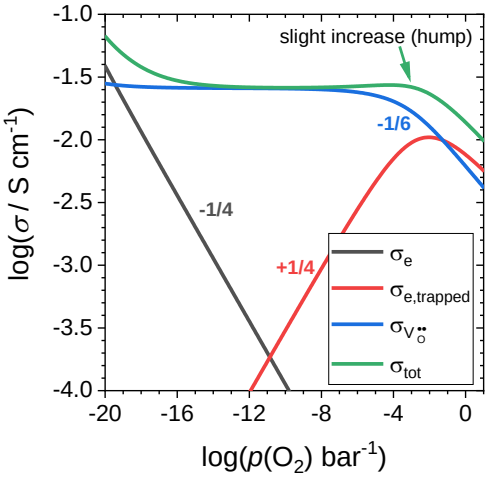

Figure 4: Point defect conductivities calculated for 10PDC at 700 °C according to literature data in ref.[15].

An interesting feature of Pr doped ceria is the appearance of a small *hump* in the total conductivity at higher oxygen partial pressures (see figure 4), which is related to the partial reduction of Pr. When 50 % of the total Pr amount is reduced, the conductivity contribution due to small polaron hopping reaches its maximum. As the $p(O_2)$ increases more, the oxidation of Pr is favored and hence the conductivity decreases.

2.1.3 Acceptor–Doped Ceria

Acceptor doping of ceria by cations with a fixed valance like Gd^{3+} yields an increased, but fixed amount of additional $V_O^{\bullet\bullet}$ according to r. 3:

$$Gd_2O_3 + 2Ce_{Ce}^{x} + O_O^{x} \rightarrow 2Gd'_{Ce} + V_O^{\bullet\bullet} + 2CeO_2 \qquad \text{r. 3}$$

For oxidizing conditions, the amount of $V_O^{\bullet\bullet}$ is pinned according to the condition $[Gd'_{Ce}] = 2[V_O^{\bullet\bullet}]$ and the $p(O_2)$ dependence of $[V_O^{\bullet\bullet}]$ is zero. Inserting the condition into eq. 1, the $p(O_2)$ dependence for electron holes ($h^{\bullet}$) and excess electrons (Ce'_{Ce}) is found to be $\pm 1/4$. It is important to note that this doping situation does not lead to a higher conduction electron concentration in contrast to a situation where $V_O^{\bullet\bullet}$ are created by reduction of ceria. Due to the increased $[V_O^{\bullet\bullet}]$, Gd–doped ceria shows higher ionic conductivities. But under strongly reducing or oxidizing conditions contributions of n–, or p–type electronic conduction are present in the total conductivity (*cf.* [34-36]).

2.1.4 Donor–Doped Ceria

Donor doping by five-fold positively charged cations like Nb^{5+} leads to an annihilation of $V_O^{\bullet\bullet}$ due to the formation of oxygen interstitials (O_i'') under oxidizing conditions according to r. 4:

$$Nb_2O_5 + 2Ce_{Ce}^{x} \rightarrow 2Nb_{Ce}^{\bullet} + O_i'' + 2CeO_2 \qquad \text{r. 4}$$

The amount of O_i'' is fixed by the neutrality condition $[Nb_{Ce}^{\bullet}] = 2[O_i'']$. However, under reducing conditions the compensation is predominantly electronic according to $[Nb_{Ce}^{\bullet}] = [e'] = [Ce'_{Ce}]$ and is described by r. 5:

$$Nb_2O_5 + 4Ce_{Ce}^{x} \rightarrow 2Nb_{Ce}^{\bullet} + 2Ce'_{Ce} + 2CeO_2 \qquad \text{r. 5}$$

In the experimental conditions in this work the formation of O_i'' dominates[22, 23]. The system with equal acceptor and donor concentrations ($[Nb_{Ce}^{\bullet}] = [Gd'_{Ce}]$ or $[Nb_{Ce}^{\bullet}] = [Pr'_{Ce}]$) can be used to have Gd'_{Ce} or Pr'_{Ce} present but with minimized $[V_O^{\bullet\bullet}]$.

2.2 Surface Defect Chemistry

2.2.1 Theoretical Considerations

Due to structural distortion and symmetry breaking, the concentrations of ionic and electronic defects j in the surface layer of a solid ($c_{j,\mathrm{s}}$) differ from the bulk values ($c_{j,\mathrm{b}}$). Such redistributions lead to a local excess charge, in contrast to the bulk where electroneutrality is always fulfilled. Therefore, the formation of a space charge potential $\Delta\varphi$ within a space charge layer (SCL) occurs, which is the difference between the electrostatic potential at the interface (φ_s) and the bulk (φ_b).

In equilibrium, the electrochemical potentials of a surface defect ($\tilde{\mu}_\mathrm{s}$) and the respective bulk species ($\tilde{\mu}_\mathrm{b}$) are equal. Deconvolution into the chemical potential μ and the electrostatic potential φ (z_j is the charge of the defect species, μ_j° is the standard electrochemical potential, k_B denotes Boltzmann's constant, and e is the elementary charge) yields:

$$\begin{aligned} \mu_j^\circ + k_B T\ln\left(c_{j,\mathrm{s}}\right) + z_j eF\varphi_\mathrm{s} &= \mu_j^\circ + k_B T\ln\left(c_{j,\mathrm{b}}\right) + z_j eF\varphi_\mathrm{b} \\ \ln\left(\frac{c_{j,\mathrm{s}}}{c_{j,\mathrm{b}}}\right) &= -\frac{z_j e}{k_B T}\Delta\varphi \end{aligned} \qquad \text{eq. 3}$$

The corresponding concentration profiles can be obtained by applying Poisson's equation, which turns into the Poisson–Boltzmann differential equation when combined with eq. 3 (ε_0 and ϵ_r are the vacuum and relative permittivity and ρ is the charge density):

$$\nabla^2\varphi = -\frac{\rho}{\varepsilon_0\epsilon_\mathrm{r}} = \frac{z_j e c_{j,s}}{\varepsilon_0\epsilon_\mathrm{r}} = \frac{z_j e}{\varepsilon_0\epsilon_\mathrm{r}} c_{j,\mathrm{b}}\exp\left(-\frac{z_j e}{k_B T}\Delta\varphi\right) \qquad \text{eq. 4}$$

In case of acceptor doped ceria, an appropriate boundary condition to solve eq. 4 is the so–called Mott–Schottky approximation where it is assumed that the acceptor dopant is immobile and its profile horizontal. The concentration profile near a grain boundary of acceptor doped ceria is shown in figure 5, assuming the Mott-Schottky case[37].

In case of ceria $\Delta\varphi$ is positive, which was experimentally found at grain boundaries, *e.g.* in ref.[38]. Also from present impedance measurements performed on Gd-doped ceria (figure 5b) the space charge potential is positive. The thickness of the SCL increases with decreasing [Gd] to maintain a constant SCL charge. In this case, the depletion of [$V_O^{\bullet\bullet}$] to the interface is stronger compared to higher dopant concentration. This depletion is exponentially connected to $\Delta\varphi$ (Poisson–Boltzmann), which results into an increased $\Delta\varphi$ in case of small [Gd] (see, *e.g.*, refs.[39, 40]).

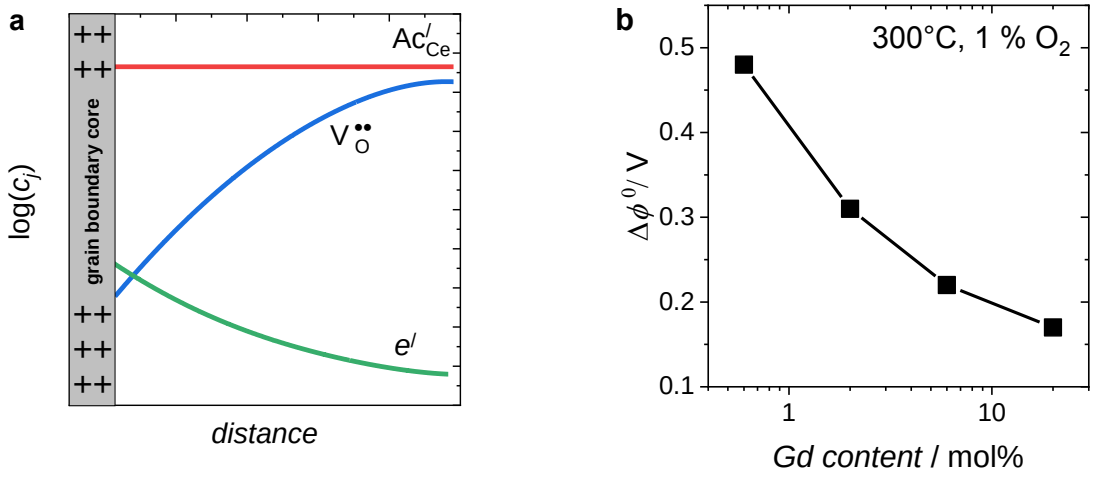

Figure 5: a) Mott–Schottky case in acceptor doped ceria: Concentration profile of acceptor dopants, oxygen vacancies and electrons near a positively charged grain boundary core with a space charge potential of +0.44 V. The concentration of the acceptor dopant is constant (immobile). Due to the positive potential, a depletion of oxygen vacancies is observed connected to an enrichment of electrons. Data was taken from ref.[37]. b) Space charge potential of Gd–doped ceria versus bulk Gd concentration obtained by electrochemical impedance spectroscopy of dense pellets *cf.* chapter 3.3.

The charge density ρ can be integrated to obtain the total charge Σ_{SCL} within the SCL (x denotes the distance to the interface):

$$\Sigma_{\mathrm{SCL}} = \int_0^{\infty} \rho \, \mathrm{d}x \qquad \text{eq. 5}$$

A change in the electrostatic potential is compensated by a change in the concentration profiles to maintain electrochemical equilibrium, hence eq. 3 can be rewritten:

$$\partial \ln\left(\frac{c_{j,\mathrm{s}}}{c_{j,\mathrm{b}}}\right) = -\frac{z_j e}{k_B T}\partial(\Delta\varphi) \qquad \text{eq. 6}$$

The oxygen partial pressure dependence of the concentrations of the surface and bulk defect species is given in eq. 7 where n_j is the oxygen partial pressure exponent with respect to the defect species j:

$$\frac{\partial \ln(c_j)}{\partial \ln(p(\mathrm{O}_2))} = n_j \qquad \text{eq. 7}$$

A relationship connecting n_j and $\Delta\varphi$ is obtained by substitution of eq. 7 into eq. 6:

$$n_{j,\mathrm{s}} - n_{j,\mathrm{b}} = -\frac{z_j e}{k_B T}\frac{\partial(\Delta\varphi)}{\partial \ln(p(\mathrm{O}_2))} \qquad \text{eq. 8}$$

From eq. 8, two important statements can be made:

(i) If the variation of $\Delta\varphi$ and hence Σ_{SCL} with changing $p(O_2)$ is minute, the $p(O_2)$ dependence n_j of the defect species located in the bulk and surface layer do not change and vice versa.

(ii) The fact that the absolute defect concentration at the surface differs from the bulk value does not influence the oxygen partial pressure dependence, as long as the defect chemistry does not change qualitatively, and the majority defects do not change with respect to the bulk and surface.

2.2.2 Surface Defect Chemistry of Undoped and Doped Ceria

Table 1: Surface *vs.* bulk defect chemistry. Different defect regimes with respect to the oxygen partial pressure dependence of the surface are compared to the bulk regime (intrinsic, acceptor–, and donor–doped ceria).

	Surface Regime	Bulk Regimes				Surface Regime
		Intrinsic	Acceptor	Donor		
		$2[V_O^{\bullet\bullet}]_b = [e']_b$ $n_{V,b} = n_{e,b} = 1/6$	$2[V_O^{\bullet\bullet}]_b = [Gd']_b$ $\Rightarrow [V_O^{\bullet\bullet}]_b = const.$ $n_{e,b} = -1/4$	$[Nb^{\bullet}]_b = [e']_b$ $\Rightarrow [e']_b = const.$ $n_{Oi,b} = 1/2$	$2[O_i'']_b = [Nb^{\bullet}]_b$ $\Rightarrow [O_i'']_b = const.$ $n_{e,b} = -1/4$	
(1)	$\Sigma_{SCL} = 0$ $2[V_O^{\bullet\bullet}]_s = [e']_s$ $n_{V,s} = n_{e,s} = -1/6$	equal n	different n	equal n	different n	$\Sigma_{SCL} = 0$ $[Nb^{\bullet}]_s = [e']_s$ $n_{Oi,s} = 1/2$
(2)	$\Sigma_{SCL} = 0$ $2[V_O^{\bullet\bullet}]_s = [Gd']_s$ $n_{e,s} = -1/4$	different n	equal n	different n	equal n	$\Sigma_{SCL} = 0$ $[O_i'']_s = [Nb^{\bullet}]_s$ $n_{e,s} = -1/4$
(3)	$\Sigma_{SCL} \neq 0$ $\Sigma_{SCL} \approx 2[V_O^{\bullet\bullet}]_s = const.$ $n_{e,s} = -1/4$	different n	equal n	different n	equal n	$\Sigma_{SCL} \neq 0$ $\Sigma_{SCL} \approx 2\left[O_i''\right]_s = const.$ $n_{e,s} = -1/4$
(4)	$\Sigma_{SCL} \neq 0$ $\Sigma_{SCL} \approx [e']_s = const.$ $n_{V,s} = -1/2$	different n	different n	equal n	different n	$\Sigma_{SCL} \neq 0$ $\Sigma_{SCL} \approx [e']_s = const.$ $n_{Oi,s} = -1/2$
(5)	$\Sigma_{SCL} \neq 0$ but small $K = K_\infty \exp(-\frac{zF\varphi}{RT})$ $n_{e,s} = -x$ $n_{V,s} = -2n_{e,s} - 1/2$	different n	different n	different n	different n	$\Sigma_{SCL} \neq 0$ but small $K = K_\infty \exp(-\frac{zF\varphi}{RT})$ $n_{e,s} = -x$ $n_{V,s} = -2n_{e,s} - 1/2$

probable cases
less probable cases
hard to estimate

intrinsic and acceptor doped: $O_2 + 2V_O^{\bullet\bullet} \rightleftharpoons 2O_O^x + 4h^{\bullet}$

donor doped: $O_2 + 2V_i^x \rightleftharpoons 2O_i'' + 4h^{\bullet}$

$\log(K) = 4\log([h^{\bullet}]) - 2\log([V_O^{\bullet\bullet}]) - \log(p(O_2))$

$\Rightarrow 1 = 4n_h - 2n_v$

The data given in table 1 summarize all possible situations regarding the oxygen partial pressure dependence of the defect species at the surface in case of pure, acceptor–, and donor–doped ceria. The gray/white colored boxes give a qualitative direction whether the considered defect chemical regime is most likely to be present or not. Dark gray boxes indicate probable cases, bright gray denotes less probable ones and white denotes defect regimes, which are hard to estimate due to the lack of appropriate literature. Please note that the deduction of the probability of the presence a specific defect chemical regime at the surface refers just to ceria. The

absolute concentrations of defects at the surface differ from those in the bulk (figure 5a), but depending on the regime the oxygen partial pressure dependence may change or not.

First, an overview of the possible defect chemical regimes is given followed by a specific discussion of intrinsic and doped ceria. In the first two cases in table 1, a zero surface charge (Σ_{SCL}) arises if:

(1) The surface oxygen vacancies ($V_{O,s}^{\bullet\bullet}$) are compensated by surface electrons (e_s') which results in an oxygen partial pressure dependence of $2[V_{O,s}^{\bullet\bullet}] = [e_s'] \propto p(O_2)^{-1/6}$. This is expected to occur only under strongly reducing conditions.

(2) The $[V_{O,s}^{\bullet\bullet}]$ is determined by the surface acceptor dopant $[A_{Ce,s}']$. Therefore, $[V_{O,s}^{\bullet\bullet}]$ is $p(O_2)$ independent and for surface electrons the relationship $[e_s'] \propto p(O_2)^{-1/4}$ is valid.

Three further cases can be distinguished in which Σ_{SCL} shows a non–zero value:

(3) The concentrations of $V_{O,s}^{\bullet\bullet}$ are large at the surface meaning that Σ_{SCL} is also large and is determined by $[V_{O,s}^{\bullet\bullet}]$. The relative change of $[V_{O,s}^{\bullet\bullet}]$ is small due to its high concentration, hence a reasonable approximation is that the $V_{O,s}^{\bullet\bullet}$ do not show perceptible $p(O_2)$ dependence, and hence $[e_s'] \propto p(O_2)^{-1/4}$.

(4) A constant Σ_{SCL} results due to a high $[e_s']$, and hence $[V_{O,s}^{\bullet\bullet}] \propto p(O_2)^{-1/2}$.

(5) The last case corresponds to a small Σ_{SCL} which implies that Σ_{SCL} may have a perceptible $p(O_2)$ dependence which makes it hard to derive an analytical expression for the $p(O_2)$ dependence of the surface defects.

For ceria–based materials, data regarding the surface defect chemistry is only rarely available since it is very challenging to measure the surface defect concentrations under well–defined temperature and oxygen partial pressure conditions directly. Generally, in case of a non–zero Σ_{SCL}, it is expected that the sign is positive for ceria. Indeed, a positive Σ_{SCL} for grain boundary cores in ceria has been found experimentally (*cf.* ref[38], and own data in figure 5b). A positive excess charge (about +2 elementary charges per surface of a unit cell with 128 ceria formula units) was found in ref.[41] by Kinetic Monte Carlo simulations on 10 mol% Gd doped ceria. For zirconia electrolyte materials and for a YSZ bicrystal an accumulation $V_O^{\bullet\bullet}$ in the grain boundary core could be seen by TEM[42].

Concentrations of surface defects have been measured by ambient–pressure XPS on ceria thin films, which is experimentally rather challenging. It was concluded that the surface charges are rather small[24-26, 43]. The concentrations of surface Ce_{Ce}' and $V_{O,s}^{\bullet\bullet}$ are strongly increased compared to the bulk, from which a decreased

reduction enthalpy by 1 eV was deduced. This agrees well with DFT calculations[44] (decrease of the reduction enthalpy by 0.8 eV for (111) surfaces to 1.4 eV for (110) surfaces) and experiments on monocrystalline ceria samples[31]. But at a $p(O_2)$ of 10^{-4} bar and 450 °C, which is comparable to the condition in this work, the amount of surface Ce'_{Ce} is still smaller than the acceptor dopant concentration. In ref.[45] it was discussed that the data in ref.[43] could be interpreted by a surface space charge potential that is independent of an applied d.c. bias (independent of the oxygen chemical potential in the thin film). Therefore, it can be concluded that case **(4)** does not apply for ceria.

Ambient–pressure XPS studies on undoped ceria thin films under reducing conditions found that the excess concentrations of $V_{O,s}^{\bullet\bullet}$ and e'_s (Ce'_{Ce}) match almost perfectly[24] so that Σ_{SCL} appears to be rather small. Hence, case **(1)** can be assumed to be valid for undoped ceria under reducing conditions. Also on Sm–doped ceria (reducing conditions) it was found that $V_{O,s}^{\bullet\bullet}$ and Ce'_{Ce} largely mutually charge compensate[25] which means that case **(2)** applies here. On Pr–doped ceria thin films on YSZ and modified effective $p(O_2)$ (tuned by a d.c. bias) it was found by ambient–pressure XPS that the surface concentration of Pr'_{Ce} increases less with decreasing $p(O_2)$ compared to bulk Pr'_{Ce}, and it was also argued that Pr–doped ceria does not have a pronounced surface charge[27]. Even if there is a surface charge, since highly acceptor doped samples are considered in this work, and hence a high and constant $V_{O,s}^{\bullet\bullet}$ concentration is expected which fixes the Σ_{SCL} with respect to $p(O_2)$ changes (case **(3)**), the oxygen partial pressure dependence of the defects are equal to the bulk. Approximately $p(O_2)$ independent space charge potentials and corresponding approximately constant excess charges have been observed for grain boundaries in ref.[46] for Fe-doped $SrTiO_3$.

Overall, for undoped as well as acceptor–doped ceria one can reasonably assume similar $p(O_2)$ dependencies of surface and bulk defects. Regarding Pr–doped ceria, a smaller $p(O_2)$ dependence of surface Pr'_{Ce} in the range of -0.1 instead of -1/6 for the surface might be present. For donor–doped ceria (Nb–doped ceria), no direct measurements of surface defect concentrations are available so far. Nevertheless, a number of probable cases yield the same defect chemical regimes for surface and bulk.

2.2.3 Surface Orientations

The thermodynamically most stable surface orientation of ceria is (111), followed by (110), and (100)[47]. For doped ceria samples, no surface energies could be retrieved from the literature. But at least for a low dopant level the same sequence

of surface stabilities is probable. In this work, it is assumed that the surface, at least in the pulsed isotope exchange experiment, is largely reconstructed into the most stable termination due to the harsh annealing at 1400°C prior to measurement for undoped as well as doped ceria samples.

The formation energy of $V_O^{\bullet\bullet}$ at the surface depends on the surface orientation and leads to a significant variation of the oxygen vacancy concentration of undoped ceria under reducing conditions [44, 47]. Such differences are assumed to be much less pronounced for acceptor doped ceria where the oxygen vacancy concentration is largely fixed by the dopant. In ref.[44], it was found that the formation enthalpy for oxygen vacancies in the surface layer increases according to (110) < (100) < (111).

Regarding the reaction rate of oxygen incorporation, no dependence on the surface terminations is available so far for ceria. However, for epitaxial $La_{0.7}Sr_{0.3}MnO_{3-\delta}$ perovskite films, the variation of the surface reaction rate constant of oxygen incorporation between the surface terminations (001), (110), and (111) has been found to be less than a factor of four.[48, 49]

2.3 Calculation of Reaction Rates

2.3.1 Carbon Monoxide and Methane Oxidation

The apparent reaction rate for carbon monoxide oxidation R_{CO}, and methane oxidation $R_{\mathrm{CH_4}}$ was calculated according to eq. 9, which is commonly used to describe reaction kinetics measured in packed bed reactors (see, *e.g.*, ref.[50]). The conversion X_i of the reactant i, which describes how much of the reactant has reacted when exiting the reactor (relative difference of the inlet concentration $c_{i,\mathrm{in}}$ and exiting concentration $c_{i,\mathrm{ex}}$) is multiplied by the volume flow rate of the gas through the reactor, and normalized to the total surface area S of the catalyst particles.

$$R_i = \frac{\nu\left(c_{i,\mathrm{in}} - c_{i,\mathrm{ex}}\right)}{S} = \frac{\nu c_{i,\mathrm{in}}}{S} X_i \qquad \text{eq. 9}$$

Since the reactor is small (2 mm inner diameter, bed height ≈ 5 mm), no significant temperature gradients are expected. To calculate the apparent activation energy E_{a} of the oxidation process, it is reasonable to assume a first order reaction with respect to species i and the corresponding surface reaction rate k.

$$X_i = 1 - \exp\left(-\frac{k_i S}{\nu}\right) \Leftrightarrow \ln(1 - X_i) = -\frac{k_i S}{\nu} \qquad \text{eq. 10}$$

Plugging in the Arrhenius type behavior for $k_i = \gamma \exp(-\frac{E_a}{RT})$ results in an expression from which an apparent activation energy E_a can be obtained (γ denotes the pre-exponential factor):

$$\ln(-\ln(1 - X_i)) = -\frac{E_a}{R}\frac{1}{T} + \ln\left(\frac{\gamma S}{\nu}\right) \qquad \text{eq. 11}$$

2.3.2 Pulsed Oxygen Isotope Exchange (PIE)

The gas phase fraction of oxygen can be analyzed either by considering just the $^{18}O/^{16}O$ fractions or the fractions of the oxygen isotopologues $^{32}O_2$, $^{34}O_2$, and $^{36}O_2$, which correspond to $^{16}O^{16}O$, $^{16}O^{18}O$, and $^{18}O^{18}O$, respectively. In the following, the analysis in terms of the $^{18}O/^{16}O$ fractions is introduced followed by the approach of analyzing the oxygen isotopologues.

The gas phase fractions of $^{18}O/^{16}O$ at the exit of the reactor are analyzed based on the overall oxygen incorporation reaction with its forward and backward reaction constants $\vec{k}_O$ and $\overleftarrow{k}_O$, respectively as displayed in reaction r. 6.

$$O_2 + 2V_O^{\bullet\bullet} + 4e' \underset{\overleftarrow{k}_O}{\overset{\vec{k}_O}{\rightleftharpoons}} 2O_O^x \qquad \text{r. 6}$$

Since PIE is conducted under equilibrium conditions, the forward and backward reaction rates are equal yielding the equilibrium exchange rate of oxygen incorporation $\Re_0$[51, 52] (eq. 12). To accent the importance of the equilibrium condition in the following derivation, the equilibrium concentrations are labeled with [$\widehat{\ }$].

$$\Re_0 = \vec{k}_O[\widehat{O_2}][\widehat{V_O^{\bullet\bullet}}]^2[\widehat{e'}]^4 = \overleftarrow{k}_O[\widehat{O_O^x}]^2 \qquad \text{eq. 12}$$

Formulating now the rate law with respect to oxygen incorporation described in r. 6, substitution of eq. 12, and taking the surface area of the sample particles (S) into account, the change of the gas phase concentration of oxygen (eq. 13) can be obtained:

$$\frac{V}{S}\frac{d[O_2]}{dt} = -\Re_0\left(\frac{[O_2][V_O^{\bullet\bullet}]^2[e']^4}{[\widehat{O_2}][\widehat{V_O^{\bullet\bullet}}]^2[\widehat{e'}]^4} - \frac{[O_O^x]^2}{[\widehat{O_O^x}]^2}\right) \qquad \text{eq. 13}$$

Considering now the isotopic exchange in chemical equilibrium, eq. 13 describes the deviation from isotopic equilibrium of oxygen where the point defect concentrations do not change over time. Replacing concentrations with fractions (f_g for oxygen gas phase fraction and f_s for lattice oxygen fraction) eq. 13 turns to eq. 14 and eq. 15 for the oxygen isotopologues $^{32}O_2$ and $^{36}O_2$

$$\frac{V}{S}\frac{\mathrm{d}^{32}f_\mathrm{g}}{\mathrm{d}t}\left[\widehat{\mathrm{O}_2}\right] = -\Re_0\left({}^{32}f_\mathrm{g} - {}^{16}f_\mathrm{s}^2\right) \qquad \text{eq. 14}$$

$$\frac{V}{S}\frac{\mathrm{d}^{36}f_\mathrm{g}}{\mathrm{d}t}\left[\widehat{\mathrm{O}_2}\right] = -\Re_0\left({}^{36}f_\mathrm{g} - {}^{18}f_\mathrm{s}^2\right) \qquad \text{eq. 15}$$

The rate law of the mixed oxygen isotopologue $^{34}O_2$ is obtained by applying the law of mass conservation:

$$\frac{V}{S}\frac{\mathrm{d}^{34}f_\mathrm{g}}{\mathrm{d}t}\left[\widehat{\mathrm{O}_2}\right] = -\frac{V}{S}\left(\frac{\mathrm{d}^{32}f_\mathrm{g}}{\mathrm{d}t} + \frac{\mathrm{d}^{36}f_\mathrm{g}}{\mathrm{d}t}\right)\left[\widehat{\mathrm{O}_2}\right] = \Re_0\left({}^{34}f_\mathrm{g} - 2\,{}^{16}f_\mathrm{s}\,{}^{18}f_\mathrm{s}\right) \qquad \text{eq. 16}$$

The rate law of ^{18}O incorporation is then:

$$\frac{V}{S}\frac{\mathrm{d}^{18}f_\mathrm{g}}{\mathrm{d}t}2\left[\widehat{\mathrm{O}_2}\right] = -\frac{V}{S}\left(\frac{\mathrm{d}^{36}f_\mathrm{g}}{\mathrm{d}t} + \frac{1}{2}\frac{\mathrm{d}^{34}f_\mathrm{g}}{\mathrm{d}t}\right)2\left[\widehat{\mathrm{O}_2}\right] = -\Re_0\left({}^{18}f_\mathrm{g} - {}^{18}f_\mathrm{s}\right) \qquad \text{eq. 17}$$

By integration of eq. 17 from time range of zero to τ – where τ denotes the mean residence time of the pulse in the packed bed – and by assuming that $^{18}f_s$ is always below 1 % of the available ^{16}O lattice oxygen, an expression for the equilibrium exchange rate of oxygen incorporation $\Re_0$ is obtained. ($^{18}f_{\mathrm{g,inlet}}$ is the ^{18}O gas phase fractions in pulse and $^{18}f_{\mathrm{g,exit}}$ is the fraction in the exiting gas):

$$\Re_0 = 2\left[\widehat{\mathrm{O}_2}\right]\frac{V}{\tau S}\ln\left(\frac{{}^{18}f_{\mathrm{g,inlet}}}{{}^{18}f_{\mathrm{g,exit}}}\right) \qquad \text{eq. 18}$$

The equilibrium exchange rate $\Re_0$ is connected to the effective surface exchange reaction rate constant k^* by[53]:

$$\Re_0 = k^*\left[\widehat{\mathrm{O}_\mathrm{O}^\mathrm{x}}\right]^{-1} \qquad \text{eq. 19}$$

This analysis of $\Re_0$ does not require the assumption of a specific reaction mechanism since it represents the overall oxygen exchange reaction where all reaction steps are merged. From the variation of $\Re_0$ with $p(O_2)$ and dopant/defect concentrations several important conclusions can be drawn. For this, the approach of the rate determining step (*rds*) is introduced, which has a slower exchange rate than fast preceding or subsequent reaction steps. In other words, one of the reaction steps merged in $\Re_0$ is such slow that it determines the overall reaction rate.

If, *e.g.,* the dissociative reaction (eq. 21) is the *rds* of the oxygen incorporation reaction, it will determine the overall exchange rate $\Re_0$ (assuming a fast oxygen adsorption as a pre–equilibrium step, eq. 20). In the following the equilibrium label

$[\widehat{\ }]$ is not used anymore for better legibility, but concentrations still refer to equilibrium concentrations.

$$O_2 \underset{\overleftarrow{k}_{ad}}{\overset{\vec{k}_{ad}}{\rightleftharpoons}} O_{2\,ad}^- + h^\bullet \quad \text{with} \quad K_1 = \frac{[O_2^-][h^\bullet]}{p(O_2)} \qquad \text{eq. 20}$$

$$O_{2\,ad}^- \underset{\overleftarrow{k}_{da}}{\overset{\vec{k}_{da}}{\rightleftharpoons}} 2O_{ad}^- + h^\bullet \Rightarrow \Re_0 \approx \frac{\vec{k}_{da} K_1 p(O_2)^1}{[h^\bullet]} \Rightarrow \Re_0 \propto p(O_2)^{1-m} \qquad \text{eq. 21}$$

The exponent m in eq. 21 denotes the influence of point defects on the overall oxygen partial pressure exponent n. In this case, molecular oxygen is involved in the *rds* and hence, $\Re_0$ is proportional to $p(O_2)^n$ with $n \leq 1$. The exponent n can be lowered to $1-m$ through the influence of point defects. For example, if for Gd–doped ceria, holes $[h^\bullet] \propto p(O_2)^{+0.25}$ appear before the actual rate–determining elementary step, then $m = 0.25$ and therefore $n = 1 - 0.25 = 0.75$.

If instead the incorporation of a single oxygen ad-atom (eq. 22) is assumed to be the *rds*, a different $p(O_2)$ dependence is obtained.

$$O_{ad}^- + V_O^{\bullet\bullet} \underset{\overleftarrow{k}_i}{\overset{\vec{k}_i}{\rightleftharpoons}} O_O^X + h^\bullet \qquad \text{eq. 22}$$

For the equilibrated dissociative–adsorption reaction in eq. 20 and eq. 21, one can write:

$$[O_{ad}^-] = \frac{\sqrt{K_1 K_2 p(O_2)}}{[h^\bullet]} \qquad \text{eq. 23}$$

The overall exchange rate $\Re_0$ equals the rate of oxygen ad–atom incorporation. By considering eq. 23, one obtains that $\Re_0$ is proportional to $p(O_2)^{0.5-m}$:

$$\Re_0 \approx \vec{k}_i [O_{ad}^-][V_O^{\bullet\bullet}] \approx \frac{\vec{k}_i \sqrt{K_1 K_2}[V_O^{\bullet\bullet}]}{[h^\bullet]} \sqrt{p(O_2)} \Rightarrow \Re_0 \propto p(O_2)^{0.5-m} \qquad \text{eq. 24}$$

This concept of the *rds* is generally applicable and enables one to distinguish whether molecular or atomic oxygen is involved in the *rds*. It is important to note that ideal behavior is assumed here. Nevertheless, non–idealities might be present at high dopant concentrations. However, sufficient quantitative data describing non–idealities of doped ceria samples are lacking, and the effect on the $p(O_2)$ dependece of $\Re_0$ is expected to be rather modest.

The analysis in terms of $\Re_0$ and hence the analysis of only the ^{18}O gas fraction does not fully exploit the information content available from the actual measured $^{32}O_2$, $^{34}O_2$, and $^{36}O_2$ gas phase composition. For a more quantitative analysis one

has to consider specific reaction mechanisms. The mechanisms denoted as M1 and M2 which are suggested in[54-56] haven been chosen here. These mechanisms represent simplified cases (with several elementary steps condensed into two steps) which nevertheless capture the important differences for the oxygen exchange reaction (involvement of $V_O^{\bullet\bullet}$, incorporation of O already in dissociative adsorption or not):

M1		**M2**	
$O_2 + 2e' \overset{^1\Re_{da}}{\rightleftharpoons} 2O^-$	r. 7	$O_2 + V_O^{\bullet\bullet} + 3e' \overset{^2\Re_{da}}{\rightleftharpoons} O^- + O_O^x$	r. 8
$O^- + V_O^{\bullet\bullet} + e' \overset{^1\Re_{i}}{\rightleftharpoons} O_O^x$	r. 9	$O^- + V_O^{\bullet\bullet} + e' \overset{^2\Re_{i}}{\rightleftharpoons} O_O^x$	r. 10

In these mechanisms, the molecular chemisorption (including the transfer of one or two electrons) is combined with the subsequent dissociation. This can be justified by the fact that chemisorption represents a fast preceding step which is correspondingly in quasi–equilibrium (formation of adsorbed superoxide and peroxide species happens already at very low *T*, see, *e.g.*, ref.[57]).

The question whether $V_O^{\bullet\bullet}$ is involved only in incorporation or also in dissociation, and which of these steps is limiting, cannot be decided a priori. For mixed conducting perovskites there is some evidence that $V_O^{\bullet\bullet}$ may appear in the rate determining step, see *e.g.*[58-60], and also for Tb–doped CeO_2 this has been suggested[61]. The bulk oxygen diffusion that follows after O incorporation into the surface layer does not explicitly appear in models M1 and M2; it is only required to be sufficiently fast to guarantee that the ^{18}O fraction in the lattice in the first layer remains small.

M1 is strictly sequential with respect to oxygen incorporation. Oxygen from the gas phase undergoes adsorption and dissociation at the surface by exchange rate $^1\Re_{da}$ (r. 7) followed by incorporation with rate $^1\Re_i$ (r. 9). In contrast, in mechanism M2 one oxygen atom is incorporated already in the dissociation step r. 8 with rate $^2\Re_{da}$, the second oxygen atom in the subsequent pure incorporation step r. 10 with rate $^2\Re_i$ (= $^1\Re_i$).

With respect to oxygen isotope exchange of the sample this corresponds to the presence of two parallel paths, because even for infinitely small $^2\Re_i$, $^{18}f_g$ can decrease by formation of $^{34}O_2$ in the backward reaction of eq. r. 8 until all oxygen of the first layer is exchanged. However, in the present samples the amount of ^{18}O in the pulse exceeds the amount of oxygen in the surface layer of the particles by

about three orders of magnitude, *i.e.,* a significant change of $^{18}f_g$ occurs only if bulk oxygen diffusion is possible. In this respect, the present pulsed isotope exchange does not differ from experiments that create an ^{18}O concentration profile in the solid detected by SIMS (k^*, see chapter 3.5), execute the fuel cell cathode reaction (k^q), or change the oxygen stoichiometry of the sample (k^δ, see chapter 3.6).

Expressions for the exchange rates $\Re_{da}$ (oxygen molecules per unit time and surface area; in contrast to ref. [54-56] which uses atoms per time and area) and $\Re_i$ (oxygen atoms per time and area) are given in the appendix. These rates depend on $p(O_2)$, defect concentrations and T. For the two mechanisms M1, M2 different relations between $\Re_0$ and $\Re_{da}$, $\Re_i$ can be obtained:

M1
$$\frac{1}{\Re_0} = \frac{1}{2\ {}^1\Re_{da}} + \frac{1}{{}^1\Re_i} \qquad \text{eq. 25}$$

M2
$$\Re_0 = {}^2\Re_{da}\left(1 + \frac{{}^2\Re_i}{{}^2\Re_{da} + {}^2\Re_i}\right) \qquad \text{eq. 26}$$

The statements in eq. 25 and eq. 26 nicely show the strictly sequential nature of M1 and parallel character of M2 with respect to the O uptake into the sample.

For M1, if ${}^1\Re_{da} \gg {}^1\Re_i$ then $\Re_0 \approx {}^1\Re_i$. In this case the ^{18}O exchange with the sample is very slow and $^{34}O_2$ is mainly formed via scrambling (recombination of adsorbed ^{18}O and ^{16}O atoms at the surface to $^{34}O_2$, backward reaction of r. 7, without changing $^{18}f_g$). If ${}^1\Re_{da} \ll {}^1\Re_i$ the value of $\Re_0$ becomes $\approx 2\ {}^1\Re_{da}$, and $^{18}O/^{16}O$ surface scrambling hardly occurs since ^{18}O incorporates immediately.

For M2, for the case of slow dissociative adsorption (${}^2\Re_{da} \ll {}^2\Re_i$), $\Re_0 \approx 2\ {}^2\Re_{da}$ is obtained as for M1. The situation differs for ${}^2\Re_{da} \gg {}^2\Re_i$. Since oxygen is not only adsorbed but one O also incorporated in the first step, reaction r. 8 already suffices to change $^{18}f_g$, and $\Re_0 \approx {}^2\Re_{da}$ (but only as long as unlabeled ^{16}O is still available in the surface layer). $^{34}O_2$ will mainly be formed by backward reaction of r. 8, rather than by pure surface scrambling in back-reaction r. 7. Thus, for M2 $\Re_0$ ranges between ${}^2\Re_{da}$ and $2\ {}^2\Re_{da}$, but only as long as unlabelled ^{16}O is still available in the surface layer. If ${}^2\Re_i$ as well as bulk oxygen diffusion is slow, the isotope exchange stops after exchanging the first layer.

For M1 and M2, different oxygen partial pressure $p(O_2)$ dependencies can be found if either $\Re_{da}$ or $\Re_i$ is considered as *rds*. When the dissociative–adsorption in r. 7 and r. 8 is rate-determining, the *rds* contains molecular oxygen species and correspondingly the expression for $\Re_{da}$ contains a term $\propto p(O_2)^1$. However, also

defects such as $V_O^{\bullet\bullet}$ and electronic defects may be involved in the *rds* or preceding equilibria. They will contribute to the overall $p(O_2)$ dependence of $\Re_{da}$, and typically decrease it by consumption of electrons/Ce'_{Ce}, formation of $h^\bullet$ in preceding equilibria such as molecular chemisorption, and involvement of $V_O^{\bullet\bullet}$

When the incorporation r. 9 in M1 is the *rds*, dissociation is a fast preceding equilibrium step leading to $[O^-] \propto p(O_2)^{1/2}$. Correspondingly, the overall $p(O_2)$ dependence of ${}^1\Re_i$ is $1/2$ minus the decrease caused by the $p(O_2)$ dependence of involved defects. Interestingly, when the incorporation r. 10 in M2 is the *rds*, a different overall $p(O_2)$ dependence is obtained because adsorbed O^- is formed in a different pre–equilibrium and $[O^-] \propto p(O_2)^1$. The $p(O_2)$ dependence of ${}^2\Re_i$ is one minus the decrease caused by the involved defects. While this case is in principle possible, it is not considered here as a highly probable case (${}^2\Re_{da}$ and ${}^2\Re_i$ both require encounter of adsorbed oxygen species and $V_O^{\bullet\bullet}$, and a higher surface coverage is expected for O^- than for adsorbed molecular oxygen species; *cf.* discussion in [62]).

The values for $\Re_i$ and $\Re_{da}$ can be obtained from the measured isotope fractions at the reactor outlet (assuming that $[{}^{18}O_{ad}]$ is at steady state and $[O_2] \ll [O_O^x]$):

$$\frac{d^{36}f_g}{dt} = -\frac{2\,{}^1\Re_{da} S}{n_O}\left({}^{36}f_g - {}^{18}f_{ad}^2\right)$$

M1
$${}^{36}f_{g,e} = B\exp\left(\frac{-2\tau S\,{}^1\Re_0}{n_O}\right) + \left({}^{36}f_{g,i} - B\right)\exp\left(\frac{\tau S\,{}^1\Re_0\,{}^1\Re_i}{\left({}^1\Re_0 - {}^1\Re_i\right)n_O}\right) \qquad \text{eq. 27}$$

$$B = \frac{\left({}^{18}f_{g,i}\,{}^1\Re_0\right)^2}{{}^1\Re_i\left(2\,{}^1\Re_0 - {}^1\Re_i\right)}$$

M2
$$\frac{d^{36}f_g}{dt} = -\frac{2\,{}^2\Re_{da} S}{n_O}\,{}^{36}f_g \Leftrightarrow {}^2\Re_{da} = \frac{n_O}{2S\tau}\ln\left(\frac{{}^{36}f_{g,i}}{{}^{36}f_{g,e}}\right) \qquad \text{eq. 28}$$

In eq. 27 and eq. 28 ${}^{36}f_{g,i}$ and ${}^{36}f_{g,e}$ are the gas phase fraction of ${}^{36}O_2$ in the pulse at the inlet and exit of the reactor, and n_O the molar amount of oxygen atoms in the gas phase. With eq. 18, and eq. 25 to eq. 28 it is possible to deconvolute the exchange rates for $\Re_{da}$ and $\Re_i$ from $\Re_0$. However, depending on the actual sample behavior the faster of these two rates may carry a rather large uncertainty.

This separation of $\Re_0$ into $\Re_{da}$ and $\Re_i$ depends sensitively on the formation of ${}^{34}O_2$. If the formation of ${}^{34}O_2$ is large $\Re_i$ becomes small in M1 and M2 and shows a very large error which makes $\Re_i$ not reliable anymore.

3 EXPERIMENTAL DETAILS

3.1 Sample Synthesis

3.1.1 Doped Ceria and Zirconia Samples

Doped ceria and zirconia samples were prepared wet chemically by a Pechini type approach to ensure homogeneous distribution of the dopants[15, 63, 64].

Single– and co–doped ceria was synthesizes using $Me(NO_3)_3$ x H_2O (with Me: Ce, Gd, Pr, and Tb; REacton, Alfa Aesar, 99.99 %) and $NH_4NbC_2O_4$ • xH_2O (Aldrich, 99.99 %) in the desired molar ratios. For Pr–doped zirconia, $ZrO(NO_3)_2$ • xH_2O (Aldrich, 99.99 %) was used as reagent. The exact water content was determined by thermogravimetric analysis. The metal salts, citric acid (CA) (Roth, >99.5 %), ethylene glycol (EG) (Emsure, Merck), and a few droplets of HNO_3 (Roth, *p.a.*) were dissolved in a glass beaker with approximately 60 – 100 mL distilled water. The molar ratio of EG/CA was two, and EG/metal one. The reaction mixture was stirred at 175 °C until a resin was formed (the resin was yellowish in case of doped ceria and white in case of doped zirconia). A 5 L glass beaker, with a hole at the bottom and covered by alumina foil at the top, was placed on top of the reaction vessel in order to capture the fluffy, voluminous product which was formed when pyrolysis at approximately 250 °C was performed. The obtained powder was homogenized by dry milling in a zirconia ball mill for 30 – 45 minutes and calcined at 800 °C for 8 h in air. The samples are labeled according to table 2.

Table 2: Sample abbreviations and their composition used in this study.

Sample	Composition	Sample	Composition
06PDC	$Ce_{0.994}Pr_{0.006}O_{2-\delta}$	06GDC	$Ce_{0.994}Gd_{0.006}O_{2-\delta}$
2PDC	$Ce_{0.98}Pr_{0.02}O_{2-\delta}$	2GDC	$Ce_{0.98}Gd_{0.02}O_{2-\delta}$
6PDC	$Ce_{0.94}Pr_{0.06}O_{2-\delta}$	6GDC	$Ce_{0.94}Gd_{0.06}O_{2-\delta}$
20PDC	$Ce_{0.80}Pr_{0.20}O_{2-\delta}$	20GDC	$Ce_{0.80}Gd_{0.20}O_{2-\delta}$
6TDC	$Ce_{0.94}Tb_{0.06}O_{2-\delta}$	20TDC	$Ce_{0.80}Tb_{0.20}O_{2-\delta}$
2P6GD	$Ce_{0.92}Gd_{0.06}Pr_{0.02}O_{2-\delta}$	6P2GDC	$Ce_{0.92}Gd_{0.02}Pr_{0.06}O_{2-\delta}$
6P14GDC	$Ce_{0.80}Gd_{0.14}Pr_{0.06}O_{2-\delta}$	14P6GDC	$Ce_{0.80}Gd_{0.06}Pr_{0.14}O_{2-\delta}$
11PNDC	$Ce_{0.78}Pr_{0.11}Nb_{0.11}O_{2-\delta}$	6PNDC	$Ce_{0.88}Pr_{0.06}Nb_{0.06}O_{2-\delta}$
2PNDC	$Ce_{0.96}Pr_{0.02}Nb_{0.02}O_{2-\delta}$	2GNDC	$Ce_{0.96}Gd_{0.02}Nb_{0.02}O_{2-\delta}$
2NDC	$Ce_{0.98}Nb_{0.02}O_{2-\delta}$	2PDZ	$Zr_{0.98}Pr_{0.02}O_{2-\delta}$
6PDZ	$Zr_{0.94}Pr_{0.06}O_{2-\delta}$	15PDZ	$Zr_{0.85}Pr_{0.15}O_{2-\delta}$
06STF	$SrFe_{0.006}Ti_{0.994}O_{3-\delta}$	2STF	$SrFe_{0.02}Ti_{0.98}O_{3-\delta}$
6STF	$SrFe_{0.06}Ti_{0.94}O_{3-\delta}$	20STF	$SrFe_{0.20}Ti_{0.80}O_{3-\delta}$

From now on, the sample history will differ, depending on which experiment is planned (exceptions will be mentioned in the respective chapters).

(i) For UV–Vis spectroscopy, thermogravimetric analysis (determining the oxygen stoichiometry), and for water and carbon dioxide adsorption the calcined powders were used.

(ii) For carbon monoxide and methane oxidation, carbon dioxide adsorption and pulsed carbon monoxide oxidation the calcined powders were sieved to 60 – 100 µm in order to break agglomerates.

(iii) For electrochemical impedance spectroscopy and isothermal isotope exchange line profiling, 1 g of the calcined powder was compacted into a dense pellet by isostatic pressing in a silicon rubber mold (ø 10 mm) at 300 kN. The green body was sintered at 1400°C for 24 h in air with a heating/cooling rate of 200 °C h^{-1}. A theoretical density between 96 – 98 % was achieved by this procedure.

(iv) For *in situ* carbon monoxide oxidation conducted with electrochemical impedance spectroscopy, 0.5 g of the calcined powder was compacted by isostatic pressing at 250 kN in a silicon rubber mold (ø 10 mm). The green body was sintered at 850 °C for 8 h with 100 °C h^{-1} to achieve a porous sample with a mean theoretical density of 72 %.

(v) For *in situ* carbon monoxide oxidation measurements by thermogravimetric analysis 1 g powder was compacted into a dense pellet by spark plasma sintering (SPS; FCT-DP D 5/2, FCT Systeme). The sample was compacted at 1000 °C for 3 minutes in a graphite mold (ø 10 mm) with a heating/cooling rate of 200 °C min^{-1} at 6 kN pressure in 25 mbar Ar atmosphere. The pellet was annealed at 1400 °C for 8 h in air with a heating/cooling rate of 100 °C h^{-1}. The sintered pellets showed a theoretical density of 96 – 99 % and were crushed and sieved to a particle size of 60 – 100 µm and < 60 µm. The latter fraction was used for the experiments.

(vi) For pulsed isotope exchange, isothermal isotope exchange, mass relaxation, propan–2–ol test reactions, Raman spectroscopy, and energy dispersive X–ray spectroscopy the particles mentioned in (v) with the size distribution of 60 – 100 µm were annealed at 1400 °C with a heating/cooling rate of 200 °C h^{-1} in air. With this procedure a smooth and dense surface was obtained and the particle size did not change by this procedure and the pressure drop across the packed bed reactor was minute.

3.1.2 Iron Doped Strontium Titanate

Iron doped strontium titante was prepared by a solid state reaction. The corresponding amounts of $SrCO_3$ (Aldrich, >99.9 %), TiO_2 (Riedel-de Haën, >98 %), and Fe_2O_3 (Alfa Aesar, >99.85 %) were dry milled for 1 h in a zirconia mill and annealed at 1200 °C with 300°C min^{-1} in air for 20 h. The mixture was milled three times and after each grinding step, the powder was calcined at 1300 °C with 300 °C h^{-1} in air for 12 h.

3.2 General Sample Characteristics

3.2.1 Density Measurement

Density measurements were conducted on pellets (total mass > 1 g) with a 5 mL pycnometer (Gay-Lussac) in distilled water at 27 °C. The measured densities were already mentioned in section 3.1.1.

3.2.2 Surface Area Measurement

The surface area was determined using the Brunauer-Emmet-Teller (BET) theory. For high surface area samples, the BET–area was measured by an Autosorb–1 (Quantachrome Instruments) with N_2 as adsorbate. Prior to measurements, the samples were treated at 120 °C in vacuum to desorb adsorbates. For low surface area samples, the company POROTEC GmbH (Hofheim, Germany) was commissioned which uses Krypton as adsorbate.

3.2.3 X-Ray Photoelectron Spectroscopy

The surface of the ceramic particles was investigated by X–ray photoelectron spectroscopy (XPS) at room temperature with an AXIS Ultra (Kratos) with monochromatized Al Kα radiation with a base pressure $<10^{-10}$ mbar. The spectra were obtained with analyzer pass energy of 20 eV. The analysis was performed with CasaXPS by the interface analysis group of the Max–Planck–Institute for Solid Sate Research.

3.2.4 X-Ray Diffraction

Phase purity and lattice parameters were examined by X–ray diffraction with an Empyrean (Malvern Panalytical) diffractometer with Cu Kα radiation (40 kW, 40 mA, λ = 1.541874 Å) in Bragg–Brentano reflection geometry at room temperature with a PIXcel 3D detector. Lattice parameters were refined by the HighScore Plus (Malvern Panalytical) software.

3.2.5 Scanning Electron Microscopy

The topography of the surface of the samples was investigated by scanning electron microscopy with a Merlin Gemini II (Carl Zeiss).

3.2.6 Inductively Coupled Plasma Optical Emission Spectroscopy

The cation stoichiometry and trace impurities were checked by inductively plasma optical emission spectroscopy (ICP–ES, Spectro Ciros CCD, Spectro Analytical Instruments). Samples were dissolved in HF, and the measurements were performed at the Max–Planck–Institute for Intelligent Systems.

3.2.7 Energy Dispersive X-Ray Spectroscopy

Segregation effects to grain boundaries were investigated by transmission electron microscopy (TEM) coupled with energy–dispersive X–ray spectroscopy (EDX) with an ARM 200CF (JEOL) and a Centurio EDX detector (200kV, probe size 1.2 Å). Measurements were performed by the Stuttgart Center for Electron Microscopy (StEM) at the Max–Planck–Institute for Solid State Research.

3.2.8 UV-Vis Spectroscopy

UV-Vis spectroscopy was performed with a Cary Series UV–Vis–NIR spectrometer (Agilent Technologies) in diffuse reflectance mode with a reduced slit height and a scan rate of 600 nm min^{-1} with a resolution of 1 nm on calcined ceramic powders diluted with 75 % zirconia (TZ-0, TOSOH) from 800 – 200 nm at room temperature. Prior to reflectance measurements, baseline and background correction was performed with a blank sample (total reflection) and with a blocked beam line (zero reflection). Reflectance spectra were converted by the Kubelka-Munk function $f(R_\infty)$ according to:

$$f(R_\infty) = \frac{(1 - R_\infty)^2}{2R_\infty} = \frac{\kappa}{B} \qquad \text{eq. 29}$$

In eq. 29, κ is the absorption coefficient, B the scattering coefficient, and R_∞ is the absolute reflectance of an infinitely thick sample.

3.2.9 Raman Spectroscopy

Raman spectroscopy was performed with a Jobin Yvon Typ V 010 LabRAM (HORIBA) single grating spectrometer with a resolution of approx. 1 cm^{-1} at room temperature. The light beam – a linear polarized He/Ne gas laser with λ = 633, 532, and 457 nm with <1 mW power – was focused on top of the particle surface by a microscope (spot size approx. 10 µm). Spectra were recorded by the spectroscopy service group in the department of Solid State Spectroscopy of the Max–Planck–Institute for Solid State Research.

3.3 Electrochemical Impedance Spectroscopy

A platinum layer with a thickness of approximately 300 nm was sputtered on the upper and bottom surface of the sample. At low temperature, this Pt layer can be considered as ion–blocking electrode, but at high temperatures, oxygen exchange will take place. For *in situ* carbon monoxide oxidation, Au was used as electrode due to its lower catalytic activity. The samples were then placed into a spring loaded quartz glass sample holder as depicted in figure 6.

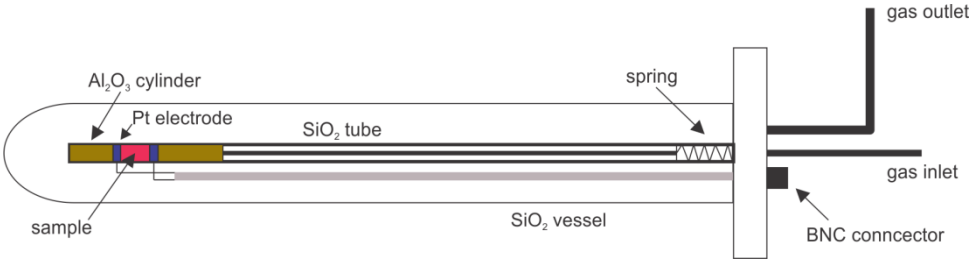

Figure 6: Sample holder used in electrochemical impedance spectroscopy experiments.

Electrochemical impedance spectroscopy is a technique which allows the distinction of processes which proceed at different time scales (*e.g.,* bulk *vs.* grain boundary conductivity). An alternating voltage is applied to the sample and amplitude and phase shift of the resulting current are measured, and the complex impedance Z can be calculated. Usually, the negative imaginary part of the impedance is plotted versus the real part in a so–called Nyquist plot. Analysis of the Nyquist plots was done by ZView (Scribner Associates Inc.). If the processes in the sample show different time constants, they are recognized as distinct semicircles. The analysis is performed by fitting to equivalent circuits (capacitors and resistors connected in series or parallel) which correspond to the electrochemical processes

in the sample. Due to non-homogeneity (rough or porous surface), a so–called constant phase element (CPE) was used in the equivalent circuits instead of a capacitor. The capacitance can be calculated according to ref.[65]:

$$C = (R^{1-P}Q)^{1/P} \quad \text{eq. 30}$$

In eq. 30, C is the capacitance, R is the resistance, P and Q are the exponent and admittance constant of CPE, respectively. Specific conductivities (σ) were calculated by eq. 31 and specific grain boundary conductivities ($\sigma_{\mathrm{GB}}^{\mathrm{spec}}$) were calculated according to eq. 32[66]:

$$\sigma = \frac{1}{R}\frac{L}{S} \quad \text{eq. 31}$$

$$\sigma_{\mathrm{GB}}^{\mathrm{spec}} = \frac{1}{R_{GB}}\frac{L}{S}\frac{C_B}{C_{GB}} \quad \text{eq. 32}$$

R_{GB} is the resistance of the grain boundary semicircle, L, and S are the thickness and area of the sample, C_B, and C_{GB} are the bulk and grain boundary capacitance, respectively (brick layer model). The space charge potential ($\Delta\varphi$) was calculated by solving eq. 33[65] numerically where ω_B and ω_{GB} denotes the peak frequency of the bulk and grain boundary arc, respectively. The elementary charge is denoted by e and k_{B} is Boltzmann's constant.

$$\frac{\omega_B}{\omega_{GB}} = \exp\left(\frac{e\Delta\varphi}{k_{\mathrm{B}}T}\right)\frac{k_{\mathrm{B}}T}{2e\Delta\varphi} \quad \text{eq. 33}$$

A Novocontrol Alpha–A high performance frequency analyzer was used for measuring the impedance spectra. The setup of the frequency analyzer is given in table 3. Gas mixtures were adjusted with mass flow controllers and the composition was checked by the oxygen measuring module ZR5 (Zirox GmbH).

Table 3: Parameters used for impedance spectroscopy

Parameter	Value
Frequency range	50 mHz to 1 MHz
Data points per decade	10 to 20
Integration time	2 s, or at least two periods
Output voltage	0.1 V
Reference calibration	yes

3.4 Propan-2-ol dehydration/dehydrogenation

Propan-2-ol dehydration/dehydrogenation experiments were performed with the setup depicted in figure 7.

The reaction takes place in a temperature controlled quartz glass packed bed reactor (PBR) with an inner diameter of 8 mm and a SiO_2 frit in order to fix the ceramic particle bed. The feed gas enters the reactor at the top. The part before the PBR with several mass flow controllers (MFC, calibrated by a bubble flow meter) is necessary to mix appropriate gas concentrations for calibration. A temperature controlled evaporator (E) is used to adjust the gas phase concentrations of the liquid reactants and products of the reaction.

Approximately 1 g ceramic particles with a size rang between 60 – 100 µm were placed into the PBR (bed height approximately 5 mm). Nitrogen was selected as carrier gas and enters E, filled with propan-2-ol, at 13.4 °C (saturating pressure p_{sat} = 29 mbar) with a volumetric flow rate of 10 mL min^{-1}. The resulting feed gas has a fraction of propan-2-ol of 2.86 % and enters the PBR. The pressure drop across the packed bed was always below 10 % in the temperature regime 250 - 400 °C.

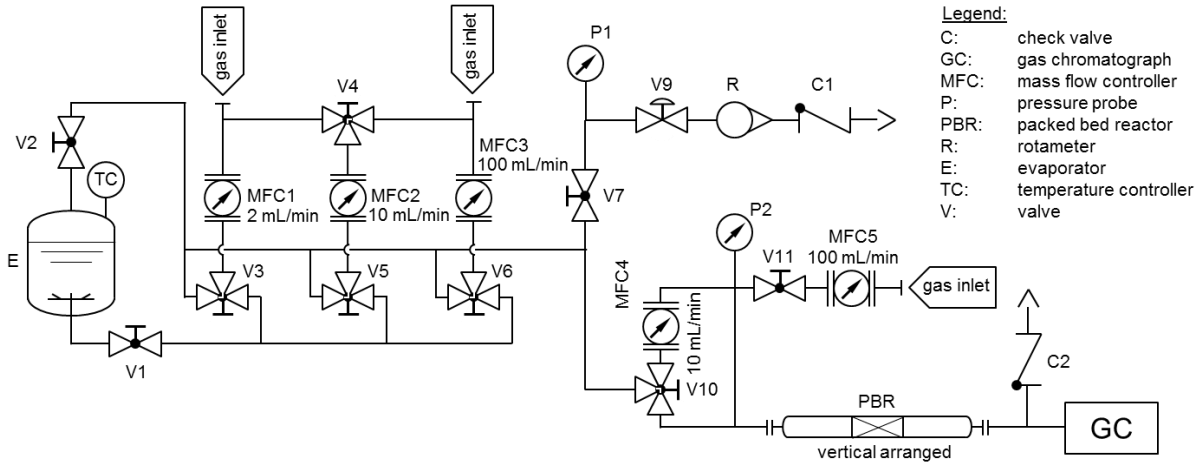

Figure 7: Pipping and instrumentation diagram of the experimental setup for propan-2-ol dehydration/dehydrogenation measurements.

Gas phase analysis was performed by an Agilent 300A Micro Gas Chromatograph (GC). The GC system is equipped with thermal conductivity detectors and two columns:

(i) Column 1 (Channel B): OV–1, bonded and crosslinked non–polar dimethyl silicone capillary column, separation of non–polar compounds.

(ii) Column 2 (Channel C): HP-PLOT Q, bonded polystyrene-divinylbenzene, separation of non–polar and weakly polar compounds, 8 m x 320 µm x 10 µm.

In table 4, the retention times and column types for the analyzed reactants and products are given. The used parameters for each column are listed in table 5.

Table 4: Analyzed compounds by the Agilent 300A Micro GC, their retention times, supplier and purity.

Column	Compound	Retention time / s
OV-1	CO_2, Westfalen AG, 4.5 CO_2, 5.0 Ar	39
OV-1	Distilled H_2O	74
OV-1	Propene, Westfalen AG, min. 99.5 %	114
PLOT-Q	Propanone, BASF VLSI Selectipur	118
PLOT-Q	Propan-2-ol, BASF VLSI Selectipur	123

Table 5: Aligent 300A Micro GC instrument setup.

Parameter	OV1 / Channel B	PLOT Q / Channel C
Inject time	20 ms	20 ms
Post run time	180 s	180 s
Sample pump	timed, 60 s	timed, 60 s
Sample inlet temperature	100 °C	100 °C
Injector temperature	100 °C	100 °C
Column temperature	75 °C	60 °C
Pressure equilibration time	60 s	60 s
Column pressure	25 psi	25 psi
Post run pressure	35 psi	35 psi

Prior to propan-2-ol dehydration/dehydrogenation experiments, the sample was pre–treated with 10 mL min^{-1} N_2 in the PBR at 550 °C for 1 h with a heating and cooling rate of 10 °C min^{-1}. During reaction, the exiting gas was analyzed in increments of 10 min with the GC, and each temperature was held for 1 h.

The GC was calibrated with propan-2-ol, propanone, and water by using the evaporator. Propene and CO_2 were calibrated by using bottled gas. The calibration curves are given in figure 8 for propan-2-ol, propanone, and H_2O, and in figure 9 for propene and CO_2. The error bars are smaller than the symbols. For each concentration, a mean peak area was obtained originated from six measurements. All calibrations show almost perfectly linear correlation.

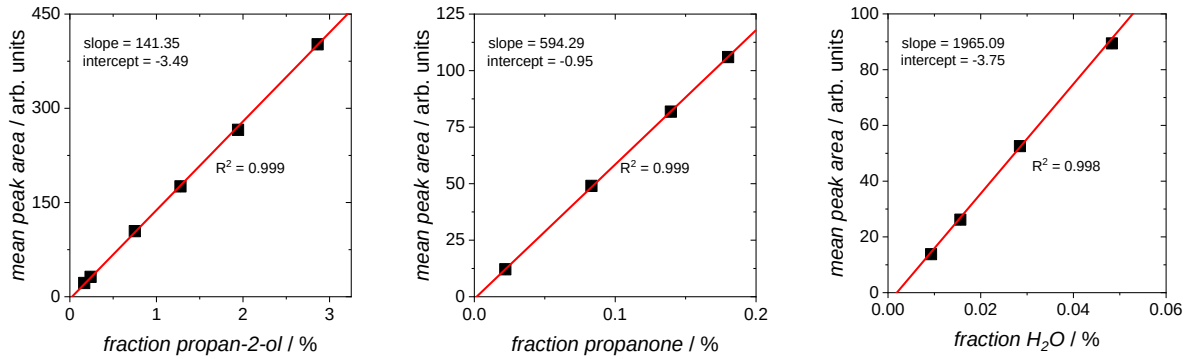

Figure 8: Calibration curves for propan-2-ol, propanone and H_2O. The error bars are smaller than the symbols.

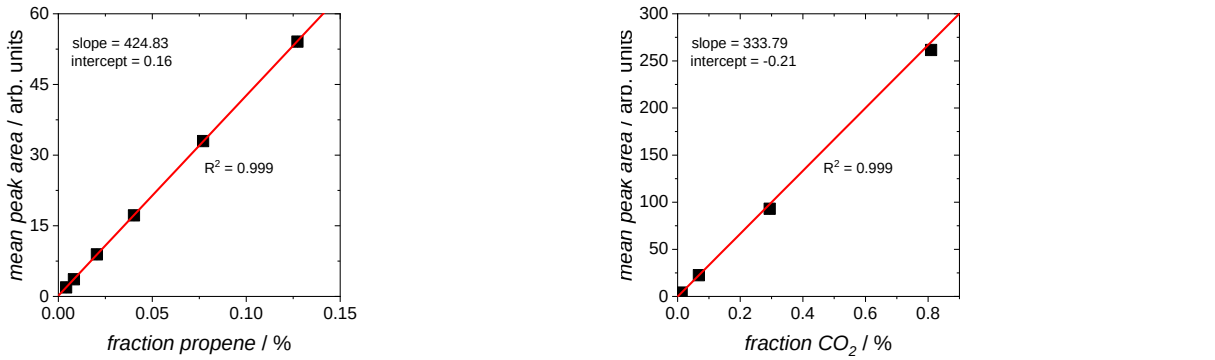

Figure 9: Calibration curves for propene and CO_2. The error bars are smaller than the symbols.

3.5 Isothermal isotope Exchange Line Profiling

Isotope exchange line profiling was performed on isostatically pressed and sintered pellets. The pellets were cut into halves (figure 11, a) and the large faces were polished with a 1 µm diamond suspension (Winter, Diapalst Suspension D1) and cleaned for 5 min with propan-2-ol in an ultrasonic bath.

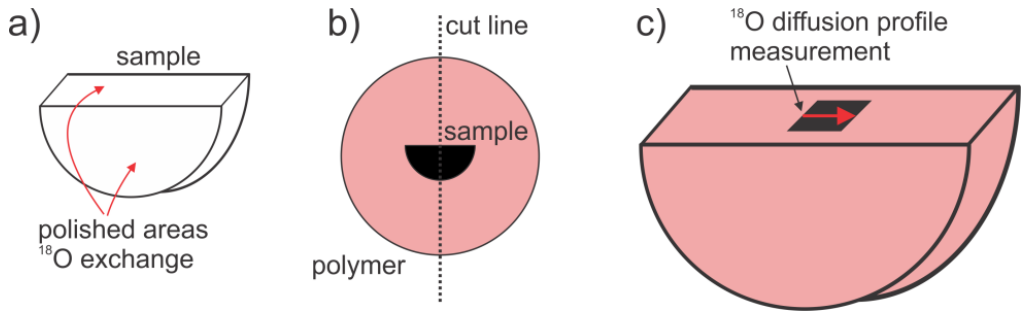

Figure 10: Schematics of sample preparation and the measurement of ^{18}O profile.

As depicted in figure 11, the sample was placed on gold foil and then placed into a quartz glass tube (inner diameter ≈ 13 mm, length ≈ 300 mm) connected to a gateway with ^{18}O and ^{16}O feed and a turbo-molecular pump.

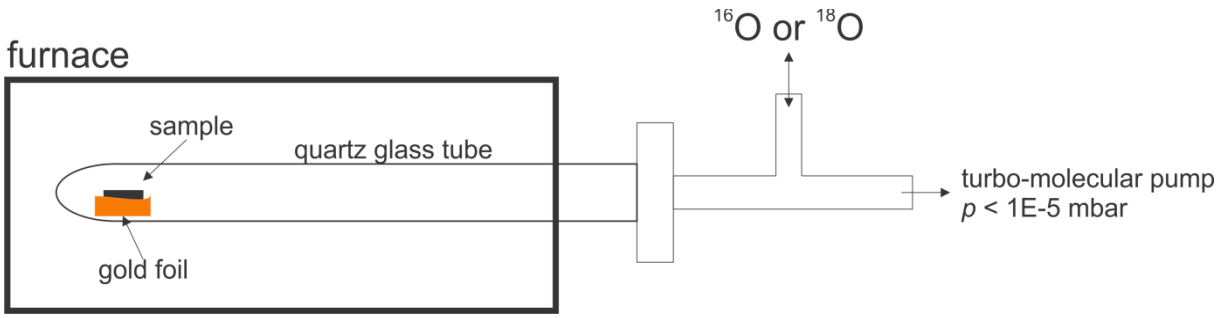

Figure 11: Schematics of the experimental setup up for isotope exchange line profiling experiment.

The tube with the sample was evacuated to approximately 10^{-5} mbar for 20 min and filled by $^{16}O_2$ gas (Westfalen, technical grade, higher purity shows an accumulation of ^{18}O above natural background) to a pressure of 200 mbar. The

sample was equilibrated at this oxygen pressure at certain temperature for a certain equilibration time (see table 6), and quenched to room temperature (usually quenching proceeds within 3 min). After evacuating to approximately 10^{-5} mbar for 20 min, the setup was filled by $^{18}O_2$ to a pressure of 200 mbar and was rapidly heated again to the annealing temperature (usually within 4 – 5 min).

Table 6: Parameters for Isotope Exchange Line Profiling

Sample	T / °C	Equilibration time / h	^{18}O exchange time / min
20GDC	550	12	240
	600	8	120
	650	5	60
	700	4	30
	800	4	30
20PDC	500	6	120
	550	5	60
	600	4	20
	700	4	15

The time the sample is allowed to exchange ^{16}O with ^{18}O was counted from 5 °C below the desired temperature. After a defined exchange time (table 6), the sample was quenched to room temperature and embedded into a conducting polymer (figure 10, b) based on modified methyl methacrylate and dendritic copper particles (Kulzer, Technovit 5000). The embedded sample was cut perpendicular to the large face and polished again.

The measurement of the ^{18}O diffusion profile (figure 10, c) was performed by Time of Flight Secondary Mass Spectrometry (ToF–SIMS, TOF.SIMS^5, IONTOF GmbH, parameters in table 7) by the interface analysis group of the Max–Planck–Institute for Solid State Research.

Table 7: Parameters for ToF-SIMS.

Polarisation	Primary gun	Sputter gun	Probed area	Pixel
negative	Bi, 30 keV	Cs, 2 keV	500 µm^2	512^2

The diffusion profile was evaluated according to eq. 34 for one–dimensional diffusion in a semi–infinite medium (see, *e.g.,* Crank[67]) by a least square fitting routine in Matlab.

$$\frac{f(x,t)-f_{\mathrm{bg}}}{f_{\mathrm{g}}-f_{\mathrm{bg}}}=\operatorname{erf}\left(\frac{x}{2\sqrt{D^{*}t}}\right)-\operatorname{erf}\left(\frac{k^{*}}{D^{*}}x+\left(\frac{k^{*}}{D^{*}}\right)^{2}D^{*}t\right)\operatorname{erf}\left(\frac{x}{2\sqrt{D^{*}t}}+\frac{k^{*}}{D^{*}}\sqrt{D^{*}t}\right) \qquad \text{eq. 34}$$

In eq. 34, $f(x)$ is the ^{18}O fraction obtained form ToF-SIMS, f_{bg} is the natural background level of ^{18}O in the sample (≈ 0.2 %), f_{g} the ^{18}O fraction in the gas phase, x the distance, t is the exchange time, D^{*} is the tracer diffusion coefficient, and k^{*} the tracer oxygen surface exchange coefficient.

3.6 Thermogravimetry

Thermogravimetric analysis (TGA) was performed with a STA 449 C Jupiter (Netzsch) coupled with a quadrupole mass spectrometer (Balzers Prisma QMS200 F1, Pfeiffer Vacuum).

Measurements were carried out typically with 0.25 – 2 g of sample placed in an Al_2O_3 crucible. The volumetric flow rate through the TGA was adjusted to 30 mL min^{-1} (*in situ* CO/CH_4 oxidation) and 60 mL min^{-1} (oxygen non-stoichiometry, H_2O/CO_2 adsorption, and mass relaxation experiments) where a share of 10 mL min^{-1} was the so–called *protective gas* (N_2) running through the balance. To correct for buoyancy effects, the mass change of an empty Al_2O_3 crucible was measured at appropriate heating/cooling rates and gas compositions, and was subtracted from the weight change of the sample. Details for the different experiments performed by TGA are listed in the following.

3.6.1 Determination of the Oxygen Non-Stoichiometry

For determining the oxygen non–stoichiometry, the samples (calcined powders) were first heated to the maximum temperature (800 °C or 900 °C) with a heating rate of 10 °C min^{-1} and then cooled down with the appropriate rate (to ensure equilibrium) given in table 8. To quantify the oxygen non–stoichiometry, the mass of the sample at the lowest temperature was set to the theoretical value of the oxygen content where all Pr or Ce are in their 4+ valance state. The oxygen partial pressure was controlled by mixing bottled gas – 0.1 % in N_2, 1 % O_2 in N_2, 100 % O_2 – with N_2 (5.0 O_2 and 5.0 N_2, Westfalen) by mass flow controllers.

Table 8: Weight-in of samples and temperature programs used in TGA experiment.

Sample	m / g	$p(O_2)$ / %	Temperature program / °C and °C min^{-1}
20PDC	0.301	83	$800 \xrightarrow{2} 600 \xrightarrow{1} 500 \xrightarrow{0.7} 400 \xrightarrow{0.3} 300$
		8.3	$800 \xrightarrow{2} 600 \xrightarrow{1} 500 \xrightarrow{0.7} 400 \xrightarrow{0.3} 300$
		0.83	$800 \xrightarrow{2} 600 \xrightarrow{1} 500 \xrightarrow{0.7} 400 \xrightarrow{0.3} 300$
		0.083	$800 \xrightarrow{2} 600 \xrightarrow{1} 500 \xrightarrow{0.7} 400 \xrightarrow{0.3} 300$
		0.0083	$800 \xrightarrow{0.6} 600 \xrightarrow{0.3} 500 \xrightarrow{0.2} 400 \xrightarrow{0.1} 300$
6PDC	0.570	83	$800 \xrightarrow{2} 600 \xrightarrow{1} 500 \xrightarrow{0.7} 400 \xrightarrow{0.3} 300$
		0.83	$800 \xrightarrow{2} 600 \xrightarrow{1} 500 \xrightarrow{0.7} 400 \xrightarrow{0.3} 300$
		0.0083	$800 \xrightarrow{0.6} 600 \xrightarrow{0.3} 500 \xrightarrow{0.2} 400 \xrightarrow{0.1} 300$
2PDC	2.069	83	$800 \xrightarrow{1.5} 600 \xrightarrow{0.5} 500 \xrightarrow{0.2} 400 \xrightarrow{0.1} 350$
		0.83	$800 \xrightarrow{1.5} 600 \xrightarrow{0.5} 500 \xrightarrow{0.2} 400 \xrightarrow{0.1} 350$
		0.0083	$800 \xrightarrow{0.3} 600 \xrightarrow{0.2} 500 \xrightarrow{0.1} 400$
20TDC	0.569	83	$900 \xrightarrow{1} 600 \xrightarrow{0.6} 400 \xrightarrow{0.3} 300$
		0.83	$900 \xrightarrow{1} 600 \xrightarrow{0.6} 400 \xrightarrow{0.3} 300$
		0.0083	$900 \xrightarrow{0.5} 600 \xrightarrow{0.3} 500 \xrightarrow{0.2} 400 \xrightarrow{0.1} 300$

3.6.2 Mass Relaxation

To determine the chemical oxygen exchange coefficient k^{δ}, relaxation experiments at different oxygen partial pressures and temperatures were conducted. The oxygen partial pressure was controlled as already mentioned in section 3.6.1.

The ceramic sample particles with a diameter of 60 – 100 µm are heated in defined oxygen partial pressure and temperature until equilibrium is reached (no mass change). An abrupt switch of the oxygen partial pressure was applied and the mass change was analyzed according to, *e.g.*, Crank's solution of a surface reaction on spheres[67] (eq. 35, diffusion is not rate limiting and therefore negligible).

$$\frac{m(t) - m_{\mathrm{eq}}}{m(t=0) - m_{\mathrm{eq}}} = \exp\left(-\frac{3k^{\delta}t}{r_{\mathrm{p}}}\right) \qquad \text{eq. 35}$$

In eq. 35, $m(t)$ is the mass at time t, $m(t=0)$ is the mass of the sample prior to relaxation, m_{eq} is the mass after relaxation when the sample is in equilibrium, r_{p} is the mean particle radius (≈ 40 µm), and with the factor 3, spherical particles are assumed as approximation. Usually, the change of oxygen partial pressure was performed from low to higher values where it is assumed that the step change in oxygen partial pressure is sufficiently small to get a linear response.

The relaxation experiments were performed between 500 – 700 °C and at $p(O_2)$ changes from 0.01 – 0.1 %, 0.1 – 1 %, and 1 – 10 % with 100 mg sample.

3.6.3 *In Situ* Carbon Monoxide and Methane Oxidation

For *in situ* CO oxidation, the gas composition was set to 1 % O_2 and 1 % CO mixed from 10 % O_2 in N_2 (both 5.0, Westfalen) and 3 % CO in Ar (4.7 CO and 5.0 Ar, Westfalen).

For *in situ* CH_4 oxidation, a gas composition of 0.25 % CH_4 and 1 % O_2 was used, mixed from 5 % CH_4 in N_2 (4.5 CH_4, 5.0 N_2 Westfalen) and 10 % O_2 in N_2.

The measurements were conducted with a sample load of 710 – 730 mg ceramic particles with a particle size below 60 µm. Mass changes were recorded in 1 % O_2 and in the appropriate CO/CH_4 concentrations plus 1% O_2 form high to low temperatures, whereby the temperature program was set to:

$$750\ °C \xrightarrow{2\ °C\ min^{-1}} 600\ °C \xrightarrow{1\ °C\ min^{-1}} 450\ °C \xrightarrow{0.6\ °C\ min^{-1}} 350\ °C \xrightarrow{0.3\ °C\ min^{-1}} 250\ °C$$

3.6.4 Carbon Dioxide and Water Desorption

Carbon dioxide and water desorption experiments were performed in N_2 (5.0, Westfalen) gas and with a sample mass of 270 – 290 mg of calcined powders. For H_2O adsorption, the gas was humidified by an evaporator filled with distilled H_2O at a temperature of 18 °C (saturated pressure p_{sat} = 21 mbar), and CO_2 adsorption took place at a partial pressure of 10 % CO_2.

The sample was pre–treated in N_2 at 1000 °C for 10 min in the TGA and cooled down with 20 °C min^{-1} to 50 °C to be sure that no adsorbed species is present at the surface of the sample. At 50 °C, H_2O or CO_2 were added to the gas stream until no change in mass could be observed. Water or CO_2 were disconnected from the gas stream and when the mass was constant, the sample was heated to 900 °C with 5 °C min^{-1} in order to desorb H_2O or CO_2.

3.7 Multifunctional Heterogeneous Reaction Setup

Pulsed isotope exchange (PIE), isothermal isotope exchange (IIE), carbon monoxide and methane oxidation (CMOX, MOX), pulsed carbon monoxide oxidation (PCMOX), and pulsed carbon dioxide adsorption (PCDA) experiments were conducted on a self–assembled and validated multifunctional heterogeneous reaction setup (MHRS). In figure 12, the piping and instrumentation is depicted and in figure 13, a photograph of the experimental setup is shown.

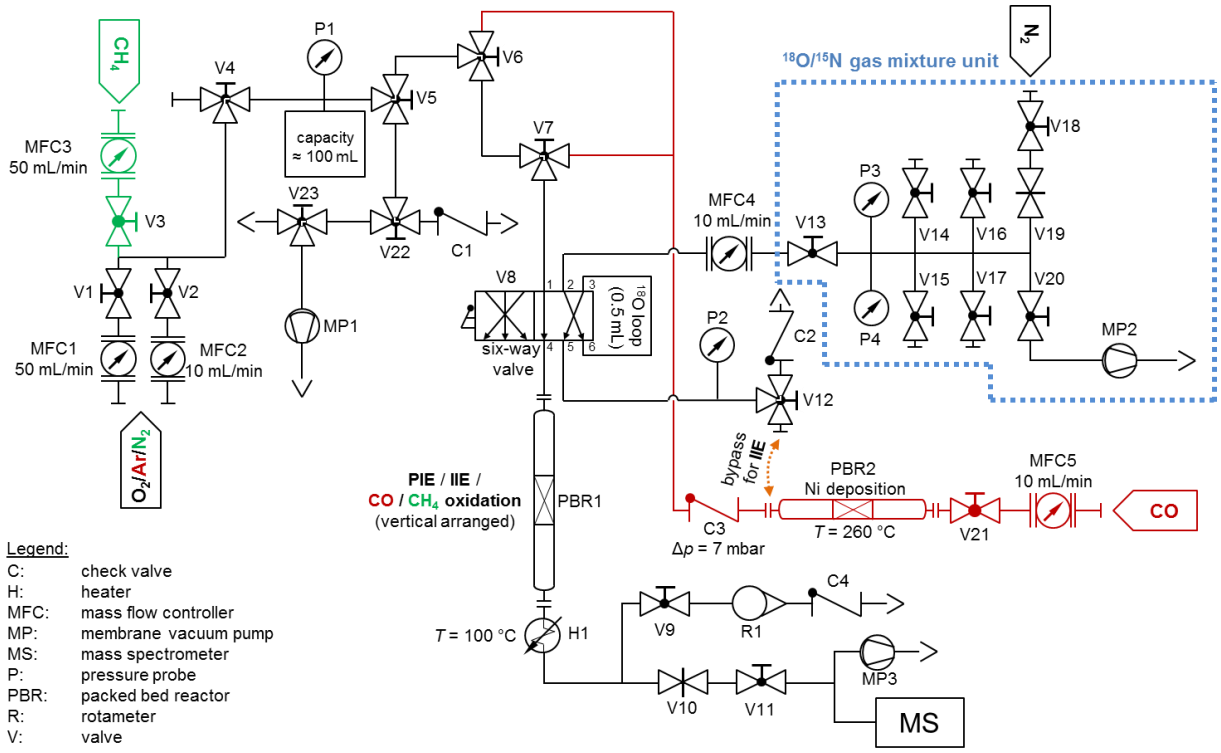

Figure 12: Pipping and instrumentation of the multifunctional heterogeneous reaction setup.

With MHRS it is possible to operate in a steady–state and a pulsed mode. The core of the MHRS is the packed bed reactor (PBR1) connected by Swagelok Ultra-Torr screw fittings to a six–way valve at the entrance, and to a mass spectrometer (MS, Balzers Prisma QME200, Pfeiffer Vacuum) at the exit. The pipes are mainly 1/8 inch, but the connection to the MS is 1/16 inch to minimize dead volume. Between PBR1 and MS, a heater (H1) is mounted in order to keep the exiting gas at constant temperature. The amount of gas which enters the MS can be determined by a rotameter (R1) and is adjusted by a needle valve (V10) connected after H1. The six-way valve is mounted to a large gas mixture part with four mass flow controllers (MFC1–3 & 5) were feeds of oxygen, nitrogen, argon, methane and carbon monoxide can be connected and mixed in desired ratios. All MFC were calibrated with a bubble flow meter.

For carbon monoxide oxidation measurements, a second packed bed reactor (PBR2, filled with SiO_2 wool) is required to deposit formed tetracarbonylnickel originating from the stainless steel pipes which contain some amounts of Ni. A check valve (C3) avoids other gases to enter PBR2.

The pressure probe (P1, PA-33X, KELLER Ges. für Druckmesstechnik mbH) before PBR1 enables one to determine the pressure drop across the packed bed. The capacity located at P1 is necessary in order to prevent pressure waves which can occur during pulsing due to the increasing pressure difference between P1 and

P2 (LEO2-Ei, KELLER Ges. für Druckmesstechnik mbH) at higher temperatures. The sample loop of the six-way valve has a volume of 0.5 mL and is connected to a second gas mixture unit, separated by a 10 mL mass flow controller (MFC4) where the pulse gas can be mixed and stored into 0.5 L lecture bottles.

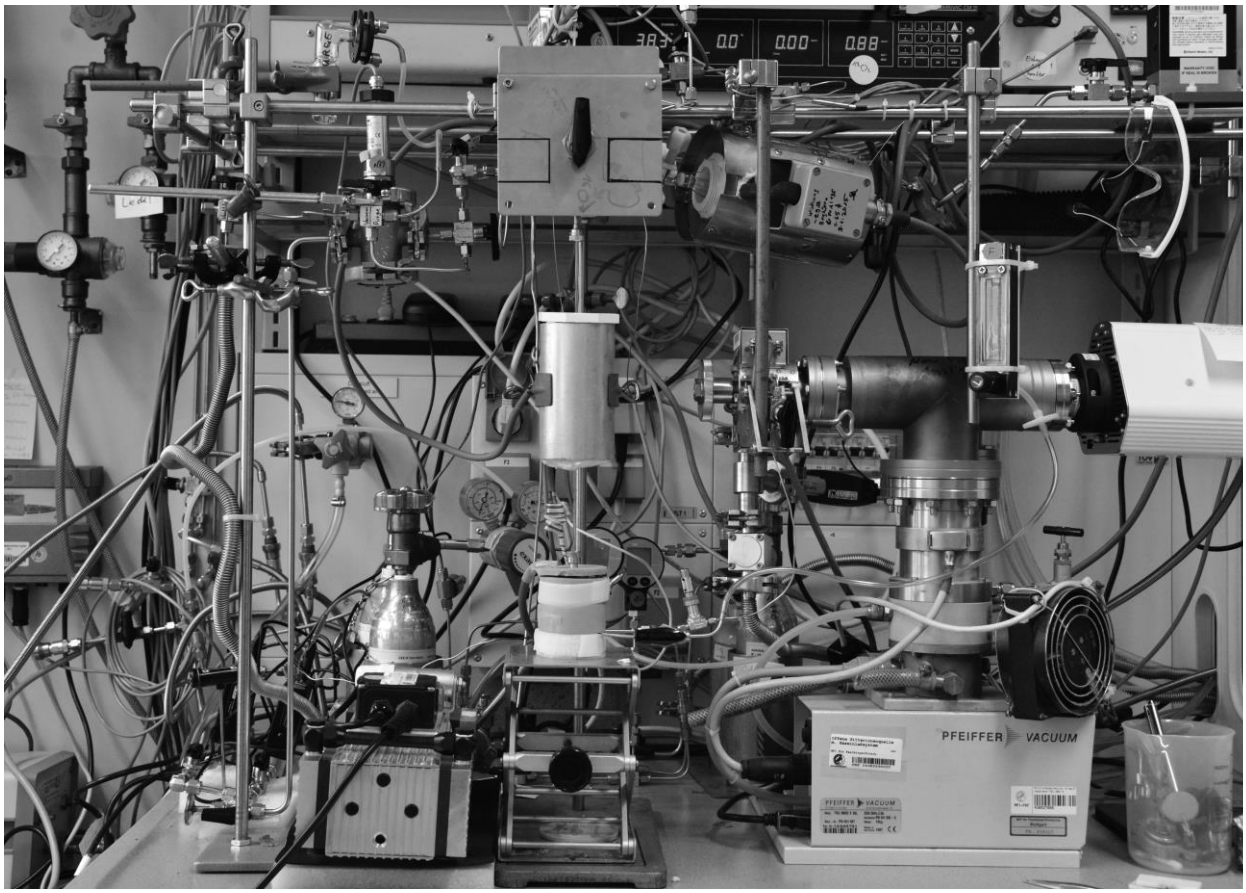

Figure 13: Photograph of the MHRS (March 2019)

With the possibility to bypass the sample loop of the six-way valve (bypass from valve V12 and check valve C3) it is possible to introduce an abrupt change in gas concentrations during steady–state measurements, necessary for isothermal isotope exchange experiments.

All experiments were conducted in gas tight Al_2O_3 tubes (Friatec GmbH, inner diameter 2 mm, thickness 0.5 mm, and length 300 mm). Temperature measurements were performed by a thermocouple placed close to the packed bed and fixed by a gold wire. The sample particles or powders were fixed by approximately 15 mg SiO_2 wool in the middle of the Al_2O_3 reactor. The SiO_2 wool was pre–treated in concentrated HNO_3 overnight and annealed at 800 °C for 4 h in air with a heating/cooling rate of 200 C h^{-1}.

A summary of gases and their purities used in the MHRS is given in table 9. Other experimental details for the different experiments conducted with MHRS are described in the following sections.

Table 9: Overview of the used gas types and purities for different experiments conducted with the multifunctional heterogeneous reaction setup.

Gas Type	Supplier	Purity	Experiment
Ar	Westfalen AG	5.0	CMOX, PCDA
N_2	Westfalen AG	5.0	PIE, MOX
20 % O_2 in Ar	Westfalen AG	5.0 O_2, 5.0 Ar	CMOX, PCMOX
10 % O_2 in N_2	Westfalen AG	5.0 O_2, 5.0N_2	PIE, MOX
1 % O_2 in N_2	Westfalen AG	5.0 O_2, 5.0N_2	PIE
0.1 % O_2 in N_2	Westfalen AG	5.0 O_2, 5.0N_2	PIE
1 % O_2 in He	Westfalen AG	5.0 O_2, 5.0N_2	PCMOX
5 % CO in Ar	Westfalen AG	4.7 CO, 5.0 Ar	CMOX, PCMOX
5 % CH_4 in N_2	Westfalen AG	4.5 CH_4, 5.0 N_2	MOX
5 % CO_2 in Ar	Westfalen AG	4.5 CO_2, 5.0 Ar	PCDA

3.7.1 Pulsed Isotope Exchange

Pulsed isotope exchange experiments were conducted on 100 mg ceramic particles with a size between 60 – 100 µm. The flow rate of the carrier gas – mixtures of 10, 1, and 0.1 % O_2 in N_2 – was set to 7 mL min^{-1} to keep the pressure drop across the packed bed below 20 %. The bed height was approximately 8 mm for all samples (exceptions will be mentioned in the respective chapters). Prior to isotope exchange, the sample in the packed bed reactor was pre–treated in the appropriated carrier gas at 900 °C for 30 min with a heating/cooling rate of 2.5 °C min^{-1}. The 0.5 mL sample loop of the six-way valve was used to introduce an ^{18}O enriched pulse with the same oxygen partial pressure as the carrier gas. The isotope enriched gas was mixed from 97 at% enriched ^{18}O gas (euriso-top), 97 at% enriched ^{15}N gas (Westfalen AG), and standard N_2 gas. ^{15}N was used to recognize the gas from the pulse loop and as internal standard, where the concentrations of ^{18}O and ^{15}N are similar. Prior to isotope exchange, the sample was equilibrated for 30 min in the carrier gas stream at each measurement temperature. The isotope enriched pulse was introduced by turning the six-way valve manually and the pulses were repeated three times with three minutes in–between. The pulse response was monitored by the mass spectrometer at m/z = 30 ($^{15}N_2$), 32 ($^{16}O_2$), 34 ($^{18}O^{16}O$) and 36 ($^{18}O_2$) with a resolution of five points per second.

For quantification, the peak areas A for each oxygen isotopologue i at reactor temperature T were normalized by the peak area of the $^{15}N_2$ signal (A_{30}).

$$N_i(T) = \left| \frac{A_i(T_R) - A_i(T)}{A_{30}(T)} \right| \qquad \text{eq. 36}$$

In eq. 36, T_R is the reference temperature where no oxygen isotope exchange occurs (usually $T_R \approx 25$ °C). The molecular oxygen isotope fractions f were calculated according to eq. 37.

$$^{32}f = \frac{N_{32}(T)}{\sum_i N_i(T)} + {}^{32}f_0 \qquad ^{34}f = \frac{N_{34}(T)}{\sum_i N_i(T)} + {}^{34}f_0 \qquad ^{36}f = \frac{N_{36}(T)}{\sum_i N_i(T)} + {}^{36}f_0 \quad -1 \qquad \text{eq. 37}$$

The parameter f_0 displays the initial molar fractions of the oxygen isotopologues in the 97 at% enriched ^{18}O gas prior to isotope exchange. The values for $^{32}f_0$, $^{34}f_0$, and $^{36}f_0$ can be calculated by assuming statistical equilibrium of the oxygen isotopologues (eq. 39) and are 0.001, 0.056 and 0.943. The total isotope fraction ^{18}f is obtained according to eq. 38.

$$^{18}f = {}^{36}f + 0.5\,{}^{34}f \qquad \text{eq. 38}$$

$$^{18}O^{18}O + {}^{16}O^{16}O \rightleftharpoons 2\,{}^{18}O^{16}O \qquad \frac{\left[\widehat{{}^{18}O^{16}O}\right]^2}{\left[\widehat{{}^{18}O_2}\right]\left[\widehat{{}^{16}O_2}\right]} = 4 \qquad \text{eq. 39}$$

3.7.2 Isothermal Isotope Exchange

Isothermal isotope exchange was conducted on 100 mg 20PDC particles (bed height was approximately 8 mm) with a size of 60 – 100 µm in 10 % O_2 atmosphere with a volumetric flow rate of 7 mL min^{-1}.

The sample was equilibrated in ^{18}O atmosphere for 6 h prior to an abrupt switch to ^{16}O. Gas phase analysis at the exit of the reactor was performed by mass spectrometry with m/z = 28 ($^{14}N_2$), 32 ($^{16}O_2$), 34 ($^{18}O^{16}O$) and 36 ($^{18}O_2$).

The fractions of ^{18}O and ^{16}O in the exiting gas were calculated with eq. 38. To calculate the tracer oxygen exchange coefficient k^*, the solution of diffusion into a sphere with surface reaction(see, *e.g.*, Crank[67]) was used by assuming that diffusion is not rate–limiting (eq. 40, for a derivation see, *e.g.*, ref. [68]).

$$\frac{M(t)}{M(t=\infty)} = 1 - \exp\left(-\frac{3k^*t}{r_p}\right) \qquad \text{eq. 40}$$

$M(t)$ is the accumulated ^{16}O in the sample at time t, and $M(t=\infty)$ the total amount of ^{16}O incorporated into the sample in equilibrium, and r_p represents the mean radius of the particles (here ≈ 40 µm). By using the factor 3 in the exponent of eq. 40, spherical particles are considered as an approximation.

3.7.3 Carbon Monoxide and Methane Oxidation

Carbon monoxide and methane oxidation were conducted on approximately 15 - 25 mg calcined powders with a bed height between 4 – 8 mm. Prior to CO/CH_4 oxidation measurements, the sample was pre–treated in the packed bed reactor in the appropriate carrier gas stream (but without CO or CH_4) for 30 min at 750 °C with a heating/cooling rate of 5 °C min^{-1}. For carbon monoxide oxidation, the carrier gas did not contain any nitrogen but argon to recognize the CO signal (N_2 and CO have the same m/z). For CH_4 oxidation, nitrogen was used instead.

Conversions of CO and CH_4 were measured as a function of $p(O_2)$, $p(CO)$, and $p(CH_4)$. The gas phase analysis was performed by mass spectrometry at the exit of the reactor:

(i) For CO oxidation: m/z = 28 (CO), 32 (O_2), 40 (Ar), 44 (CO_2).

(ii) For CH_4 oxidation: m/z = 15 (CH_3^+), 18 (H_2O), 28 (N_2), 32 (O_2), 44 (CO_2).

For methane oxidation the CH_3^+(m/z = 15) fragment was analyzed instead of CH_4^+ (m/z = 16) since the latter signal is influenced by oxygen. In order to not exceed a pressure drop across the packed bed of 20 %, the total volumetric flow rate was set to 10 mL min^{-1} ($p(O_2)$ experiment) and 25 mL min^{-1} (for $p(CO)$/ $p(CH_4)$ experiment). The gas composition was adjusted according to table 10 for CO oxidation and table 11 for CH_4 oxidation.

Table 10: Gas compositions and volumetric flow rates used for carbon monoxide oxidation measurements.

Gas Composition	20 % O_2 in Ar mL/min	5 % CO in Ar mL/min	Ar mL/min
1 % O_2 / 1 % CO	0.50	2.00	7.50
4 %O_2 / 1 % CO	2.00	2.00	6.00
10 %O_2 / 1 % CO	5.00	2.00	3.00
1 % O_2 / 0.3 % CO	1.25	0.50	23.25
1 %O_2 / 0.1 % CO	1.25	2.50	21.25

Table 11: Gas compositions and volumetric flow rates used for methane oxidation measurements.

Gas Composition	10 % O_2 in N_2 mL/min	5 % CH_4 in N_2 mL/min	N_2 mL/min
1 % O_2 / 0.25 % CH_4	1.00	0.50	8.50
3 %O_2 / 0.25 % CH_4	3.00	0.50	6.50
9.5 %O_2 / 0.25 % CH_4	9.50	0.50	0
5 % O_2 / 0.1 % CH_4	12.50	0.50	12.00
5 % O_2 / 0.3 % CH_4	12.50	1.50	11.00
5 % O_2 / 1 % CH_4	12.50	5.00	7.50

The quantification of CO, CO_2, CH_4, O_2 and H_2O was done by a linear two point calibration: at room temperature where no reaction takes place (the measured ion

currents are equal to the inlet gas concentrations) and at higher temperatures, where total conversion of CO and CH_4 occurs (concentrations of zero).

In case of CO oxidation, the exiting gas stream was analyzed additionally by a CO sensor (TOX Sens, Kohlenmonoxid 300 ppm, Endresss+Hauser) in order to check for full conversion at high temperatures.

Prior to calibration, the ion currents for CO (I_{CO}, in case of CO oxidation) and O_2 (I_{O_2}, in case of CH_4 oxidation) were corrected according to eq. 41 and eq. 42, in order to consider the fragmentation of CO_2 (I_{CO_2}) and H_2O (I_{H_2O}) in CO^+ and O^+ respectively.

$$I_{CO,corr} = I_{CO} - 0.11 I_{CO_2} \qquad \text{eq. 41}$$

$$I_{O_2,corr} = I_{O_2} - 0.01 I_{H_2O} \qquad \text{eq. 42}$$

3.7.4 Pulsed Carbon Monoxide Oxidation

Pulsed carbon monoxide oxidation was performed on the same samples with the same pre–treatment procedure already mentioned in section 3.7.3. The total volumetric flow rate of the carrier gas – a mixture of 1 % O_2 in He – was set to 10 mL min^{-1}. The 0.5 mL sample loop of the six-way valve was used to introduce a pulse with a composition of 1 % ^{18}O enriched oxygen (97 at% ^{18}O, euriso-top) and 1 % CO in argon. $^{15}N_2$ was not used here because it contains traces of $^{14}N_2$ which falsify the measured CO ion currents (same m/z).

Prior to pulsed carbon monoxide oxidation, the sample was equilibrated for 30 min in the carrier gas stream at each measurement temperature. The $^{18}O_2$/CO pulse was introduced at each temperature by manually turning the six-way valve. After pulsing and a delay of 10 minutes, the sample was heated to the next measurement temperature.

The pulse response was monitored by the mass spectrometer at m/z = 28 (CO), 32 ($^{16}O_2$), 34 ($^{18}O^{16}O$), 44 ($C^{16}O_2$), and 46 ($C^{16}O^{18}O$) with a resolution of four points per second. The oxygen isotopologue $^{36}O_2$ could not be quantified since the signal is influenced by Ar (^{36}Ar isotope).

3.7.5 Pulsed Carbon Dioxide Adsorption

Pulsed carbon dioxide adsorption experiments were conducted on approximately 5 mg calcined powders. The carrier gas was a mixture of 1 % O_2 in argon with a total volumetric flow rate of 10 mL min^{-1}.

The sample was pre–treated in the packed bed reactor in the carrier gas stream for 30 min at 600 °C with a heating/cooling rate of 5 °C min^{-1}. The 0.5 mL sample loop of the six–way valve was used to introduce a pulse with a composition of 1 % O_2, 1 % CO_2, and approximately 1 % $^{15}N_2$ (Westfalen, as internal standard) in argon.

The O_2/CO_2 pulse was introduced only once at each temperature by turning the six-way valve manually. After a delay of three minutes after pulsing, the sample was heated to 600 °C with 100 °C min^{-1} to desorb CO_2 and cooled down to the next measurement temperature with 10 °C min^{-1}.

The pulse response was monitored by the mass spectrometer at m/z = 30 ($^{15}N_2$), 32 (O_2) and 44 (CO_2) with a resolution of five points per second and the peak area of the CO_2 signal was normalized by the peak area of $^{15}N_2$. To quantify the amount of adsorbed CO_2 ($c_{CO_2,ad}$), eq. 43 was used.

$$c_{CO_2,ad}(T) = \frac{N_{CO_2,reactor} - N_{CO_2,sample}(T)}{N_{CO_2,reactor}} c_{CO_2,puls} \qquad \text{eq. 43}$$

The normalized CO_2 peak area obtained on an empty reactor ($N_{CO_2,reactor}$) was subtracted by the normalized area obtained with the ceramic sample powder ($N_{CO_2,sample}$) at temperature T multiplied by the amount of available CO_2 in the pulse ($c_{CO_2,puls}$).

4 RESULTS AND DISCUSSION

4.1 Specific Sample Characterization

4.1.1 Raman Spectroscopy

Materials with a fluorite-type crystal structure show only one allowed Raman phonon mode, which is the symmetric breathing mode of the lattice oxygen atom around each cation. For undoped ceria, this mode appears at approximately 465 cm^{-1}. McBride *et al.*[69] found experimentally (and confirmed by model calculations) that upon substitution of Ce^{4+} with a trivalent rare earth metal like La, Gd, Pr, or Tb a broad feature at about 570 cm^{-1} appears in the Raman spectra which is attributed to oxygen vacancies.

Interestingly, on Gd, Sm, Y, Lu, and La–doped ceria samples a second band at around 600 cm^{-1} appears simultaneously. This second mode originates from the different ionic radii of the dopant cations compared to Ce^{4+} (*e.g.,* 0.97 Å for Ce^{4+} and 1.05 Å for Gd^{3+}). The absence of the latter peak in case of Pr was explained due to the fact that in PDC, the majority of Pr is the 4+ state with a radius close to that of Ce^{4+} (0.96 *vs.* 0.97 Å).[70]

The ratio of the peak areas at the phonon modes 570 and 465 cm^{-1} (ratio of lattice oxygen to oxygen vacancies) displays the relative oxygen vacancy concentration in the bulk material.[71, 72] In principle, surface sensitive measurements are possible by Raman spectroscopy if the excitation energy is within the band gap of ceria ($E_g \approx 3.6$ eV (344 nm)).[72] However, due to the unavailability of an appropriate UV laser these measurements could not be conducted in the present study. Here, Raman spectroscopy was performed with annealed GDC and PDC particles (ø 40 µm) with an excitation wavelength of 633 nm (red laser).

The Raman spectra of Gd–doped ceria samples (figure 14a) clearly show the F_{2g} vibrational mode of the lattice oxygen and the two defect modes at 570 and 600 cm^{-1}, which is in line with literature findings on GDC powders conducted with the same excitation wavelength.[73] Qualitatively, a clear trend can be seen from figure 14a: the intensities of the defect modes increase with [Gd], indicating the increase of $[V_O^{\bullet\bullet}]$. Due to relative low intensities, a quantitative analysis was not performed here for GDC.

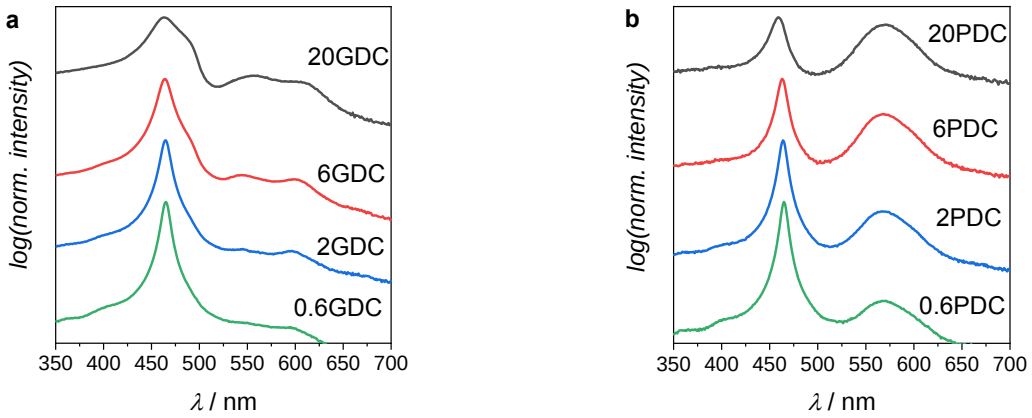

Figure 14: Logarithmic plot of the normalized Raman spectra for a) GDC and b) PDC particles. Spectra are vertically shifted for clarity.

A clearer result (which is in line with literature data, *cf.* ref.[69, 71, 74]), was obtained for PDC. As depicted in figure 14b, with increasing Pr dopant concentration the oxygen vacancy related mode at 570 cm^{-1} becomes more intense, and a linear relationship between the peak area ratio A_{570}/A_{465} with the Pr concentration was obtained (figure 15a). From this, it can be clearly stated that the oxygen vacancy concentration in PDC increases with [Pr].

Figure 15b displays the Raman spectra of Gd/Nb and Pr/Nb co-doped ceria together with 2NDC, 6PDC and 6GDC. For 2NDC, only the vibrational mode at 465 cm^{-1} of lattice oxygen was observed. Comparing 6G6NDC/6P6NDC to 6GDC/6PDC, the defect related modes at 570 and 600 cm^{-1} are less intense when Nb is present. This qualitative observation indicates that in presence of Nb, oxygen vacancies are annihilated.

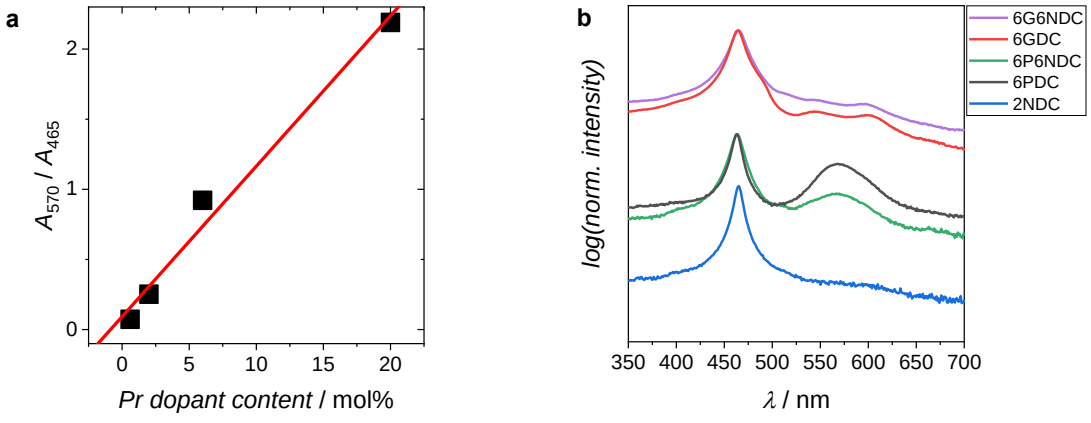

Figure 15: a) Correlation of the peak area ratio of the lattice oxygen and oxygen vacancy signal with the Pr dopant concentration. b) Comparison of the normalized Raman spectra of single Nb-, Gd-, and Pr-doped ceria with the Nb co-doped system.

To conclude, by Raman spectroscopy it was shown that the concentration of oxygen vacancies clearly correlate with the Pr/Gd dopant concentration. Nb–doped ceria did not show oxygen vacancy related modes and in GDC/PDC with additional

Nb–doping, the oxygen vacancy related modes are less intense indicating a decreased oxygen vacancy concentration.

4.1.2 UV-Vis Spectroscopy

Pure ceria shows three different absorption maxima in the UV region at about 255, 285, and 340 nm (3.6 – 5 eV) which correspond to Ce – O charge transfer processes and interband transitions[75, 76]. The measured spectra of doped ceria samples in the present study are all normalizes to the transition at 340 nm.

For Pr–doped ceria[70, 77] and zirconia[78], a broad absorption band at around 500 nm (2.5 eV) appears which is attributed to Pr^{3+} and creates the reddish color of PDC. It becomes more intense with increases Pr concentration (figure 16). Absorption measurements on Pr_2O_3[79] (only Pr^{3+}) showed three different transitions related to Pr^{3+} at around 450, 470 and 490 nm (2.5 – 2.8 eV). On Pr_6O_{11}[80] (the majority of Pr is in the 4+ state) a very broad feature between 400 and 1400 nm was observed which is attributed to O – Pr^{4+} charge transfer processes.

Figure 16: Color of GDC (which is similar for all Gd dopant content and pure ceria) and the series of PDC samples.

From figure 17a-c it can be seen that 20GDC and 6G6NDC show only Ce – O charge transfer processes and interband transitions as undoped ceria does. PDC samples as well as TDC show a broad band at around 500 nm (2.5 eV) which is attributed to Pr^{3+}/Tb^{3+}. With increasing Pr/Tb concentration, this absorption becomes more intense, which is in line with the color series of the samples (figure 16). At lower energies (<1.8 eV) and with increasing Pr/Tb concentration, the absorption increases again due to O – Pr^{4+}/Tb^{4+} charge transfer processes. This mode becomes more pronounced with increasing dopant concentration indicating the formation of an impurity band within the valance- and conduction band of ceria (see figure 18 for a scheme). The Pr^{4+} related transitions can also be noticed when one considers the absorption of a mixture of 80 % CeO_2 and 20 % Pr_6O_{11} in figure 17a. Pr/Nb co-doped ceria samples show also a broad band at around 500 nm which is attributed to Pr^{3+} transitions as can be seen from figure 17b.

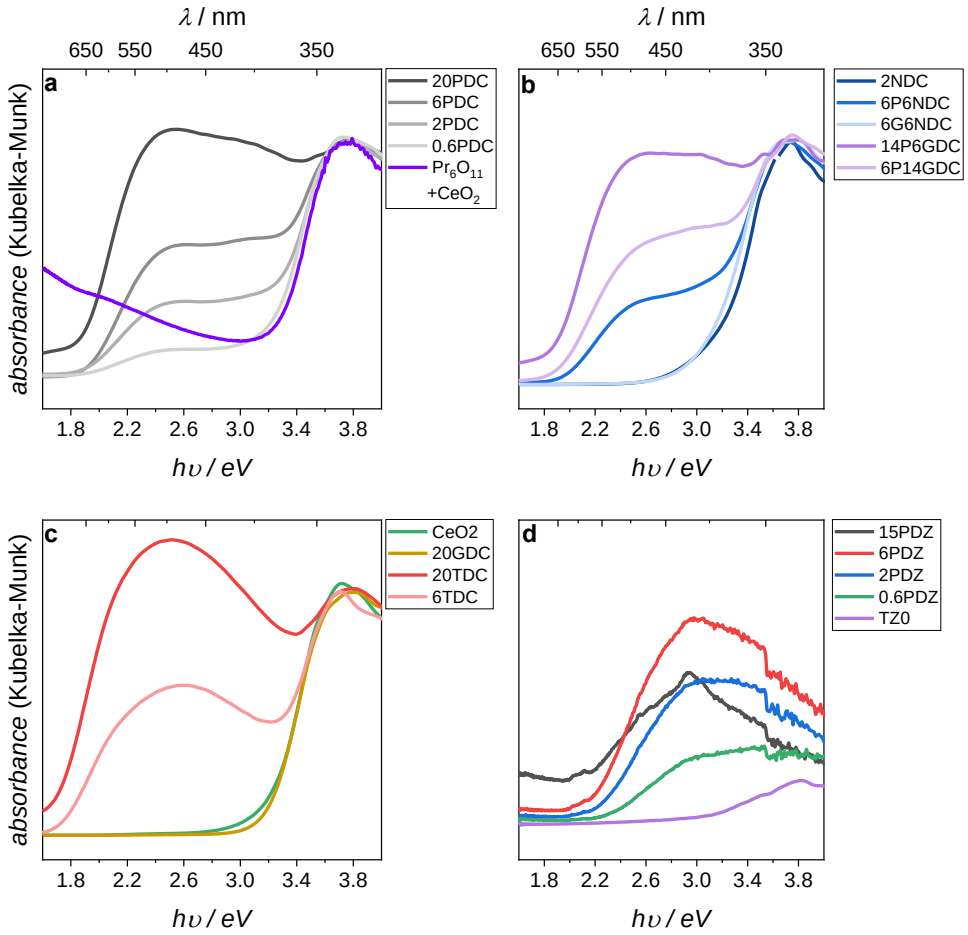

Figure 17: UV-Vis absorption spectra. a), b) and c) doped ceria samples, and c) Pr–doped and undoped zirconia (TZ0). Samples were diluted with 75 % TZ0 powder.

For Pr–doped zirconia (figure 17d), a broad adsorption band between 300 – 550 nm (2.2 to 4.1 eV) is present. At 590 – 600 nm (2 eV) a small peak can also be seen for 15PDZ in figure 17c which corresponds also to Pr^{3+} transitions[80]. The low intensity and the absence of this peak when PDZ with small Pr concentrations is considered may indicate that under the measurement conditions (and after the calcination in oxidizing conditions) no, or only a very small amount of Pr^{3+} is present. The increase of the absorption at λ > 600 nm (2 eV) is also attributed to O – Pr^{4+} charge transfer processes (as in PDC) and indicates the formation of a Pr impurity band within the valance- and conduction band of zirconia.

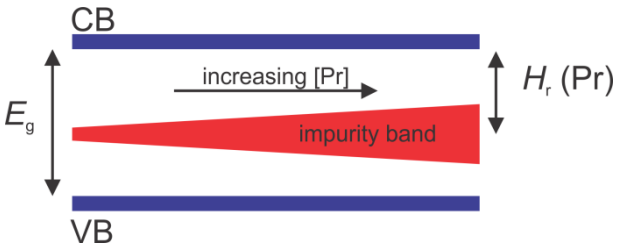

Figure 18: Scheme of the Pr-impurity band within the conduction band (CB) and valance band (VB) of ceria.

Due to the Franck–Condon principle, the retrieved energies of absorption are higher compared to results obtained by non-optical methods.

To conclude, evidence for the formation of a Pr–impurity band in Pr–doped ceria and zirconia was found. Terbium doped ceria behave similar to Pr–doped ceria. Co-doping with Nb seems not to influence the $Pr^{3+/4+}$ transitions. No formation of an impurity band was observed for single Nb and Gd–doped ceria.

4.1.3 Water Desorption

On the stoichiometric ceria (111) surface, it was found by DFT calculations that water adsorption proceeds on top of Ce^{4+} cations.[81, 82] Hydroxyl groups are stable up to 250 K[83] before they disappear. On reduced[81] as well as on Gd–doped ceria (XPS and electron stimulated desorption studies, *cf.* refs.[84, 85]) water adsorbs at room temperature at the oxygen vacancy site and water dissociation is thermodynamically more favorable. On reduced ceria (111), hydroxyl groups are stable to above 500 K.[83]

In figure 19, results from the present water desorption experiments conducted by TG measurements coupled with mass spectrometry on GDC and 2NDC calcined powder samples are shown (the BET surfaces are given in table 12, for water and CO_2 sorption experiments). The samples had been equilibrated with 21 mbar H_2O at 50 °C before desorption. One monolayer of adsorbed H_2O corresponds to an adsorbate concentration (θ) of 16 µmol m^{-2} by assuming an adsorption cross section of 10 $Å^2$ per H_2O molecule.[86]

Table 12: BET areas of the GDC and 2NDC calcined powder samples used for water and CO_2 desorption experiments.

Sample	BET / $m^2\ g^{-1}$
20GDC	10.4
6GDC	14.4
2GDC	13.2
0.6GDC	10.3
2NDC	6.2

A clear trend can be seen in figure 19: with increasing Gd and hence oxygen vacancy concentration the mass loss becomes larger (figure 19a). This indicates that more water adsorbs to the surface as more oxygen vacancies are present, which is in line with the above mentioned literature. At about 800 °C, the mass loss reaches a plateau where all water molecules are desorbed (also indicated by the mass spectrometer signal where no further release of H_2O was monitored).

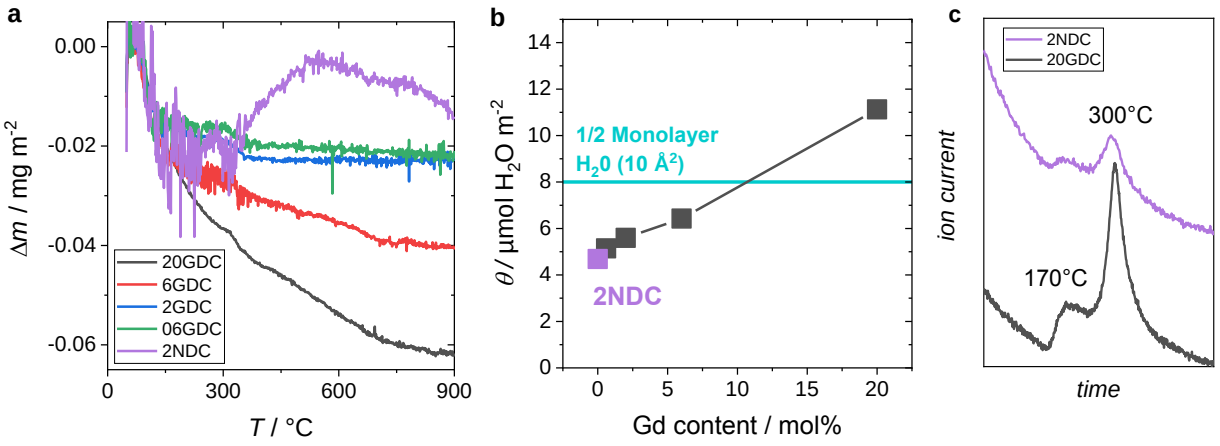

Figure 19: Water desorption experiments (21 mbar H_2O): a) Mass loss measured by TG as a function of sample temperature. b) Corresponding integrated water signal monitored by mass spectrometry. c) On-line mass spectrometer data which shows the water desorption for 20GDC and 2NDC. The data was shifted vertically for clarity.

For 2NDC, the mass loss from 50 °C to 150 °C is identical to the GDC samples, but decreases again at higher temperatures to the value at 50 °C. This might be related to the small weight changes and uncertainties in the buoyancy correction. Since the surface concentration of oxygen vacancies on 2NDC is minute, less water adsorption occurs when compared to the series of GDC samples. The integrated and calibrated water signal (using H_2O formation from 1.8 mg $CuSO_4$ $5xH_2O$ as reference) monitored by the MS also shows that less water desorbs from 2NDC compared to GDC (see also MS data in figure 19c).

It can be stated that the amount of adsorbed H_2O clearly correlates with [Gd] and hence with $[V_O^{\bullet\bullet}]$. While the absolute water amounts from TGA and MS differ, the trend with increasing Gd concentration is the same, strongly suggesting dissociative adsorption of water at oxygen vacancies.

4.1.4 Carbon Dioxide Desorption

Depending on the surface termination and presence of hydroxyl groups, *in situ* FT–IR spectroscopy on ceria powders showed that CO_2 adsorbs to ceria surfaces as monodentate, bidentate, polydentate and hydrogen carbonate species. The corresponding desorption temperatures were determined by TPD analysis to be 573, 573, 723 and 473 K, respectively.[87, 88] DFT calculations of ceria (110) surfaces indicated that CO_2 weakly physisorbed on stoichiometric ceria. On reduced ceria, the strongest adsorption energies were found when CO_2 adsorption proceeds atop an oxygen vacancy.[89] Yang *et al.* conducted experimental CO_2 sorption studies with undoped and Sm–doped ceria. They concluded that surface oxygen vacancies strongly affect the CO_2 adsorption.[90] Dopant dependent CO_2 adsorption

experiments have been performed in ref.[91]. They attributed the increase of the CO_2 adsorption capability in the series of Cu–CeO_2 > La-CeO_2 > Zr-CeO_2 = CeO_2 to the increased amount of oxygen vacancies.

The present CO_2 sorption experiments were conducted on GDC and 2NDC powder samples (BET areas in table 12) by two methods: thermogravimetry and pulsed CO_2 adsorption. In the first method, the samples had been equilibrated in 100 mbar CO_2 at 50 °C before desorption. One monolayer of adsorbed CO_2 corresponds to approximately 8 µmol m^{-2} by assuming an adsorption cross section of 20 $Å^2$ per CO_2 molecule.[92]

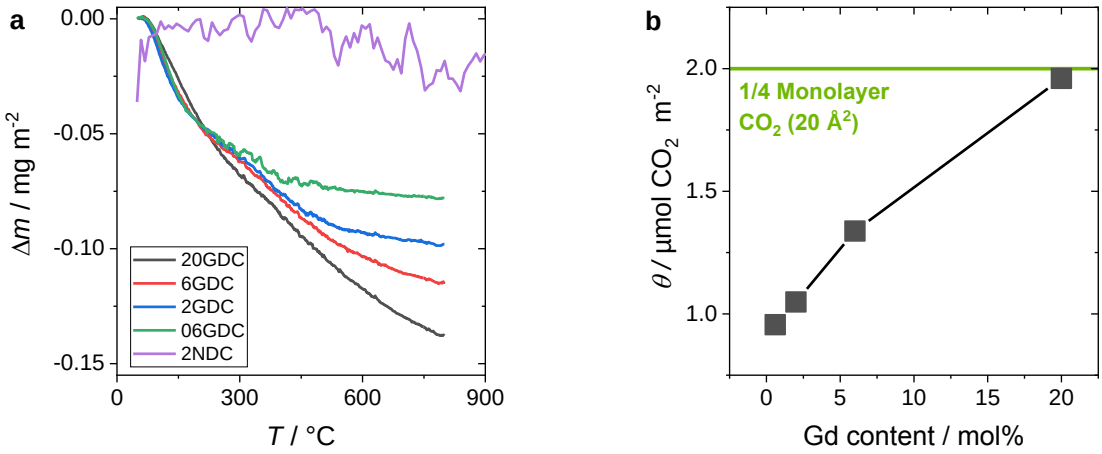

Figure 20: CO_2 desorption experiments (100 mbar CO_2): a) Mass loss measured by TG as a function of sample temperature. b) Corresponding integrated CO_2 signal monitored by mass spectrometry.

Results obtained by MS coupled TG are given in figure 20. 2NDC is inactive for CO_2 adsorption. The sample did not show a significant mass loss during CO_2 desorption, also no CO_2 was monitored by MS during desorption. GDC samples show a systematic trend: with increasing [Gd], the mass loss increases and the integrated CO_2 signal from the MS increases as well (using CO_2 formation from 3.6 mg $CaCO_3$ as reference). These results are in line with ref.[93], where the amount of adsorbed CO_2 increases with La concentration in La doped ceria. Furthermore, the measured CO_2 surface concentrating for 20GDC of about 1.9 µmol m^{-2} is comparable to literature data[93] of 1.6 µmol m^{-2}.

Temperature dependent pulsed carbon dioxide adsorption experiments on PDC, GDC and 2NDC calcined powder samples also showed a clear relationship between dopant content and CO_2 adsorption capability (figure 21).

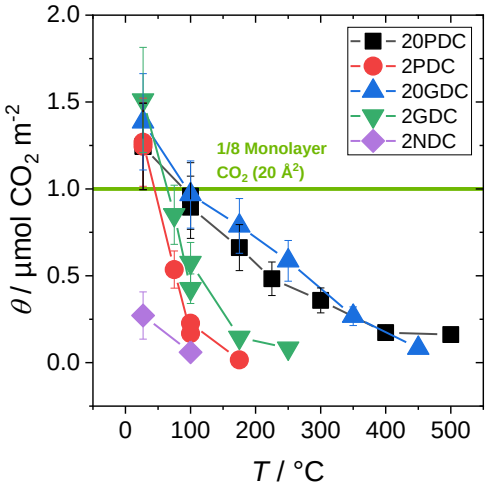

Figure 21: CO_2 adsorption for PDC, GDC and 2NDC, measured by pulsed carbon dioxide adsorption experiments, the pulse contained 0.5 mL of 1 % O_2 and 1 % CO_2.

While for 20 and 2 PDC/GDC samples the surface concentration of CO_2 amounts to 1.2 – 1.5 µmol m^{-2}, the concentration of adsorbed CO_2 for 2NDC is low with 0.2 µmol m^{-2} at room temperature. These values are in good agreement to the present CO_2 desorption experiment by TG/MS and to data of Wilkes *et al.* (for 20PDC 1.5 µmol m^{-2})[93]. With increasing temperature, less CO_2 tends to adsorb to the surface. At 100 °C, almost no CO_2 adsorbs to the 2NDC surface. For 2PDC and 2GDC, the surface concentration of CO_2 is minimal already at about 200 – 250 °C while for 20GDC and 20PDC CO_2 adsorption ceases only at 450 °C to about 0.2 µmol m^{-2}.

Specific cation effects cannot be excluded; however, it is highly plausible that the amount of adsorbed CO_2 correlates with $[V_O^{\bullet\bullet}]$ hand hence, with the dopant type and concentration. PDC and GDC tend to adsorb identical adsorbate concentrations while CO_2 adsorption is not favorable on 2NDC.

4.1.5 Thermogravimetry

Thermogravimetric measurements were conducted in order to investigate the oxygen non-stoichiometry of Pr–doped ceria and how strong PDC got reduced under the experimental conditions in the further approach. Results, regarding the chemical oxygen surface exchange coefficient k^{δ} obtained from mass relaxation are given in section 4.2.3.3, where the measured exchange coefficients from different methods are compared. The results of *in situ* CO and CH_4 oxidation are given in chapter 4.3.

The oxygen non-stoichiometry (2-δ) is plotted for 20, 6, and 2PDC in figure 22. At low temperatures all Pr is assumed to be tetravalent and δ was set to zero. With increasing temperature and decreasing oxygen partial pressure, Pr^{4+} reduces to Pr^{3+}

which induces the increase of the oxygen vacancy concentration and hence, a stronger negative deviation from the ideal oxygen stoichiometry. At $T > 800$ °C, (2-δ) reaches a plateau where all Pr is trivalent and the condition $[Pr]_{tot} \approx 2[V_O^{\bullet\bullet}]$ holds.

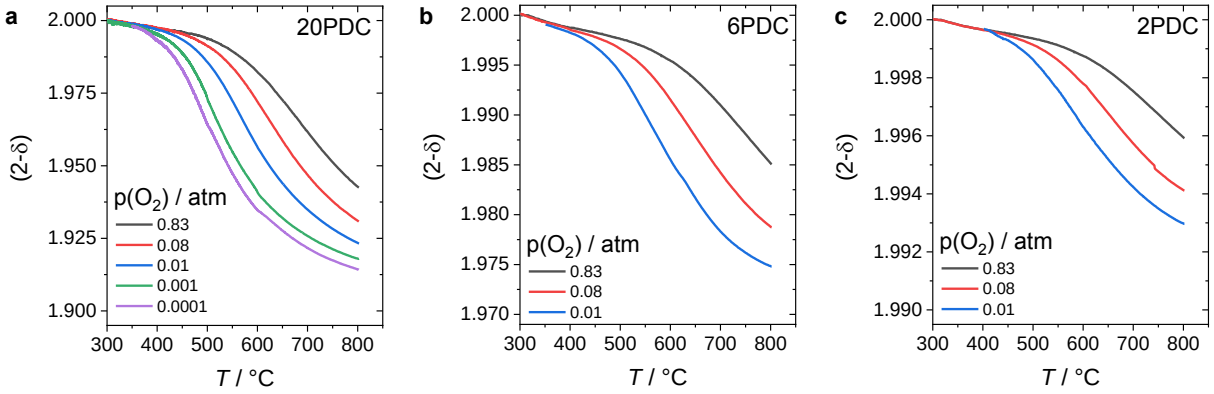

Figure 22: Oxygen non-stoichiometry at different oxygen partial pressures as a function of temperature for a) 20PDC, b) 6PDC and c) 2PDC.

The thermodynamic factor w was extracted according to eq. 44 (*cf.* ref.[94], page 268) from the oxygen non-stoichiometry data and the results are given in figure 23. Generally, w describes how strongly the oxygen ion concentration in the material changes on the oxygen partial pressure. With increasing Pr concentration and decreasing temperature, w decreases as expected since the thermodynamic factor is inversely related to the chemical capacity ($C_{chem} = \frac{\partial[O_O^x]}{\partial \mu_O}$)

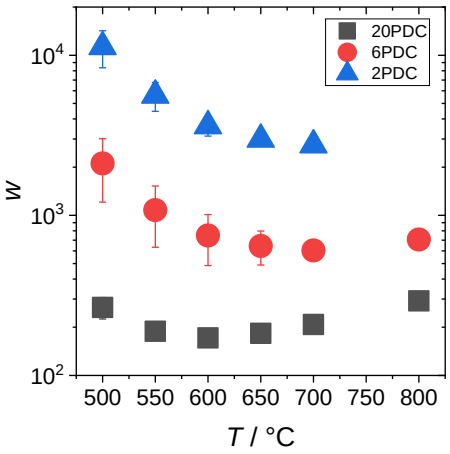

$$w = \frac{1}{2}\frac{\partial ln(p(O_2)\ bar^{-1})}{\partial ln(2-\delta)} \qquad \text{eq. 44}$$

Figure 23: Extracted thermodynamic factor *w* for 20, 6, and 2PDC at different temperatures.

From the mass change in figure 22, the fraction of Pr^{3+} can be extracted by assuming r. 2, and eq. 45 can be derived (ideal behavior assumed), where x_{Pr} and x_{O_2} denote the fraction of Pr in the doped ceria samples and the fraction of oxygen in the gas phase. $\Delta H^{\circ}_{r,Pr}$ is the enthalpy of reduction for Pr and $\Delta S^{\circ}_{r,Pr}$ the corresponding entropy which are given in table 13.

$$K = \frac{[O_O^x][Pr_{Ce}^x]^2}{\sqrt{p(O_2)}[V_O^{\bullet\bullet}][Pr_{Ce}']^2} \Rightarrow \frac{(2-\delta)(x_{Pr}-2\delta)}{\sqrt{x_{O_2}}4\delta^3} = K_{r,Pr}\exp\left(\frac{-\Delta H_{r,Pr}^\circ + T\Delta S_{r,Pr}^\circ}{RT}\right) \qquad \text{eq. 45}$$

Table 13: Calculated thermodynamic data for Pr doped ceria samples.

Sample	$\Delta H_{r,Pr}^\circ$ / eV	$\Delta S_{r,Pr}^\circ$ / J mol^{-1}K^{-1}
20PDC	2.3 eV	-200
6PDC	1.9 eV	-130
2PDC	1.8 eV	-95

The fraction of Pr^{3+} as a function of temperature at different $p(O_2)$ was already discussed and shown in section 2.1.2.

Overall, TG measurements showed that the oxygen non-stoichiometry and Pr^{3+}/Pr^{4+} ratio is strongly affected by the oxygen partial pressure and temperature.

4.1.6 Oxygen Ion Diffusion

Oxygen ion diffusion was measured by isothermal isotope exchange line profiling (IELP) on dense 20PDC and 20GDC pellets in 200 mbar O_2 from 500 °C to 650 °C. The extracted tracer diffusion coefficients D^* for 20GDC and 20PDC are given in figure 24. The tracer oxygen surface exchange rates k^* are given in section 4.2.3.3 where they are compared to other exchange rates determined by different methods.

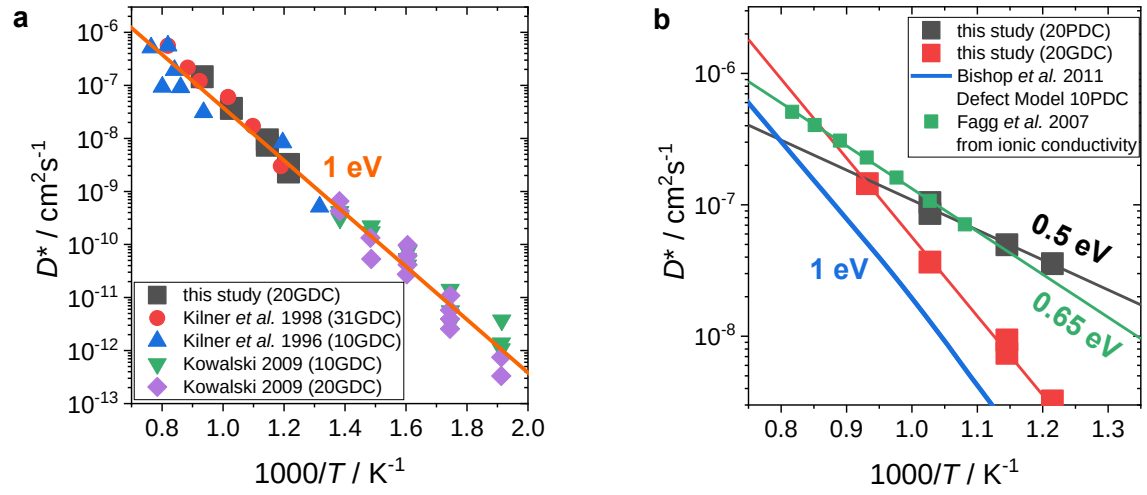

Figure 24: Tracer diffusion coefficients D^* for a) GDC and b) PDC. Literature values were extracted from refs.[95-97] for GDC, and from refs.[15, 98] for PDC.

As can be seen from figure 24a, D^* for the present 20GDC sample matches very well to literature data for 31GDC, 20GDC, and 10GDC measured also by IELP[95-97], demonstrating the reliability of the present measurement method. The oxygen diffusion shows an apparent activation energy of around 1 eV.

In figure 24b, D^* for the present 20PDC is plotted together with data extracted from ionic conductivities (oxygen) and mobilities (oxygen vacancy)[15, 98]. No IELP measurements have previously been performed on Pr-doped ceria samples. Ionic

conductivity and mobility data was converted to D^* by using eq. 46 and eq. 47 where D_V denotes the oxygen vacancy diffusion coefficient, u_V is the mobility of oxygen vacancies, $\mathcal{F}_V$ is the tracer correlation factor (for simple cubic structure with very low defect concentration $\mathcal{F}_V \approx 0.65$[99]), σ_{ion} is the oxygen ionic conductivity, z and F are the charge and the Faraday constant, respectively.

$$D^* = \frac{\delta}{2-\delta} D_V \mathcal{F}_V = \frac{\delta}{2-\delta} \frac{u_V RT}{zF} \mathcal{F}_V \qquad \text{eq. 46}$$

$$D^* = \frac{RT\sigma_{ion}}{[O_O^x] z^2 F^2} \qquad \text{eq. 47}$$

The present 20PDC sample shows higher tracer diffusion coefficients compared to 20GDC, and a significantly decreased activation energy with a value of 0.5 eV. On the other hand, for D^*, calculated from literature oxygen vacancy mobilities (blue line, figure 24b), the activation energy amounts 1 eV, which is identical to GDC. The reason for this might be that u_V was determined at T and $p(O_2)$ where all Pr is trivalent and no Pr^{3+}/Pr^{4+} redox-couple is available. Therefore, it is not too surprising that this data matches better to GDC (since in GDC only Gd^{3+} is present). In contrast, D^* from oxygen ion conductivities (green data in figure 24b, at T and $p(O_2)$ where still an perceptible amount of Pr^{3+}/Pr^{4+} is present) are in very good agreement to D^* of the present 20PDC, indicating that the Pr redox-couple facilitates the oxygen ion diffusion. A tentative explanation for this behavior could be the formation of a percolating oxygen path with decreased migration barriers along $Pr^{3+/4+}$.

4.2 Oxygen Exchange Kinetics

This section deals with the results regarding the oxygen exchange kinetics. Parts of this chapter already have been published by the author as part of this dissertation (*cf.* ref.[100]). First, general sample characteristics are presented followed by a detailed discussion and interpretation of the results.

4.2.1 Sample characteristics

For probing the oxygen exchange kinetics on doped ceria systems, double–annealed particles were used, which showed a BET surface of 0.014 m^2g^{-1}. The double annealing at 1400 °C yields well defined and almost pore free surfaces of the particles as depicted by the SEM images in figure 25.

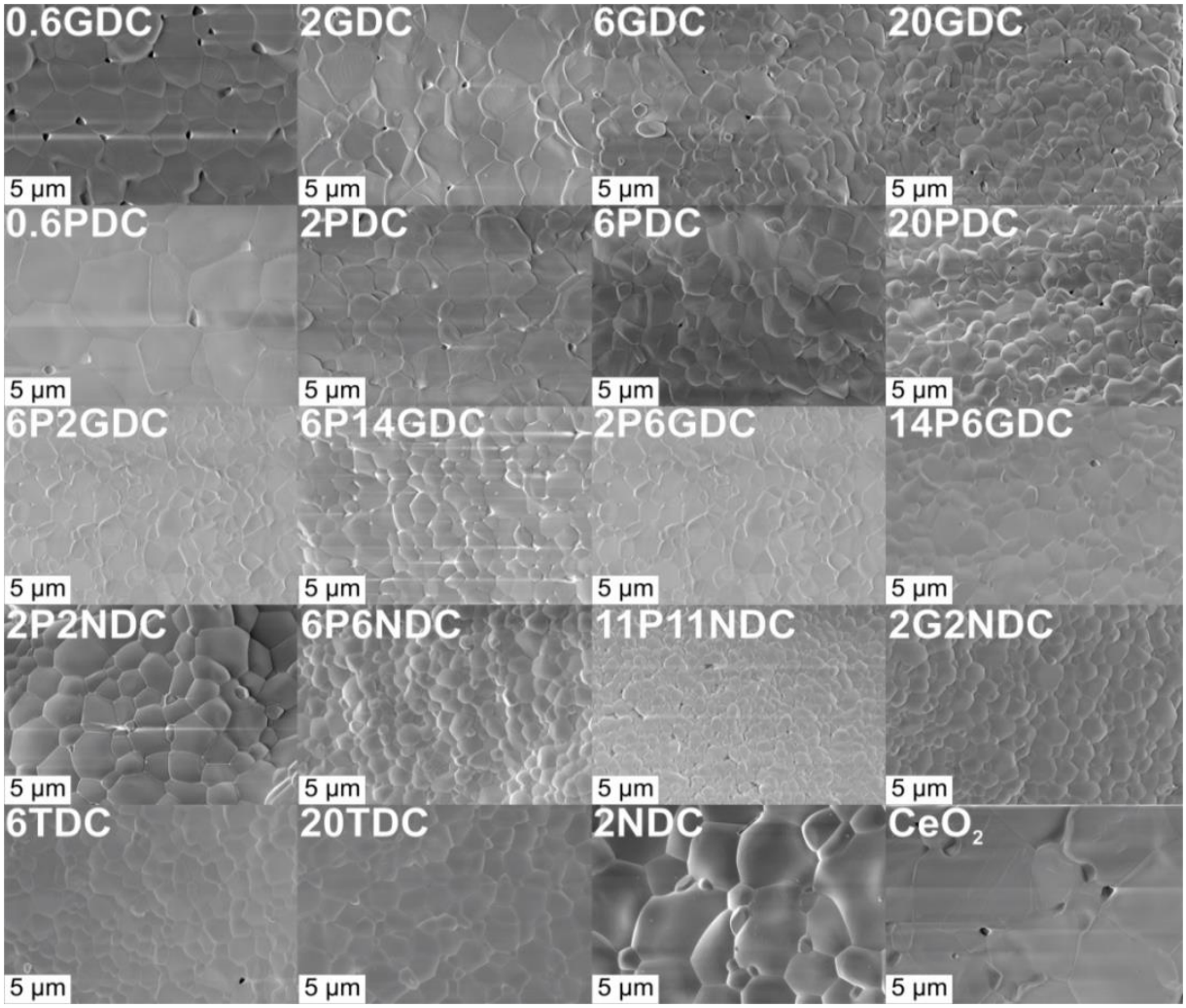

Figure 25: SEM images of the surfaces of the double–annealed (1400 °C) particles of doped ceria investigated by pulsed oxygen isotope exchange.

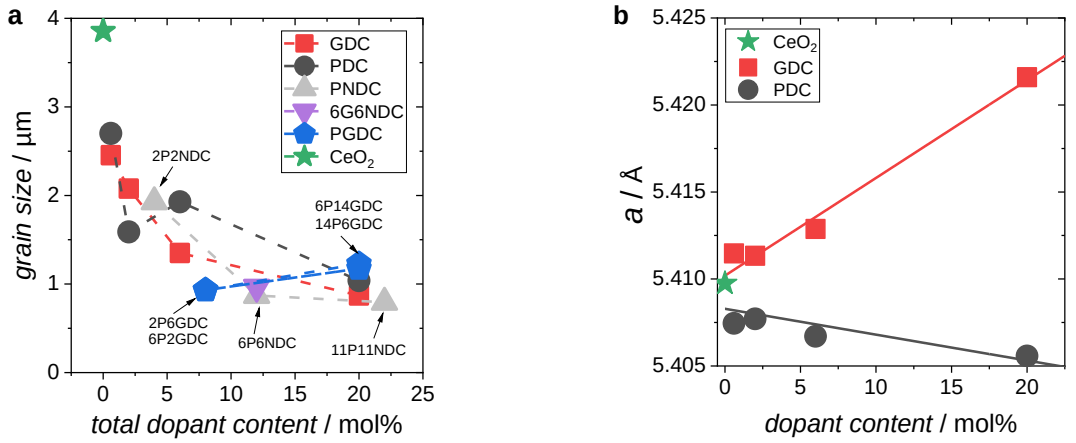

Figure 26: a) Grain size of doped ceria samples as a function of total dopant content. b) Lattice parameter of PDC and GDC as a function of dopant content.

The mean grain size ranges from 1 – 4 µm and tends to decrease moderately with increasing doping content (figure 26a). This trend was also found, for example in ref.[101], where the mean grain size of GDC pellets decreases from 7.2 µm (1 mol% Gd) to 1 µm (20 mol% Gd). XRD measurements (figure 27 to figure 29) confirmed a phase pure, cubic fluorite type crystal lattice. Only 11P11NDC shows a small impurity of a second phase.

The lattice parameters for Gd–doped ceria follow Vegard's law[102] (figure 26b) indicating a solid solution, corresponding to the larger ion radius of Gd^{3+} (Ce^{4+} 0.97 Å, Gd^{3+} 1.053 Å[103]). The lattice constants of the Pr-doped ceria system decrease slightly. This indicates that the mean valance of Pr shifts to 4+ rather than 3+ (Pr^{4+} 0.96 Å, Pr^{3+} 1.126 Å), which is in accordance with the defect model calculations[14] and TG data (figure 2 and figure 3). A summary of the lattice parameter for the investigated doped ceria samples is listed in table 14.

Table 14: Lattice parameter of undoped ceria, PDC, GDC, Pr/Gd co–doped ceria, 2NDC, Pr/Nb, Gd/Nb, and Pr/Gd co–doped ceria.

Sample	Lattice Parameter *a* / Å	Sample	Lattice Parameter *a* / Å
CeO_2	5.4098	20TDC	5.3910
06GDC	5.4115	2P6GDC	5.4126
2GDC	5.4113	6P2GDC	5.4081
6GDC	5.4129	6P14GDC	5.4179
20GDC	5.4216	14P6GDC	5.4142
06PDC	5.4075	11P11NDC	5.4142
2PDC	5.4077	6P6NDC	5.4092
6PDC	5.4067	2P2NDC	5.4091
20PDC	5.4056	6G6NDC	5.4048
6TDC	5.4066	2NDC	5.4080

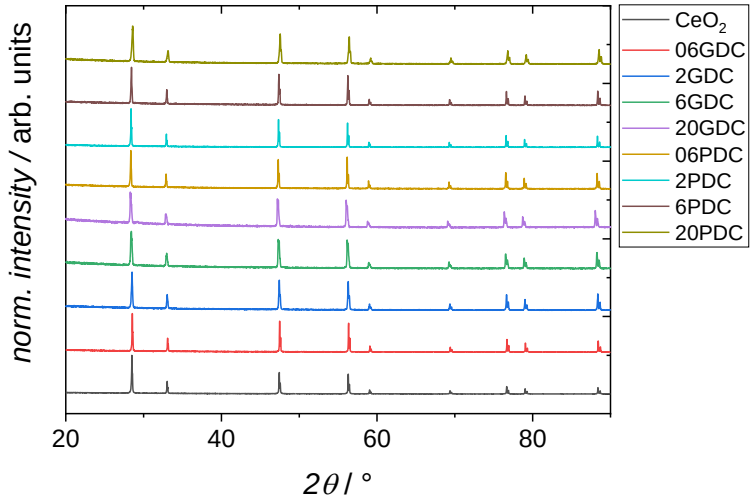

Figure 27: XRD patterns for undoped ceria, GDC, and PDC.

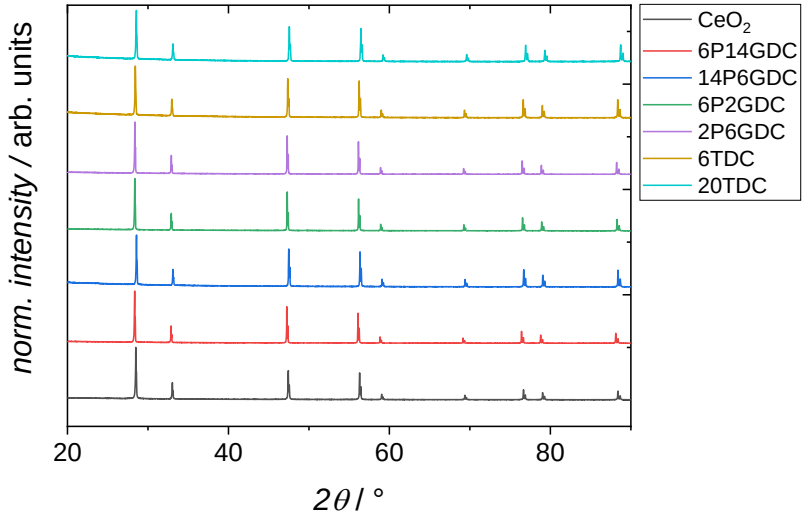

Figure 28: XRD patterns for undoped ceria, Tb-doped ceria, and Pr/Gd co–doped ceria.

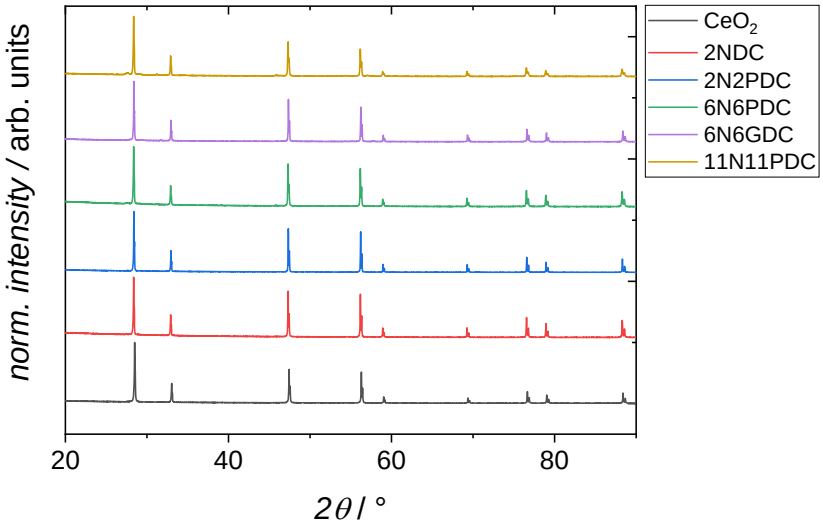

Figure 29: XRD patterns for undoped ceria, 2NDC and equimolar Pr/Nb, Gd/Nb co–doped ceria.

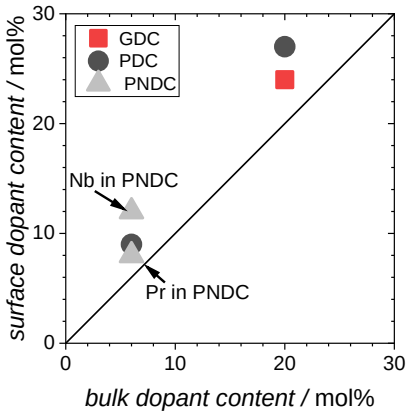

Figure 30: Dopant content at the surface of the twofold annealed particles determined by XPS.

XPS measurements conducted on 20PDC, 6PDC, 20GDC, 6GDC and 6P6NDC (figure 30) revealed a moderate segregation of dopants to the surface of the particles of up to 30 % relative to bulk values after the second annealing step at 1400 °C. The tendency of the dopants to segregate increases according to Gd < Pr < Nb.

By TEM–EDX elemental analysis on 6PDC (Figure 31a-b) it was found that the concentration of Pr across a grain boundary is moderately increased in comparison to the bulk. It is important to note that no significant amount of Si was found. Due to the segregation of dopants around the grain boundary, the grain boundary growth is now impeded by the lattice diffusion of these dopants (see figure 26a). This effect is called solute drag and was investigated, *e.g.*, in ref.[104] for doped ceria.

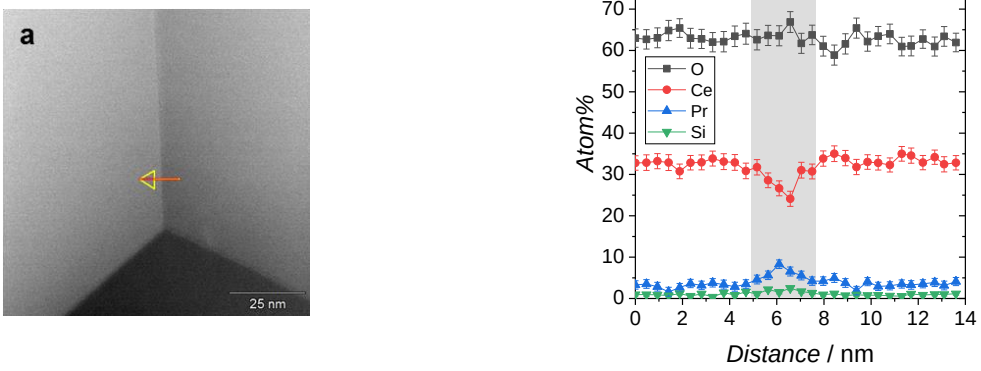

Figure 31: a) Location and direction of the performed line scan at a grain boundary of 6PDC. b) Atom% profile of Pr, Ce, Si and O along the line scan.

For all doped ceria samples, the particles probed by PIE measurements are in the surface controlled regime. The characteristic lengths ($l_0 = k^*/D^*$ (D^* = oxygen tracer diffusion coefficient, k^* = effective tracer exchange rate constant) calculated with literature data[95, 105, 106] are typically 10 – 1000 times larger than the average particle radii of the samples. Hence, bulk diffusion of oxygen is fast compared to the surface reaction, and not affecting the ^{18}O exchange kinetics.

Oxygen ion blocking effects at grain boundaries in acceptor doped ceria are known to be present, but in the temperature regime where oxygen exchange is conducted, the blocking effect becomes small[107, 108]. Impedance spectroscopy of GDC pellets confirmed this observation. In figure 32 the conductivity of 6GDC and 20GDC is plotted.

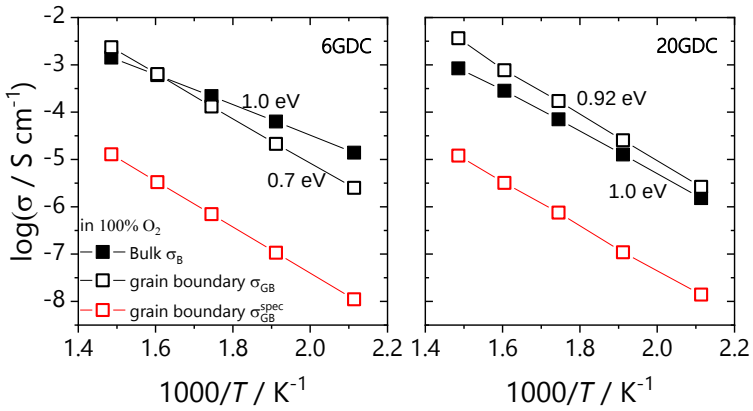

Figure 32: Conductivity of 6GDC and 20GDC pellets as a function of inverse temperature obtained by electrochemical impedance spectroscopy in 100 % O_2.

The activation energies for grain boundary and bulk conductions remain close to each other, as observed in literature (see, *e.g.*, ref.[109]). Due to the slightly blocking character of the grain boundaries, the specific grain boundary conductivity (σ_{GB}^{spec}, see section 3.2.7) is below the bulk conductivity (σ_B). However, the total conductivities of bulk and grain boundaries are very close together indicating almost non–blocking grain boundaries, especially at higher temperatures.

4.2.2 Raw Data and Exchange Activity of the Empty Reactor

In figure 33 the ion currents of the oxygen isotopologues $^{32}O_2$, $^{34}O_2$, and $^{36}O_2$ at the exit of the reactor are shown. During pulsing, the mass balance (green line in figure 33) of the isotopologues deviates only slightly, confirming the reliability of the quantitative analysis.

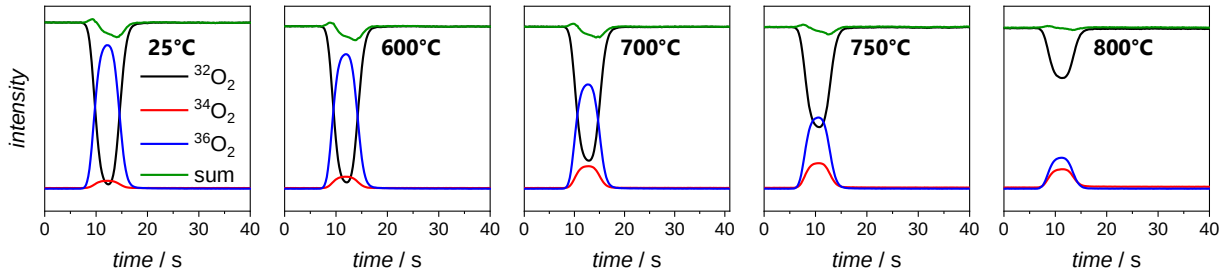

Figure 33: Raw data of a PIE experiment conducted on 20GDC. Depicted are the ion currents for the three oxygen isotopologues as a function of time. The green line denotes the mass balance of oxygen.

The sum of the peak areas remains almost constant (deviation of ± 0.5 %) when normalized to the reference ^{15}N peak (not shown in figure 33) in a temperature

series. This also indicates that the ionization probability of the oxygen isotopologues is similar. The relative uncertainties for the three oxygen isotopologues fractions range between $\pm 2-6$ % and are higher for $^{32}O_2$ and $^{34}O_2$, especially at high conversions (high temperatures), and with samples with a profound formation of $^{34}O_2$ due to the overlap of incorporation/excorporation.

In figure 34, the fractions of the oxygen isotopologues $^{32}O_2$, $^{34}O_2$, and $^{36}O_2$ in the pulse are plotted as a function of reactor temperature for an empty quartz glass and Al_2O_3 reactor (both are filled with approx. 15 mg SiO_2 wool, which later serves as catalyst support). Both reactors show oxygen exchange activity mainly due to isotopic scrambling at the reactor surface. The total ^{18}O content hardly changes, hence the ^{18}O exchange with the reactor and the Si wool is negligible. In case of the quartz glass reactor, isotopic scrambling commences already between 700 – 800 °C.

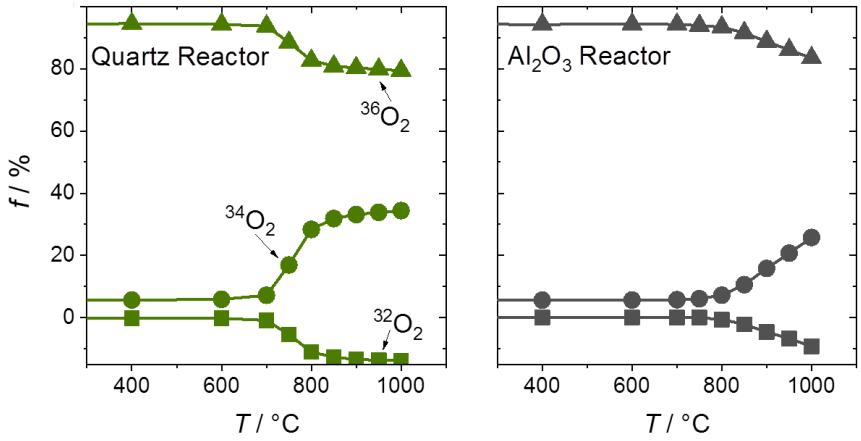

Figure 34: Oxygen isotopologue fractions (*f*) measured at the exit of the reactor as a function of reactor temperature. Shown are the data for an empty quartz and Al_2O_3 reactor with approx. 15 mg SiO_2 wool as catalyst chair and an inner diameter of 2 mm in 10 % O_2.

The negative $^{32}O_2$ fractions are due to some unavoidable smearing of the ^{18}O pulse: at the edges of the pulse, residual $^{32}O_2$ can scramble at the reactor surface with $^{36}O_2$ yielding $^{34}O_2$, as indicated by peak splitting of the $^{34}O_2$ MS signal. Al_2O_3 shows considerable oxygen exchange activity only at temperatures beyond 850 – 900 °C, which makes this material an appropriate reactor for PIE measurements.

4.2.3 Pulsed Isotope Exchange of Doped Ceria

Figure 35 summarizes the fractions of the oxygen isotopologues in the pulse for selected doped ceria samples. Generally, with increasing temperature, ^{18}O starts to incorporate into the sample indicated by a decrease of ^{36}f. Due to the fact that the oxygen stoichiometry is in chemical equilibrium, the same amount of ^{16}O needs to be released from the sample in the form of $^{32}O_2$ or $^{34}O_2$ depending on the underlying reaction mechanism.

2NDC and undoped ceria show similar low oxygen exchange activity as the empty Al_2O_3 reactor. The measured Gd, Pr and Tb single– and co–doped samples are all more active for oxygen exchange compared to undoped CeO_2. On 0.6GDC oxygen incorporation commences at around 750 °C. This onset temperature decreases with increasing Gd concentration so that for 20GDC oxygen incorporation starts already at 600 °C. All Gd–doped ceria samples show a moderate formation of $^{34}O_2$ which points to a slow incorporation rate relative to the rates of oxygen adsorption and dissociation. The oxygen exchange activity on Pr–doped ceria samples increases even more pronounced than on GDC. For 0.6PDC, oxygen incorporation starts in the same low temperature range as for undoped ceria or the empty reactor (850 – 900 °C).

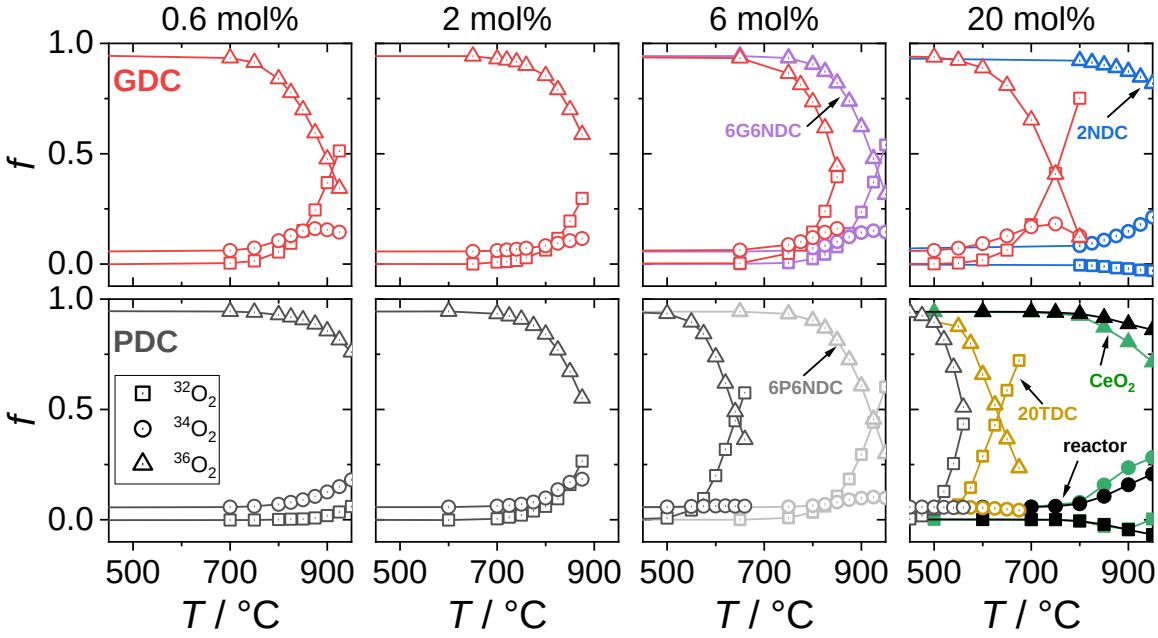

Figure 35: Oxygen isotopologue fractions (*f*) measured at the exit of the reactor as a function of reactor temperature in 10 % O_2 atmosphere.

With increasing [Pr] the onset temperature for oxygen incorporation shifts quickly to lower temperatures, reaching a value of already 500 °C for 20PDC. The absence of $^{34}O_2$ for samples with less than 6 mol% Pr or Tb suggests that the dissociated oxygen species incorporates faster into the bulk when compared to GDC or Nb single– and co–doped ceria, or that the oxygen diffusivity in bulk PDC/TDC is faster than in GDC. According to the defect chemical model[14], 10PDC has a moderately higher $V_O^{\bullet\bullet}$ mobility than single crystalline 10GDC (measured by ^{18}O isotope exchange and SIMS line scan)[96], which is in agreement with molecular dynamics simulations[110]. The present isothermal isotope exchange line profiling (IELP) experiments of 20GDC and 20PDC dense pellets (see section 4.1.6) indeed showed a higher oxygen diffusion coefficient for 20PDC. The activation energy for

oxygen diffusion of 20PDC of 0.5 eV is half of the value for 20GDC with 1 eV. A tentative explanation for this behavior could be the formation of a percolation oxygen path with decreased migration barriers along $Pr^{3+/4+}$.

Pr/Nb, Gd/Nb, and 2NDC are less active for oxygen incorporation compared to GDC and PDC or Pr/Gd co–doped samples and the formation of $^{34}O_2$ is less pronounced for PNDC than for GNDC (figure 34). Since donor–doping with Nb leads to a suppression of oxygen vacancies (or even leads to the formation of oxygen interstitials for 2NDC), these results show that oxygen vacancies are crucial for the oxygen incorporation reaction.

In the following, first the ^{18}O gas phase fraction will be analyzed by assuming the overall oxygen incorporation reaction (eq. 18), followed by an analysis of the $^{32}O_2$, $^{34}O_2$, and $^{36}O_2$ gas phase fractions in terms of the reaction mechanisms M1 and M2 (eq. 25 and eq. 26) mentioned in section 2.3.2.

4.2.3.1 Analysis of the ^{18}O gas phase fraction

The calculated equilibrium exchange rates $\Re_0$ of the overall oxygen incorporation reaction (r. 6, and eq. 18) are plotted in figure 36, the temperature dependence of all doped ceria samples follows Arrhenius behavior.

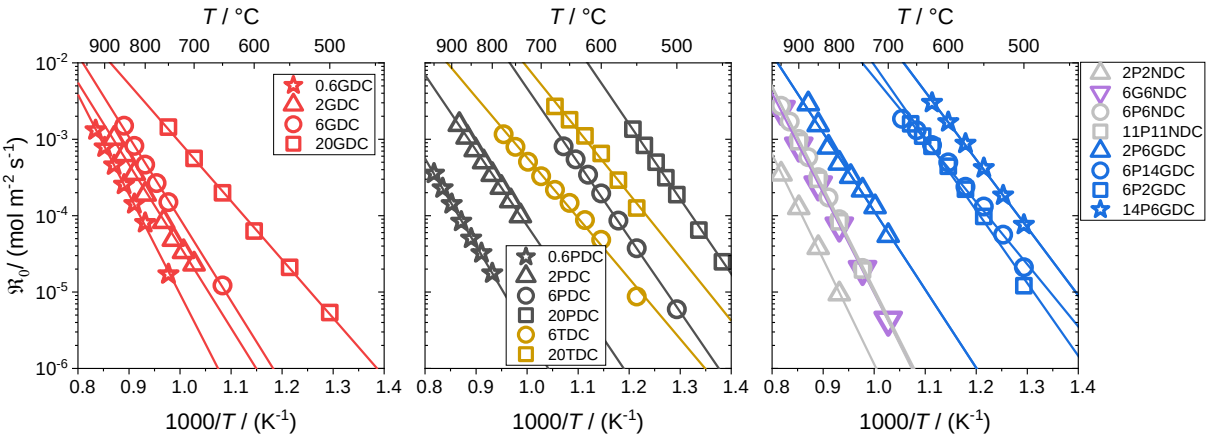

Figure 36: Arrhenius diagram of the equilibrium exchange rate $\Re_0$ for doped ceria sample measured in 10 % oxygen atmosphere.

$\Re_0$ from subsequent pulses varied by a factor of 0.3 – 1.7 relative to the mean value at low oxygen conversions, but with increasing conversion this deviation increases. Thus, the relative errors are small relative to the variation of $\Re_0$ with T or dopant concentration. The repetition of a T–series for 20PDC did not show any indications of sample degradation. Figure 37 shows the extracted activation energies (E_a) ranging between 1.4 – 2.3 eV as a function of the total dopant content. The relative error for E_a was found to be ±5 %.

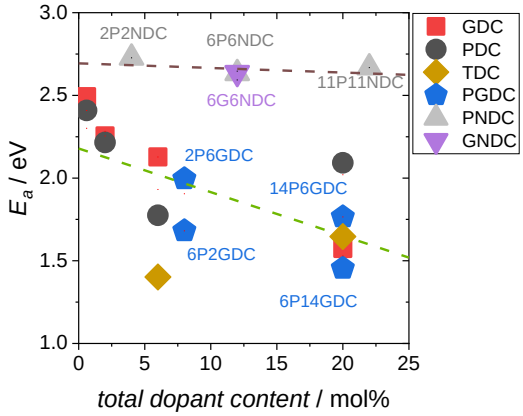

Figure 37: Extracted activation energies of $\Re_0$ in 10 % O_2 for doped ceria samples.

Two distinct groups can be seen in figure 37: Pr, Tb, and Gd single– and co–doped ceria samples showed E_a values ranging from 1.4 –2.3 eV, while Nb doping led to higher activation energies between 2.5 – 2.8 eV. With increasing total dopant content the values tend to decrease slightly. The interpretation of the obtained E_a values are not straightforward since they represent a combination of the actual reaction barrier of the *rds* and the reaction/adsorption enthalpies of fast preceding steps. However, the higher E_a values for Nb doped ceria might arise from higher reaction barriers due to the absence of oxygen vacancies, or from higher effective temperature dependence of the tiny oxygen vacancy concentration compared to PDC, TDC and GDC.

To relate the trends of the oxygen exchange rates with the dopant concentration, $\Re_0$ was inter/extrapolated to a common temperature of 700 °C. Therefore, the values of the slopes in figure 38 may carry some uncertainty. Nevertheless, due to the large change of dopant content by 1.5 order of magnitude, the observed trends are reliable. Since undoped ceria and 2NDC show low oxygen exchange activity in the range of the empty Al_2O_3 reactor, only an upper limit of $\Re_0$ is given for them.

For GDC, figure 38a shows that $\Re_0$ is proportional to the Gd bulk concentration. Relative to undoped ceria, $\Re_0$ increases by two orders of magnitude. Since the condition $[\mathrm{Gd}] = 2[V_O^{\bullet\bullet}]$ holds, $\Re_0$ is proportional to the bulk $[V_O^{\bullet\bullet}]$ according to $\Re_0 \propto [V_O^{\bullet\bullet}]^1$. On has to keep in mind that the absolute surface concentration of oxygen vacancies differ from the bulk values, but still an approximate proportionality to the bulk Gd concentration is expected (*cf.* sections 2.1.3 and 2.2.2). In contrast, for Pr doped ceria samples, $\Re_0$ increases more strongly according to $\Re_0 \propto [V_O^{\bullet\bullet}]^{3.5}$ (see figure 38b). Overall, for 20PDC the $\Re_0$ value increases by almost five orders of magnitude (by a factor of 100000) relative to undoped ceria.

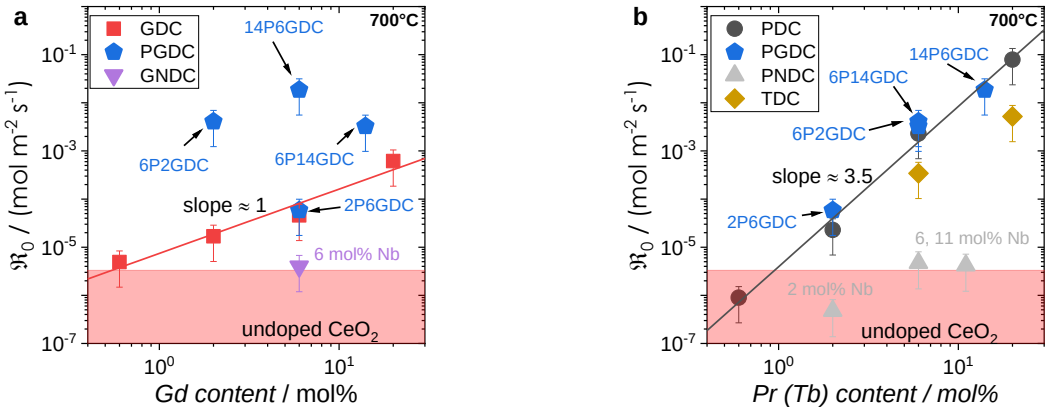

Figure 38: $\Re_0$ as a function of bulk (a) Gd and (b) Pr content. The red shaded area indicates the activity range of undoped ceria and 2NDC. Values for 06GDC, 20GDC, 06PDC, 2PDC, 6PDC and 20PDC are mean values calculated from at least two measurement series (separately filled reactor beds).

Such a strong increase suggests that the intrinsic redox activity of Pr itself also affects the oxygen exchange activity. In the present study, TDC shows similar strong correlation of $\Re_0$ with [Tb], and agrees well with results from Balaguer *et al.*[61], where a relationship of $[Tb] \propto \Re_0^{2.1}$ was found (10, 20 and 50 mol% Tb doped ceria). This indicates that redox–active dopants tend to facilitate the oxygen incorporation, which is in line with several observations that mixed conducting fluorites or perovskites activate the oxygen incorporation more strongly than purely electronic or ionic conductors[55, 111-116].

Gd and Pr co–doped ceria behave similar to PDC. Mainly the [Pr] seems to determine the oxygen exchange activity: while additional Gd co–doping (figure 38b) shows almost no effect on the equilibrium exchange rate, additional Pr co–doping clearly increases $\Re_0$ (figure 38a). As soon as an equimolar concentration of Nb is present in Nb/Pr, Nb/Gd co–doped ceria the $\Re_0$ values drop down to the region of undoped ceria, which strongly supports the assumption that the increase of the reaction rate with increasing Gd concentration is related to the concentration of oxygen vacancies and not to some specific effect of the Gd cations.

Important information about the underlying reaction mechanism can be obtained when the oxygen partial pressure dependence of $\Re_0$ is considered (figure 39). For the present samples, the oxygen partial pressure exponent n is always above 0.5 and ranges between 0.6 – 0.8. As discussed in section 2.3.2, this means that molecular oxygen is involved in the *rds* of oxygen incorporation. The fact that n is smaller than 1 indicates that other point defects also play a role in the reaction mechanism.

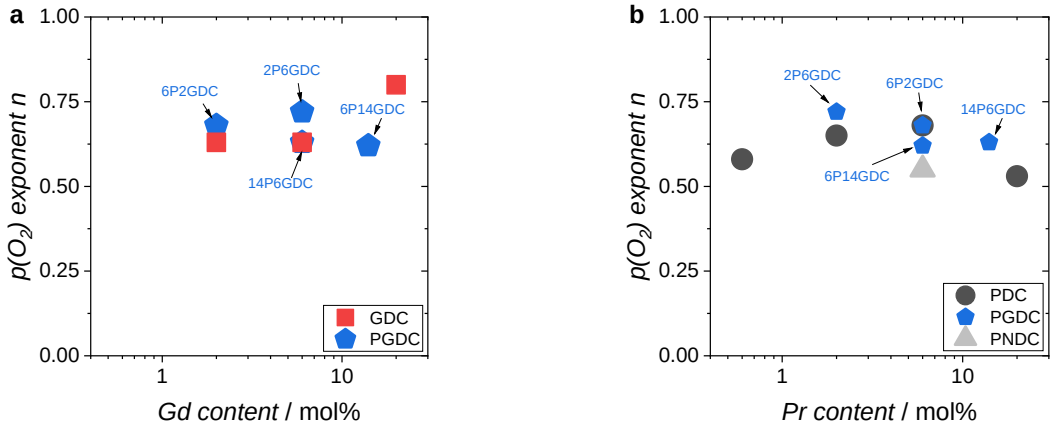

Figure 39: Oxygen partial pressure exponents *n* as a function of dopant content. The relative error is smaller than the symbol size. Temperatures where *n* was determined: 2GDC 810 °C, 6GDC 785 °C, 20GDC 625° C, 2PDC 800 °C, 6PDC 650 °C, 20PDC 560 °C, 2P6GDC 775 °C, 6P2GDC, 6P14GDC 600 °C, 14P6GDC 575 °C, 2P2NDC 850 °C.

Assuming a fast pre–equilibrium of oxygen adsorption where just one hole is involved (r. 11, eq. 48), followed by the vacancy–assisted dissociative–incorporation of the adsorbed oxygen molecule O_2^- as the *rds* (r. 12, eq. 49) yields:

$$O_2 \underset{\overleftarrow{k}_1}{\overset{\vec{k}_1}{\rightleftharpoons}} O_2^- + h^\bullet \qquad \text{r. 11} \qquad K_1 = \frac{[O_2^-][h^\bullet]}{p(O_2)} \qquad \text{eq. 48}$$

$$O_2^- + V_O^{\bullet\bullet} \underset{\overleftarrow{k}_2}{\overset{\vec{k}_2}{\rightleftharpoons}} O_{ad}^- + O_O^x + 2h^\bullet \qquad \text{r. 12} \qquad \Re_0 = \vec{k}_2 K_1 p(O_2)[V_O^{\bullet\bullet}][h^\bullet]^{-1} \qquad \text{eq. 49}$$

Substitution of $[h^\bullet]$ in eq. 49 with the relationship $[h^\bullet] \propto p(O_2)^{1/4}$ for bulk GDC yields $\Re_0 \propto p(O_2)^{3/4}$, which fits very well to the observed oxygen partial pressure exponents ranging between 0.6 – 0.8. It follows that additional to one $V_O^{\bullet\bullet}$ at least one hole is produced or one electron is consumed before *or* in the *rds*.

Regarding the observed $\Re_0 \propto [V_O^{\bullet\bullet}]$ for GDC, there is some discrepancy since according to eq. 1, the hole concentrations depends according to $[h^\bullet] \propto [V_O^{\bullet\bullet}]^{1/2}$ which overall results in $\Re_0 \propto [V_O^{\bullet\bullet}]^{1/2}$. A tentative consideration to resolve this discrepancy is the following: $[h^\bullet] \propto [V_O^{\bullet\bullet}]^{1/2}$ enters the rate expression as a consequence of the chemisorption equilibrium in eq. 48. If the system behaved ideally, K_1 would be independent of [Gd] and $[V_O^{\bullet\bullet}]$, but $[O_2^-]$ would decrease with increasing [Gd] and $[V_O^{\bullet\bullet}]$. However, the decreased effective cation charge with increasing Gd content might make the O_2 chemisorption increasingly favorable (deviation from ideal behavior) such that overall the $[O_2^-]$ becomes approximately independent of $[V_O^{\bullet\bullet}]$. Alternative mechanisms with two $V_O^{\bullet\bullet}$ involved before or in the

rds (leading to stronger $[V_O^{\bullet\bullet}]$ dependencies of $\Re_0$) are considered less probable as they require the encounter of adsorbed oxygen with two $V_O^{\bullet\bullet}$.

To derive an appropriate reaction mechanism which is in accordance with the experimental observations, a short summary of the results regarding PIE measurements is given:

(i) The equilibrium exchange rate on GDC shows a proportionality of $\Re_0 \propto [Gd]^1 \propto [V_O^{\bullet\bullet}]^1$. For PDC the relationship $\Re_0 \propto [Pr]^{3.5}$ (with $[Pr] \propto [V_O^{\bullet\bullet}]$) was observed. This indicates that in both cases, oxygen vacancies are involved in *or* before the *rds*.

(ii) The oxygen partial pressure dependence of the equilibrium exchange rate was found to be $\Re_0 \propto p(O_2)^{n>1/2}$ in all cases.

(iii) Since the exponent of the overall $p(O_2)$ dependence is between 0.5 and 1, this indicates that at least one electron is consumed or one hole is produced in *or* before the *rds*.

For GDC, the reaction mechanism depicted in figure 40 is consistent with these findings.

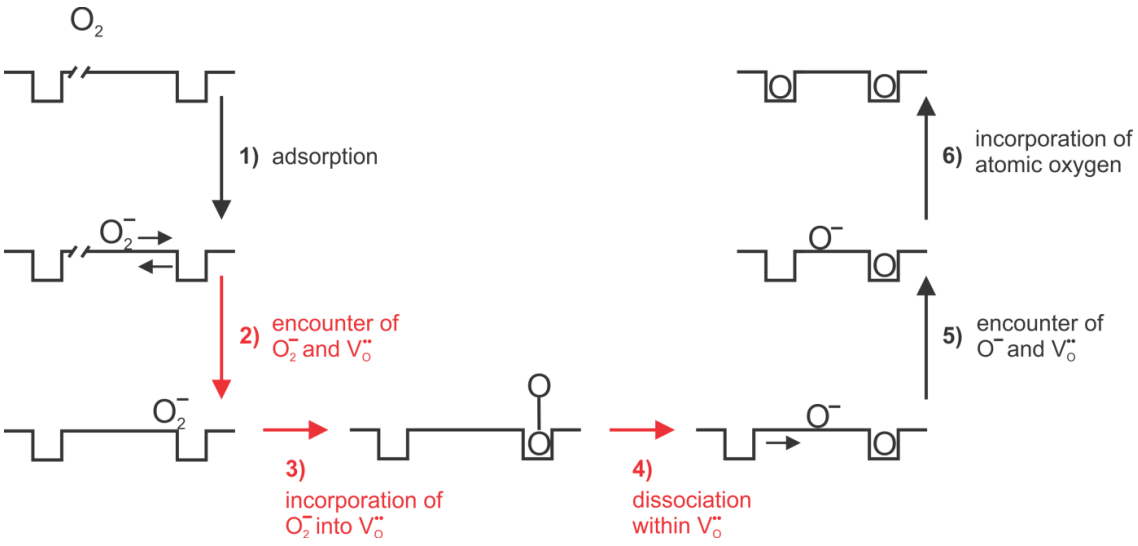

Figure 40: Proposed reaction mechanism for GDC consistent with the measured data. The charges of the oxygen intermediates are tentatively assigned since they cannot be directly concluded form PIE measurements. The rate-determining step is expected to be within steps 2 – 4, and are marked with red.

The adsorption of gaseous oxygen at the surface (step **1**) is expected to be fast. Such chemisorption processes occur on oxides already at room temperature or even below as found in literature[57, 117, 118]. It is most likely that oxygen adsorbs as a superoxide species (O_2^-). Although peroxide as well as superoxide (O_2^{2-}) species were found on reduced ceria[117] and redox–active perovskites like (La,Sr)$MnO_{3\pm\delta}$[119], the latter is less probable under oxidizing conditions since GDC is a large bandgap material.

The dissociation of oxygen without the involvement of an oxygen vacancy can be ruled out for GDC as well as for PDC since it was found that in addition to molecular oxygen also one $V_O^{\bullet\bullet}$ is involved in *or* before the *rds*. Hence, it is reasonable to assign that the incorporation proceeds by the encounter of a surface O_2^- with a surface $V_O^{\bullet\bullet}$ (step **2**). At this stage no unambiguous statement can be made whether O_2^- or $V_O^{\bullet\bullet}$ diffuses at the surface. However, on perovskites such as $Ba_{0.5}Sr_{0.5}Co_{0.8}Fe_{0.2}O_{3-\delta}$ or $(La,Sr)MnO_{3\pm\delta}$[62, 112] there is evidence that an oxygen vacancy approaches the adsorbed oxygen species. The next step **3** is the incorporation of the superoxide into an oxygen vacancy and the subsequent dissociative incorporation (step **4**). From DFT calculations for ceria[120] and perovskites[62] it was deduced that the dissociation of molecular oxygen is facilitated when it is first incorporated into an $V_O^{\bullet\bullet}$. Based on the present experimental observations, one of the steps **2 – 4** concluded to be rate–limiting.

In step **5**, the remaining oxygen atom encounters an oxygen vacancy and finally incorporates (step **6**). DFT calculations of the diffusivity of adsorbed oxide ions on the ceria (111) surface plane showed that on perfect ceria the O ion diffusion is unlikely to happen due to the large barrier of 1.58 eV. In contrast, in the oxygen vacancy-rich ceria structure, the oxygen ion can easily be inserted into a close–by oxygen vacancy.[120]

The charge of the adsorbed oxygen atom is assigned here only tentatively since from PIE measurements no direct conclusions about the charge can be drawn. Based on the observation that molecular oxygen is involved in the *rds*, the steps after the dissociative–incorporation (**5** and **6**) cannot be rate limiting. This implies that the concentration of O^- is larger compared to O_2^- (also observed for $(La,Sr)MnO_{3\pm\delta}$[62]), leading to a shorter diffusion length to an oxygen vacancy. Alternatively O^- as the mobile surface species would need to have a higher surface mobility compared to O_2^-. The assignment that the incorporation of O^- into $V_O^{\bullet\bullet}$ in step **6** is not rate–limiting may also imply that the similar step **3** is also not limiting.

Regarding PDC, the over–proportional increase with $\Re_0 \propto [Pr]^{3.5}$ is remarkable. A part of this strong correlation originates most likely due to the involvement of one oxygen vacancy in *or* before the *rds* as found for GDC, which yields $\Re_0 \propto [Pr]^1 \propto [V_O^{\bullet\bullet}]^1$. It is highly plausible that the remaining dependence of 2.5 originates from the intrinsic low temperature redox–activity of Pr in comparison to Ce. A reasonable hypothesis is that oxygen prefers to adsorb close to $Pr^{3+/4+}$ (Pr'_{Ce}/Pr^x_{Ce}) sites according to r. 13 and r. 14, which enter the oxygen incorporation reactions as a fast proceeding equilibrium:

$$O_2 + Pr'_{Ce} \rightleftharpoons O_2^- + Pr^x_{Ce} \qquad \text{r. 13}$$

$$O_2^- + Pr'_{Ce} \rightleftharpoons O_2^{2-} + Pr^x_{Ce} \qquad \text{r. 14}$$

From this, one can deduce that $[O_2^-]$ and $[O_2^{2-}]$ scale with $[Pr'_{Ce}/Pr^x_{Ce}]$ and $[Pr'_{Ce}/Pr^x_{Ce}]^2$, respectively, which would then increase the subsequent dissociation rate and yield $\Re_0 \propto [Pr]^3$ (together with the involvement of one $V_O^{\bullet\bullet}$ in the *rds*). Another aspect of Pr is the formation of an impurity band where the band width increases with increasing [Pr][27] (see section 2.1.2 and 4.1.2). This may facilitate the charge transfer from the surface to the adsorbed oxygen species $[O_2^-]$ and $[O_2^{2-}]$ (more negative adsorption energies) and further increase the dependence of $\Re_0$ on [Pr], yielding altogether $\Re_0 \propto [Pr]^{n>3}$. At present, a final conclusion about the detailed atomistic origin of the strong dependency of $\Re_0$ to [Pr] cannot be drawn.

4.2.3.2 Analysis of the Oxygen Isotopologue Fractions

In this section the analysis in terms of mechanisms M1, M2 as outlined in section 2.3.2 is applied. This analysis does not only consider the overall isotope fraction in the gas phase ($^{18}f_{g,i}$ and $^{18}f_{g,e}$) but also the distribution of the isotopologues $^{36}O_2$, $^{34}O_2$, $^{32}O_2$. As indicated in the appendix, this analysis yields meaningful results only when a perceptible amount of $^{34}O_2$ is formed. When $\Re_i \gg \Re_{da}$, only few $^{34}O_2$ are formed and the analysis yields $2\,^1\Re_{da} \approx \Re_0$ (M1) or $2\,^2\Re_{da} \approx \Re_0$ (M2), but the much higher $\Re_i$ comes with very large error bars that makes it unreliable.

Deconvolution of the different rates of the elementary steps proposed according to mechanisms M1 and M2 was carried out via eq. 25 to eq. 28. Figure 41 shows the results for 2PDC, 2GDC, 6GDC. Similar as for $SrTi_{1-x}Fe_xO_{3-\delta}$ in ref.[55], this analysis does not allow an unambiguous decision between M1 and M2 (however, the dopant and $p(O_2)$ dependence discussed in section 4.2.2 strongly favors M2). Also, similar to the analysis in ref.[55], M2 yields lower $\Re_i$ values (but similar $p(O_2)$ dependence) compared to M1.

For all data presented in figure 41, $\Re_{da} \leq \Re_i$ holds. The difference is greater at low $p(O_2)$. Within the error bars, $\Re_i$ has no pronounced $p(O_2)$ dependence, which is in line with the (largely) $p(O_2)$–independent oxygen vacancy concentration. $\Re_0 \approx 2\Re_{da}$ has a $p(O_2)$ dependence with an exponent in the range of 0.6 - 0.7, which is in line with molecular oxygen species in *or* before the *rds* plus contributions from defects with a negative $p(O_2)$ dependence.

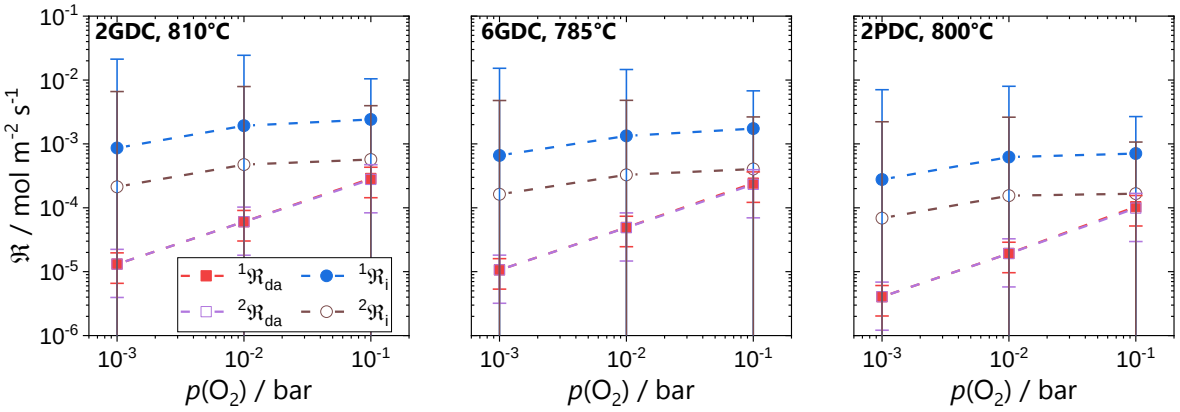

Figure 41: Calculated exchange rates of adsorption/dissociation $\Re_{ad}$ and incorporation $\Re_i$ by assuming mechanisms M1 or M2 (section 2.3.2) as a function of $p(O_2)$.

Overall, one can conclude that the analysis in terms of M2 is in agreement with the conclusions of section 4.2.2, and furthermore - for those samples with sufficiently high $^{34}O_2$ formation that allows for a reliable analysis - yields $\Re_{da}$ and $\Re_i$ values with a consistent $p(O_2)$ dependence.

4.2.3.3 Comparison of Oxygen Exchange Rates

To check whether the results obtained by PIE are comparable with other methods, isothermal mass relaxation after $p(O_2)$ change and isothermal isotope exchange experiments on 20PDC and 20TDC particles (in the same reactor as for PIE) were conducted and results from isothermal exchange line profiling (section 4.1.6) and literature were extracted.

The temperature dependence of the chemical oxygen surface exchange coefficient k^δ determined by TG is plotted for 20PDC and 20TDC for different oxygen partial pressures in figure 42a, and they all follow Arrhenius behavior. The apparent activation energies are ranging between 0.8 eV for 20TDC and 1.0 eV for 20PDC, and are half as large as E_a obtained by PIE (≈ 2 eV). The $p(O_2)$ dependence of k^δ is in line with the observed $p(O_2)$ dependence of $\Re_0$ with an exponent of about 0.6 (figure 42b), which substantiates the involvement of molecular oxygen in/before the rate–determining step of oxygen incorporation.

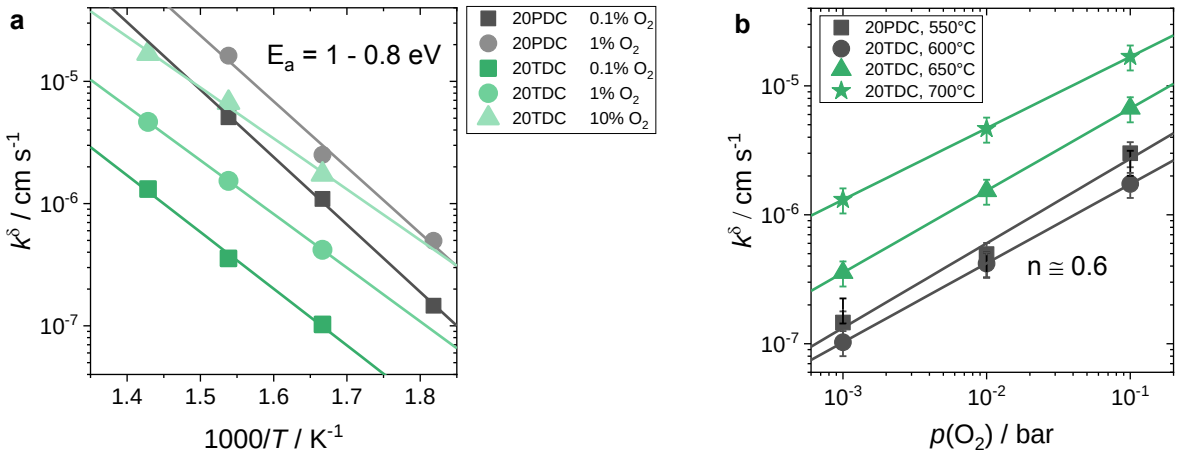

Figure 42: Results obtained by mass relaxation experiments by TGA. a) Temperature dependence of k^{δ} and b) $p(O_2)$ dependence of k^{δ} values for 20PDC/20TDC double annealed particles.

For PDC, the coefficient k^{δ} was transformed to the tracer oxygen surface exchange rate k^* by multiplying with the thermodynamic factor w in order to compare with literature and present PIE data (eq. 50). A mean thermodynamic factor of about 218 was extracted from TG measurements for 20PDC (500 °C to 800 °C, *cf.* section 4.1.5, within the error range, w only varies slightly with temperature).

$$k^{\delta} = k^* w \qquad \text{eq. 50}$$

For GDC and PDC the k^* values from this study are given in figure 43 and figure 44 as open symbols, and literature data are denoted by solid symbols. Overall, the data scatter by almost six orders of magnitude.

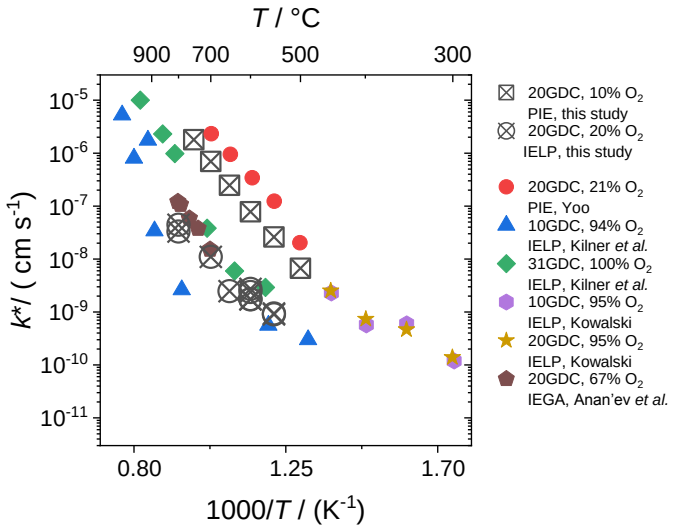

Figure 43: Exchange rates k^* obtained in this study and extracted from literature for GDC.

For GDC (figure 43), the data from Yoo[54] agree well with the present PIE study and both data sets connect reasonably well to IELP results at lower temperature[97]. The present IELP data of 20GDC particles are two orders of magnitude smaller than

the PIE data but agree very well to other exchange rates determined by IELP[95, 96] and isotope exchange gas phase analysis (IEGA)[121] and show similar slopes at temperatures above 500 °C.

The present k^* values for 20PDC obtained by PIE and isothermal isotope exchange (IIE) are in good agreement. For PDC (figure 44), the k^* values obtained by mass relaxation on 20PDC particles and isothermal exchange line profiling (IELP, section 4.1.6) on 20PDC dense pellets are comparable. The k^* values from mass relaxation experiments are three orders of magnitude smaller than the present PIE data for 20PDC and IIE of the same particles.

The latter two experiments deliver k^* values of comparable magnitude. They are also similar to the 20PDC data of Yoo[54], to the exchange rate for 10PDC measured by mass relaxation[122] (thin film, deposited on a $GaPO_4$ microbalance crystal) and to values for Pr_6O_{11} from IELP[123]. Values from impedance spectroscopy of 10PDC films on a YSZ substrate ($k^q = k^*$) are two orders of magnitude lower compared to 20PDC PIE data, but show a similar slope. They are comparable with the k^* values from present IELP and mass relaxation experiments. The smallest exchange rates were found by Ma *et al.*[124, 125] by *in situ* strain measurements on 10PDC thin films on YSZ substrates and by Kim *et al.*[126] by *in situ* optical absorption relaxation.

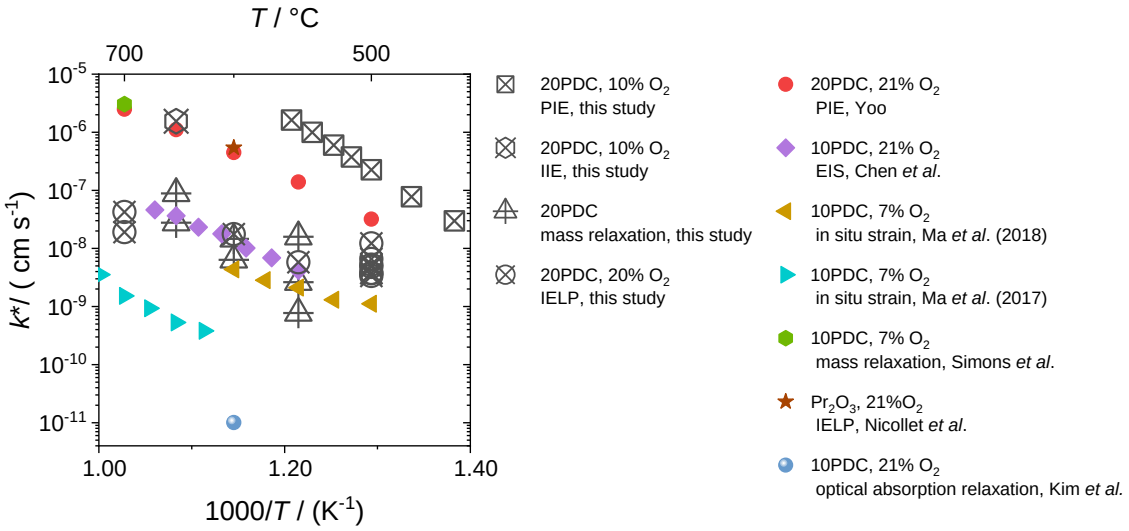

Figure 44: Exchange rates k^* obtained in this study and extracted from literature for PDC.

This comparison demonstrates the extreme sensitivity of the surface exchange rates to experimental details. Since in this study, the samples were never exposed to any precious metal (Au, Pt, etc.) which are known to catalyze the oxygen exchange reaction, such an effect is not the origin of the high exchange rates obtained by the present PIE study. Especially if the gas phase in the experimental setup is not absolutely dry, quartz glass can act as a SiO_2 source, which can form a thin glassy or silicate layer on mixed–conduction perovskites decreasing the

exchange rate[127]. Zhao *et al.*[128] found on 10PDC films an even stronger degradation of the exchange rate by more than 1.5 orders of magnitude. This might be related to the fact that ceria does not form silicate crystallites, but instead silica probably homogeneously covers large parts of the surface.

4.2.4 Pulsed Isotope Exchange of Doped Zirconia and Strontium Titanate

PIE measurements of Pr–doped zirconia (PDZ) and Fe–doped strontium titanate (STF) were conducted with approximately 20 mg calcined powders (SEM, XRD data and BET in section 4.3.1). SEM images of the analyzed calcined powders (figure 48 and figure 49) are less well-defined compared to the annealed particles investigated in section 4.2.2. Due to the smaller particle sizes, the pressure drop across the packed bed could not be kept lower than 10 %. Therefore, the absolute values of reaction rates here should not be directly compared to the results of annealed doped ceria particles in section 4.2.3.

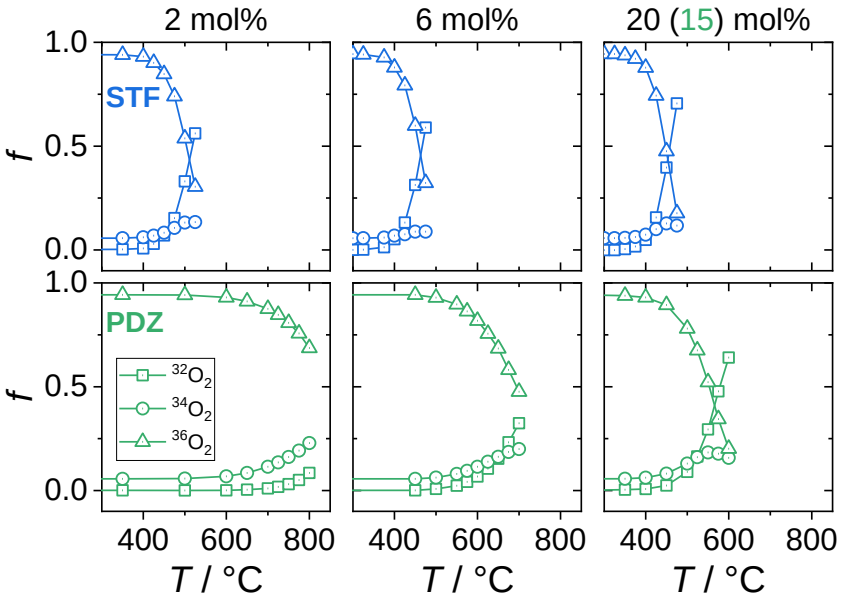

Figure 45: Fractions of the oxygen isotopologues measured at the exit of the reactor as function of reactor temperature for 2, 6 and 20 mol% Fe-doped strontium titanate (STF) and 2, 6, and 15 mol% Pr-doped zirconia (PDZ) calcined powders, measured in 10 % O_2.

The fractions of the oxygen isotopologues measured at the exit of the reactor are plotted in figure 45. The decrease of the onset temperature for oxygen incorporation with increasing dopant concentration is more pronounced for PDZ compared to STF. For STF, it shifts from 400 °C (2STF) to about 450 °C (20STF). In contrast, for 2PDZ, oxygen incorporation starts at 650 °C and the onset temperature lowers to 450 °C for 15PDZ. STF as well as PDZ show moderate $^{34}O_2$ formation for all dopant concentrations. This indicates that in contrast to Pr–doped ceria, a high Pr

concentration in doped zirconia seems not to sufficiently increase the rate of oxygen incorporation relative to adsorption/dissociation to prevent $^{34}O_2$ formation.

The temperature dependence of the equilibrium exchange rate follows Arrhenius behavior for STF and PDZ (figure 46a). The activation energy was calculated to be 1.8 eV for STF and 1.3 eV for PDZ (for comparison, E_a of PDC was around 1.7 - 2.4 eV).

Fe–doped strontium titanate is more active for oxygen incorporation than PDZ. STF shows a dependence of $\Re_0 \propto [Fe]^1$ (figure 46b). However, Yoo *et al.*[55] found a higher proportionality of $\Re_0 \propto [Fe]^{2.1}$ in a series of $SrTi_{1-x}Fe_xO_{3-\delta}$ with x = 0.01, 0.05, 0.35, 0.5. Nevertheless, if just the first two samples are considered (x = 0.01, and 0.05) the same dependence of $\Re_0$ on Fe content could be obtained as in the present study.

The equilibrium exchange rate of Pr–doped zirconia depends more strongly on the dopant concentration according to $\Re_0 \propto [Pr]^{1.6}$. PDZ is less active for oxygen incorporation when compared to calcined PDC powders. $\Re_0$ values for PDC calcined powder samples are proportional to [Pr] by $\Re_0 \propto [Pr]^{1.9}$, which is lower compared to the results obtained in section 4.2.3.1 on annealed PDC particles with $\Re_0 \propto [Pr]^{3.5}$. The reason for this discrepancy may originate from the different maximum temperature which the samples have seen (800 °C for the calcined powders and 1400 °C for annealed particles), but also the different temperatures to which $\Re_0$ has been extrapolated to.

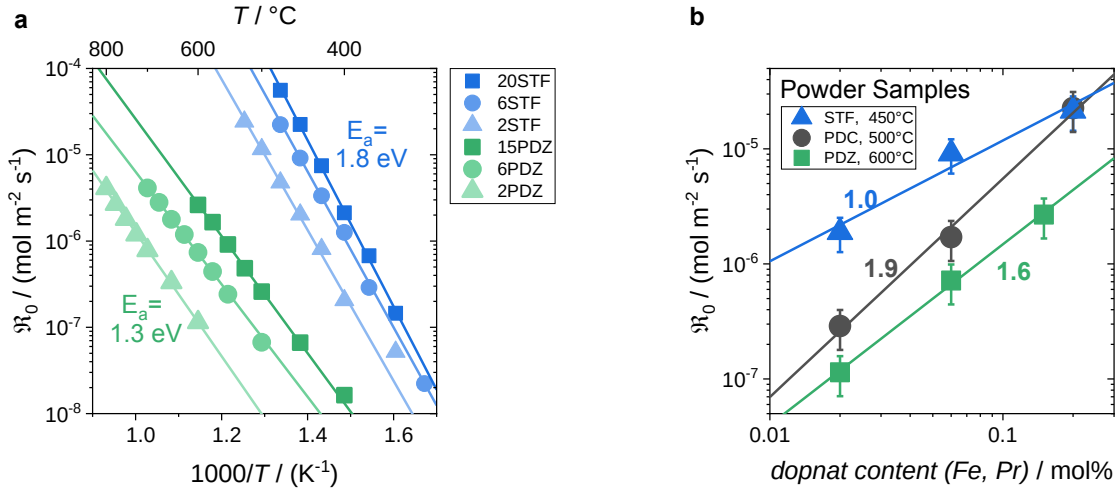

Figure 46: a) Arrhenius diagram for STF and PDZ. b) Dopant dependence of the equilibrium exchange rate extra/interpolated at 450 °C for STF, 600 °C for PDZ and 500 °C for PDC calcined powders. Measurements have been performed in 10 % O_2.

Nevertheless, similar to PDC the exponent of the dopant concentration dependence > 1 indicates that oxygen might preferably adsorb near $Pr^{3+/4+}$ sites,

and that charge transfer is facilitated due to the broadening of the Pr impurity band with increasing [Pr] as discussed in section 4.2.3.2.

4.2.5 Conclusion

For an extended set of single and double doped ceria with Gd, Pr, Nb, Tb, and of a series of Fe–doped strontium titanate and Pr–doped zirconia, the equilibrium oxygen exchange rate was determined by pulsed isotopic exchange. This dataset was expanded by measuring the oxygen exchange rate coefficients via mass relaxation, isothermal isotope exchange and isothermal isotope exchange line profiling for 20GDC, 20PDC and 20TDC.

The highest reaction rates were found when oxygen vacancies and redox-active centers are available. The equilibrium exchange rate clearly correlates with the dopant concentration. Together with oxygen partial pressure dependence a mechanism of oxygen incorporation was derived, which matches the experimental observations. Additional doping of PDC/GDC with Nb led to a decrease of the equilibrium exchange rate, supporting the interpretation that the effect of doping is to a significant part due to the role of oxygen vacancies.

For GDC, molecular oxygen is involved in the *rds* and oxygen vacancies appear in *or* before the *rds*. For PDC, the strongest increase of the equilibrium exchange rate with increasing Pr concentration was observed compared to other samples in the present study. At 700 °C, 20PDC accelerates $\Re_0$ by five orders of magnitude compared to undoped ceria. This steep increase is assigned to the involvement of an oxygen vacancy in *or* before the *rds* and to facilitated electron transfer to adsorbed oxygen due to the formation of a Pr impurity band, which increases the adsorbate coverage. Tb–doped ceria behave similarly due to closely related defect chemical behavior compared to PDC and probably follows the same mechanism. Fe–doped strontium titanate and Pr–doped zirconia show smaller dependences of the equilibrium exchange rates on the dopant concentration than PDC. This might be related to different sample thermal history/morphology. Nevertheless, a clear correlation of $\Re_0$ with Fe and Pr concentration emphasizes the importance of doping with redox-active cations for high oxygen exchange activity.

The absence of $^{34}O_2$ formation in case of PDC and TDC indicates higher oxygen ion diffusivities compared to GDC, which was confirmed by isothermal isotope exchange line profiling. Compared to 20GDC, the diffusivity of 20PDC is higher at $T < 800$ °C and shows an activation energy of 0.5 eV (1 eV for 20GDC). This increased diffusivity might be related to a lower migration barrier along Pr^{3+}/P^{4+} redox–couples.

Furthermore, it was shown that the surface reaction rate is very sensitive to experimental details like surface poisoning or catalytically impurities than bulk properties emphasizing the importance to investigate a systematically doped set by the same method.

4.3 Carbon Monoxide and Methane Oxidation

In this chapter the CO and CH_4 oxidation (with the focus on doped ceria) are presented. The scope of this part is to elucidate whether the type and amount of dopant in ceria influences the reaction rate to a comparable magnitude as for oxygen exchange (section 4.2). The reactions are conducted under continuous flow conditions in a packed bed reactor and the reactions are in a steady-state.

Methane and carbon monoxide oxidation reactions follow the so–called Mars-van-Krevelen mechanism[129] in which CO or CH_4 are oxidized to CO_2 by reacting with lattice oxygen as depicted in figure 47. The catalyst gets reduced (formation of oxygen vacancies) and is recovered by re-oxidation with gas phase O_2 (refilling of lattice oxygen). One of those two processes can be rate-limiting.

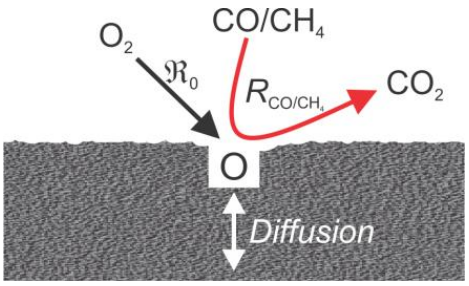

Figure 47: Schematic of CO/CH_4 oxidation on a solid metal oxide catalyst.

The re-oxidation branch describes the oxygen exchange reaction. If this reaction is rate-limiting, similar dependencies of the CO/CH_4 oxidation reaction rate on oxygen partial pressure, dopant type and concentration are expected as found for oxygen exchange in section 4.2.3. In case of a rate-limiting behavior of the methane or carbon monoxide oxidation (catalyst reduction), this is not necessarily the case.

Since CO oxidation is a rather simple reaction a reasonable reaction mechanism can be deduced from the present experimental data. For the more complex CH_4 oxidation the focus was mainly to elucidate which defect species are involved in the rate–determining step

4.3.1 Sample Characteristics

Methane and carbon monoxide oxidation were performed in an Al_2O_3 reactor with SiO_2 wool as catalyst support. Since for the double–annealed particles significant conversion of reactants was observed only at temperatures above 800 °C, calcined powders with higher surface area are investigated here. The sample mass in the packed bed reactor was 15 – 25 mg with a bed height between 4 – 8 mm.

Table 15: BET areas of doped ceria, zirconia, and strontium titanate powders investigated through CO and CH_4 oxidation.

Sample	BET / $m^2\ g^{-1}$	Sample	BET / $m^2\ g^{-1}$
20PDC	20.8	15PDZ	35.8
6PDC	24.6	6PDZ	10.3
2PDC	23.8	2PDZ	4.4
0.6PDC	21.0	20STF	2.0
20GDC	20.6	6STF	3.6
2GDC	17.5	2STF	3.4
2NDC	17.6	0.6STF	2.8
YSZ	13.5		

The corresponding BET areas of the samples are listed in table 15. The surface areas are comparable among each system, only for Pr–doped zirconia the BET area decreases strongly with decreasing Pr content. All Pr–, Gd–, and Nb–doped ceria powders are similar in their morphologies (figure 48a–b). They form flakes with a size of several hundred nanometers, which agglomerate to porous particles with a size of up to 100 µm.

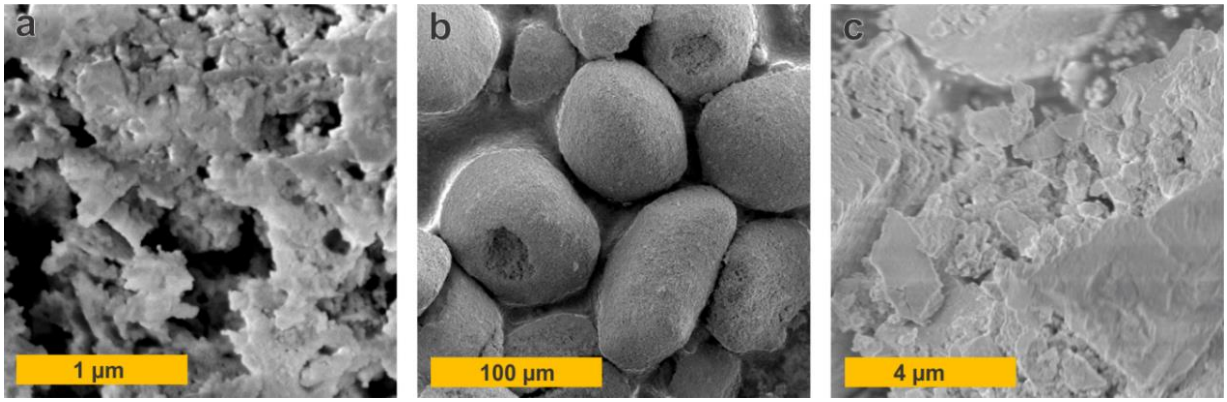

Figure 48: SEM images of a) 20PDC powder, b) 20PDC powder agglomerates, and c) 15PDZ powder.

The morphology of Pr–doped zirconia powder is less well defined, the particle size varies strongly (figure 48c). Fe–doped strontium titanate powders appear more uniformly in the form of small agglomerated crystallites with a size of approximately 1 – 2 µm, which is typical for perovskite powders prepared by solid oxide synthesis.

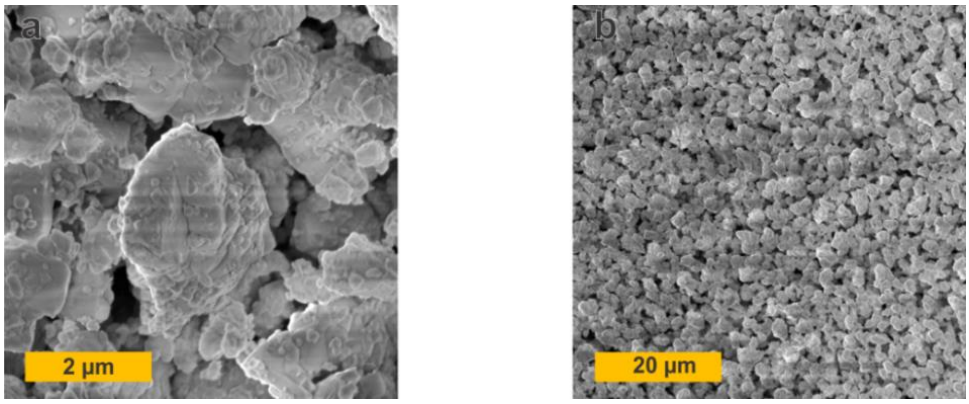

Figure 49: SEM images 20STF powders.

Lattice parameters for the samples are listed in table 16. XRD measurements on Pr/Gd and Nb–doped ceria calcined powers showed phase pure fluorite type crystal structure (figure 50a). For 15 mol% Pr–doped zirconia, the XRD pattern showed a phase pure cubic structure, while for lower Pr concentration the diffraction pattern matched to a tetragonal crystal structure. Fe–doped strontium titanate was phase pure with a cubic crystal structure; only in 20STF small amounts of a tetragonal phase appeared (figure 50b).

Table 16: Extracted lattice parameter for Pr, Gd, and Nb doped ceria, YSZ, Pr–doped zirconia (2PDZ and 6PDZ are tetragonal) and Fe–doped strontium titanate.

Sample	*a* / Å	Sample	*(a, b), c* / Å
20PDC	5.4120	YSZ	5.1409
6PDC	5.4118	15PDZ	5.1559
2PDC	5.4103	6PDZ	3.5970, 5.1683
0.6PDC	5.4118	2PDZ	3.5980, 5.1866
20GDC	5.4196	20STF	3.9025
2GDC	5.4079	6STF	3.9059
2NDC	5.4147	2STF	3.9066
		0.6STF	3.9060

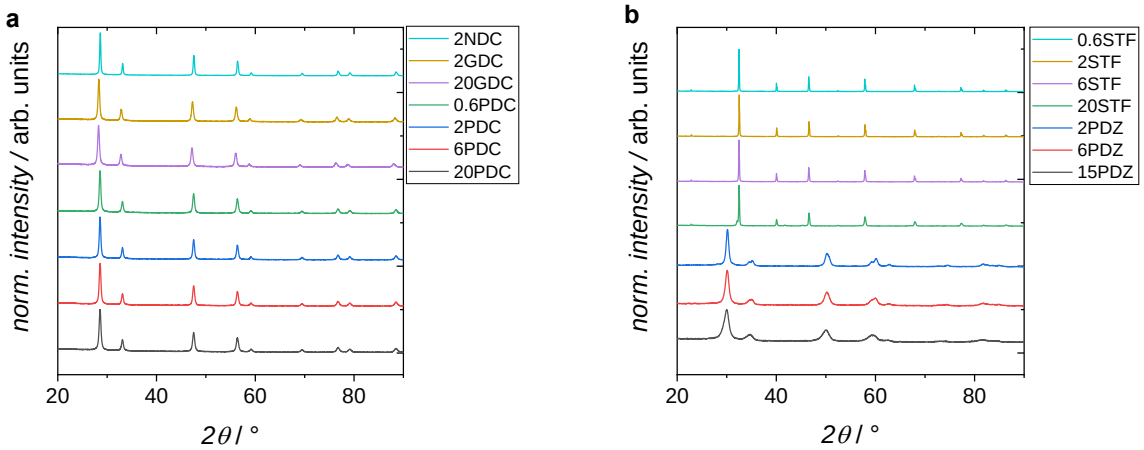

Figure 50: XRD pattern of calcined powders. a) PDC; GDC and 2NDC. b) STF and PDZ.

4.3.2 Raw Data

The mass balance of carbon, hydrogen and oxygen was always checked. The deviation from the mass balance for carbon and oxygen is in the range of ±2 – 5 % for both, CO and CH_4 oxidation (figure 51a, b). In case of hydrogen, the deviation is up to ±10 % as can be seen for CH_4 oxidation from figure 51b.

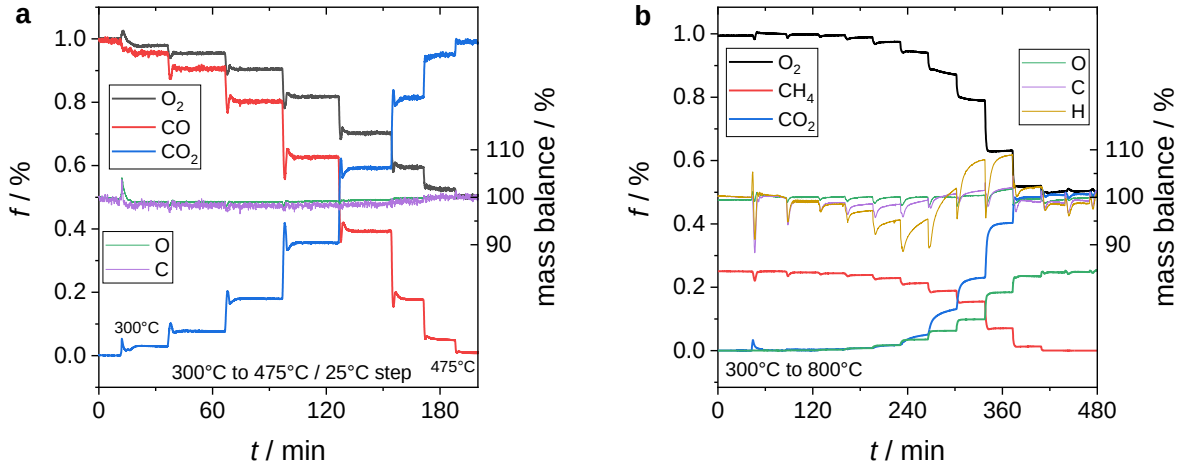

Figure 51: Measured reactant and product gas phase fractions for a) CO and b) CH_4 oxidation for 20GDC in 1 %O_2 with 1 %CO or 0.25 % CH_4 with a flow rate of 10 mL min^{-1}. The right scale displays the deviation from the mass balance.

The probed catalysts reached a steady state (constant reactant conversion) already after a few minutes. The data presented in figure 51a and b is for 20GDC, but are representative for all samples.

4.3.3 Carbon Monoxide Oxidation

4.3.3.1 Results and Discussion

The conversion of carbon monoxide is plotted in figure 52a as a function of reactor temperature in an atmosphere of 1 % O_2 and 1 % CO (oxidizing conditions even for complete CO conversion) for PDC, GDC, 2NDC and YSZ. All samples follow temperature dependences of Arrhenius type (figure 52b). The activation energies for 2NDC, PDC, and GDC were in the range of 0.8 – 0.9 eV. YSZ showed a higher E_a of 1.5 eV.

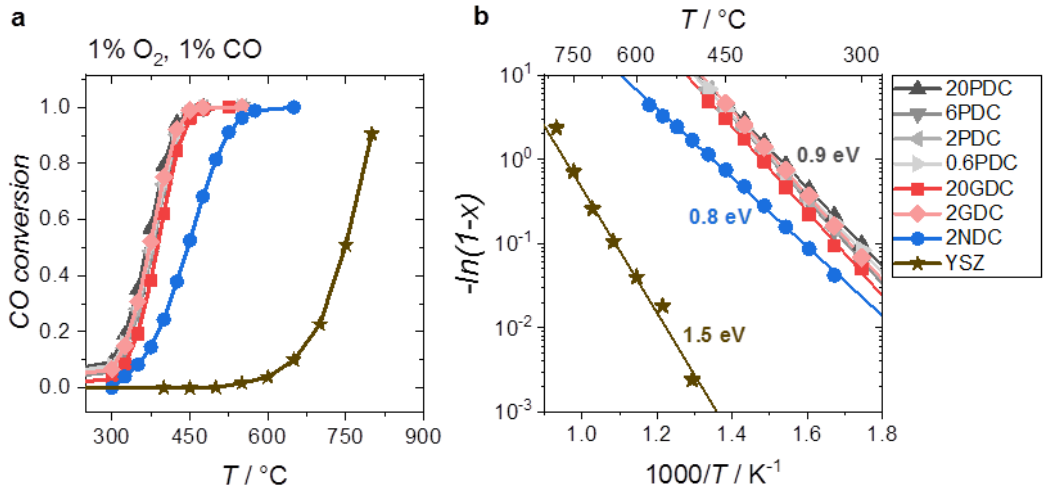

Figure 52: a) CO conversion and b) Arrhenius plot for Pr–, Gd–, and Nb–doped ceria and 14 mol% Y stabilized zirconia (YSZ, TOSOH TZ-8).

The Pr doped ceria samples (black/gray symbols, figure 52a) exhibit identical CO conversions. The reaction starts at around 300 °C and reaches full conversion at 450 °C. 2GDC and 20GDC (red symbols) behave similarly. For 2NDC (blue), the onset temperature for CO conversion shifts to higher temperatures and full conversion is attained at 550 °C. For YSZ, which has no intrinsic redox behavior, the CO conversion starts only at 600 °C and reaches full conversion above 800 °C.

The CO conversion for Pr doped zirconia and Fe doped strontium titanate are plotted in figure 53a. From figure 53b, the Arrhenius type temperature dependence of the conversion can be seen, the activation energy is higher compared to doped ceria with values between 1.0 – 1.6 eV. For PDZ, the onset temperature for CO conversion shifts to higher temperature with decreasing Pr concentration. Similarly, the onset temperature increases for STF with decreasing Fe concentration.

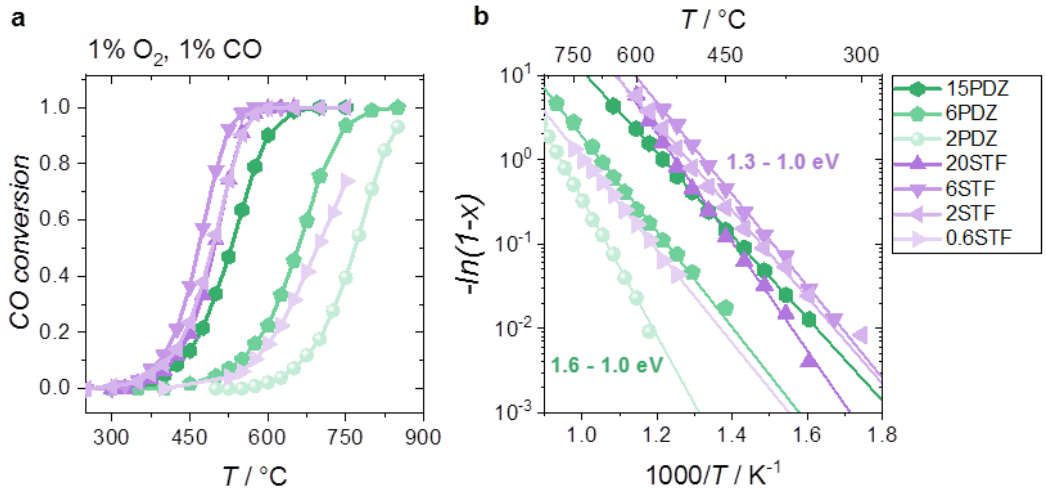

Figure 53: a) CO conversion and b) Arrhenius plot for Pr-doped zirconia (PDZ) and iron doped strontium titanate (STF).

The activation energy for all samples are summarized in figure 54a. Whereas for PDC and GDC, the activation energy is almost constant with increasing dopant concentration, STF and PDZ show different behavior. For STF, E_a tend to increases from around 1 eV at small Fe concentration to around 1.3 eV at high [Fe]. PDZ follows an opposite trend: with increasing Pr concentration, E_a decreases from 1.6 to 1.0 eV.

The results in figure 52 and figure 53 do not consider the specific surface area. For a quantitative comparison, the apparent reaction rates R_{CO} (see eq. 9) were calculated at low conversion (<20 %) by normalizing to the surface area of the samples in figure 54b. The apparent reaction rates were inter/extrapolated to a common temperature: 350 °C for the doped ceria system and 500 °C for Fe–doped strontium titanate and Pr/Y–doped zirconia.

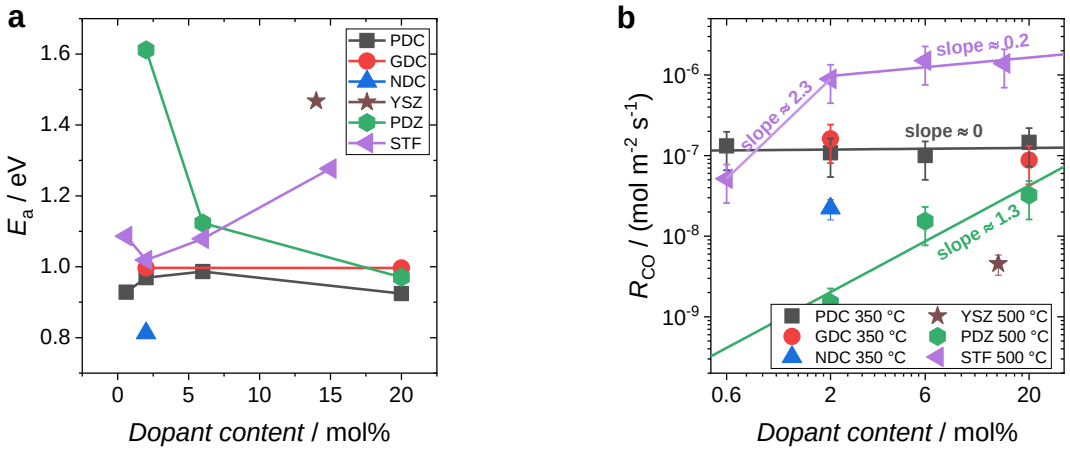

Figure 54: a) Dopant dependence of the activation energy of CO oxidation. b) Dopant dependence of the apparent reaction rate R_{CO}.

Within the experimental error, no dopant dependence of R_{CO} was found for Pr and Gd–doped ceria (figure 54b). This indicates that the intrinsic redox-activity of ceria itself is sufficed to reach a good CO oxidation performance. Similarly, Wilkes and coworkers[130] found that the CO oxidation reaction rate differs only slightly for 20PDC (0.031 mol $h^{-1}m^{-2}$) and 20GDC (0.019 mol $h^{-1}m^{-2}$) at 560 °C. The absence of the dependence of R_{CO} on [Gd] and hence $[V_O^{\bullet\bullet}]$, indicates that an increased amount of $V_O^{\bullet\bullet}$ do not significantly accelerates the reaction. The depletion of the reaction rate for 2NDC might be related to the absence of any oxygen vacancy at the surface and/or to the less easy reducibility due to its n-type character.

At 500 °C, YSZ shows a R_{CO} value, which is 1.5 orders of magnitude smaller compared to GDC/PDC. Extrapolated to 300 °C, R_{CO} for YSZ yields about $1x10^{-13}$ mol $m^{-2}s^{-1}$ (not shown in figure 54b). The large difference of R_{CO} by six orders of magnitude to Pr/GD/Nb-doped ceria strongly indicates that redox-activity of the underlying catalyst material is essential for good CO oxidation performance.

In Pr–doped zirconia, only Pr shows redox-activity. Therefore, it is not surprising that the reaction rate of CO oxidation depends on the Pr concentration with $R_{CO} \propto [Pr]^{1.3}$. The apparent reaction rate for Fe–doped strontium titanate shows strong dopant dependence between 0.6STF and 2STF with a slope of 2.3. The dependence reaches a plateau at high Fe concentrations with a very weak slope of 0.2, which is comparable to the independence of R_{CO} on [Pr] in doped ceria.

Carbon monoxide and oxygen partial pressure dependence of the apparent reaction rates R_{CO} was measured only for the doped ceria systems PDC, GDC, and 2NDC. The results are given in figure 55a and figure 55b.

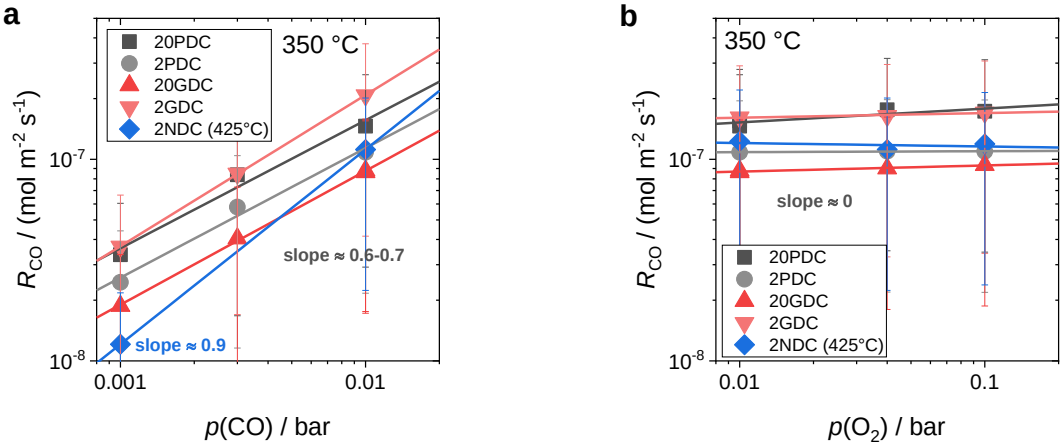

Figure 55: Dependence of the CO oxidation reaction rate R_{CO} to a) CO partial pressure, and b) oxygen partial pressure.

On GDC and PDC, R_{CO} is proportional to $R_{CO} \propto p(CO)^{0.6}$, and 2NDC yields and exponent of 0.7. No $p(O_2)$ dependence was found for those samples. These findings indicate that the reduction of the catalyst by CO is rate determining rather than the re-oxidation. Experimental studies on Zr doped ceria[131], and undoped ceria[130, 132] also observed an apparent reaction order for CO between 0.6 and 0.8, and a zero reaction order for oxygen. Temperature programmed desorption of oxygen from ceria indicated that the interaction between the underlying catalyst and O_2 molecules does not significantly influence the CO oxidation activity, and that rather the extraction of lattice oxygen (the reduction of the catalyst) is the rate-determining step.[133]

The data in figure 56 show that the condition $R_{CO} > \Re_0$ holds for 20PDC at temperatures below 400°C, and for 6, and 2PDC below 550 and 750°C, respectively. All PDC and GDC reaction rates from figure 52b fall into this regime of $R_{CO} > \Re_0$. This suggests two possibilities for the low temperature range: (i) The oxidation of the catalyst might be rate-determining. (ii) The catalyst develops a decreased lattice oxygen concentration, since within the same time-interval more lattice oxygen reacts with CO to CO_2 than is replenished by O_2.

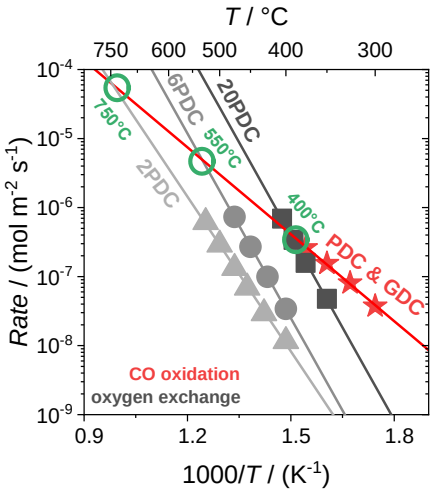

Figure 56: Plot of the apparent reaction rate R_{CO} of CO oxidation of PDC powder samples and the equilibrium exchange rate $\Re_0$ of oxygen incorporation for 2, 6, and 20PDC powder samples. Since PDC and GDC behave similar, the red colored data is also representative for GDC

Assumption (i) can be ruled out, since the $p(O_2)$ dependence of R_{CO} at 350 °C (*e.g.*, when $R_{CO} > \Re_0$) was measured to be zero and hence, the oxygen incorporation is not the *rds*. To test assumption (ii), *in situ* CO oxidation was performed in the thermogravimetry setup. Reversibility is given because the mass loss during heating and cooling agree hence, the date in figure 57 represents a true steady-state.

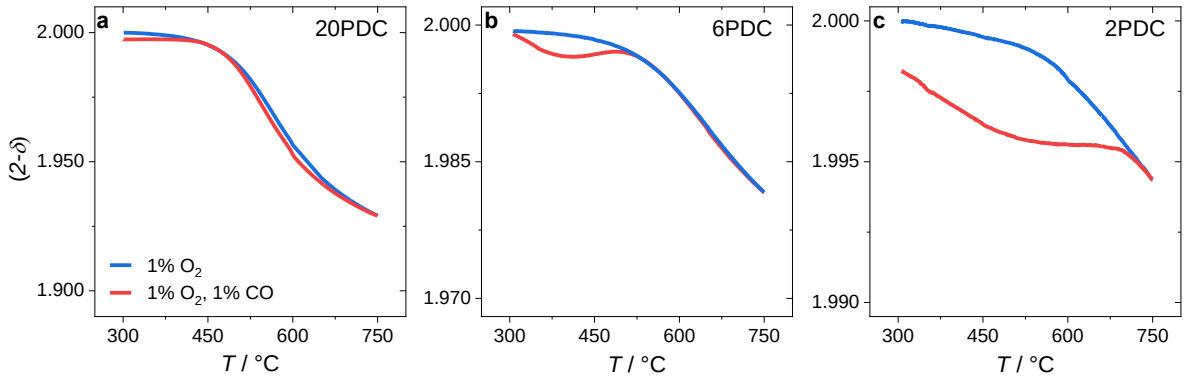

Figure 57: Change of oxygen non-stoichiometry as a function of temperature for a) 20PDC, b) 6PDC, and c) 2PDC. The blue curve was obtained in 1 % O_2 and the red curve was measured in 1 % O_2 plus 1 % CO.

Figure 57 compares the oxygen non-stoichiometry as a function of temperature for PDC samples measured in 1 % O_2 (blue) and with additional 1 % CO (red). With decreasing Pr concentration and at lower T, the oxygen deficit increases when CO is present relative to the measurements in oxygen. At temperatures matching approximately those temperatures of the intersection points in figure 56 ($R_{CO} = \Re_0$), the lattice oxygen concentration approaches the values in 1 % O_2, *i.e.* oxygen extraction by CO oxidation and oxygen replenishment by O_2 are balanced at this point. In other words, in the regime where the oxygen incorporation reaction is slower compared to the CO reaction, the catalyst indeed shows a strong relative oxygen deficit, and the Pr doped ceria particles experience a kinetically determined

decreased effective oxygen activity $p(O_2)_{eff}$. With decreasing Pr concentration the relative magnitude of the deficit increases. The $p(O_2)_{eff}$ values can be estimated by extrapolating $p(O_2)$ to the observed δ (using (2-δ) values will produce a large error) from TGA data obtained at different $p(O_2)$. A decreased effective oxygen partial pressure was also observed on $Sr(Fe_{0.5}Ti_{0.5})O_{3-\delta}$ during CO oxidation at T < 550 °C by Vračar.[5]

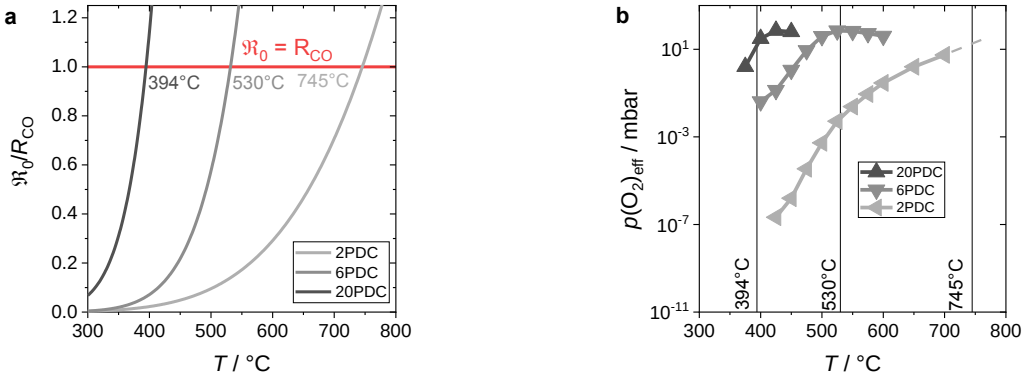

Figure 58: a) Ratio of equilibrium exchange rate of oxygen incorporation $\Re_0$ and CO oxidation R_{CO} as a function of temperature. The intersection with the horizontal line represents the situation where $R_{CO} = \Re_0$. b) Kinetically determined effective oxygen partial pressure $p(O_2)_{eff}$ within the PDC catalyst particles as a function of temperature.

For 6PDC and 2PDC where the deviation of (2-δ) in CO/O_2 atmosphere is large, $p(O_2)_{eff}$ reaches very low values, *e.g.*, a $p(O_2)_{eff}$ of around $1x10^{-6}$ at 450 °C (figure 58b), which corresponds to strongly reducing conditions.

In the observed steady-state, the oxygen incorporation is not the *rds* because more oxygen vacancies and electronic defects are created at the surface by CO oxidation, which accelerates the oxygen incorporation. Additionally, the reduced lattice oxygen concentration decelerates the CO oxidation rate until R_{CO} and $\Re_0$ are balanced and the steady-state is reached. The slower oxygen exchange kinetics for PDC samples with small [Pr] results into decreased $p(O_2)_{eff}$ with decreasing [Pr]. At the beginning of the reaction, CO oxidation proceeds by consuming the present stock of lattice oxygen. Only when an appropriate amount of oxygen vacancies and electronic defects are created in the further approach of the reaction, the oxygen incorporation accelerates. At this point the PDC exhibits a steady-state oxygen deficit, since enough oxygen is replenished due to the faster oxygen exchange kinetics. With increasing temperature $\Re_0$ increases more steeply than R_{CO} (figure 56), the oxygen deficit decreases and $p(O_2)_{eff}$ increases, until at some point $p(O_2) \approx p(O_2)_{eff}$.

Also 2NDC ceria shows this kind of behavior as one can see from figure 59a where the mass change of 2NDC is given as a function of temperature in oxygen and in additional CO atmosphere. The relative larger mass gain in 1 % O_2 at lower

temperature is due to the formation of oxygen interstitials[23], which is absent when the pressure of CO leads to a decreased $p(O_2)_{eff}$.

The mass change for 20GDC and 2GDC in 1% CO and 1 % O_2 in figure 59b is very low, approximately one order of magnitude lower for 20GDC and two orders of magnitude lower for 2GDC when compared to 2PDC, which makes these TGA measurements on GDC quantitatively not reliable.

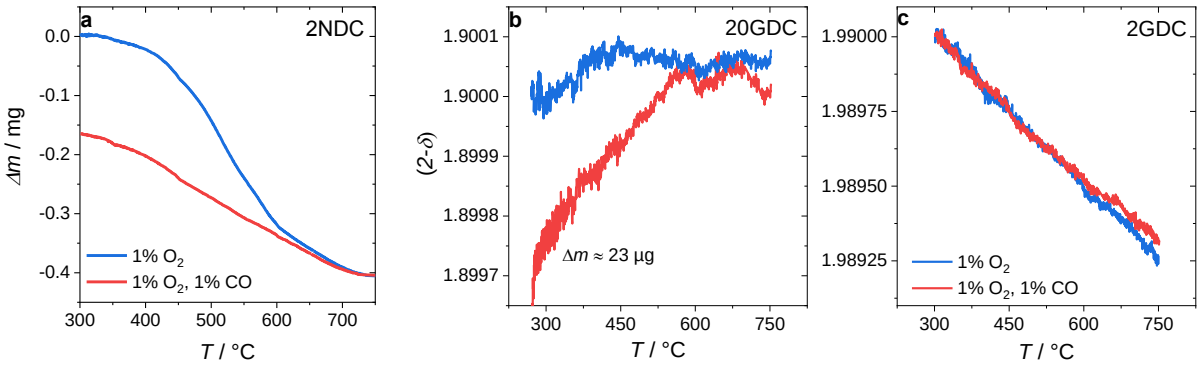

Figure 59: Change of oxygen non-stoichiometry as a function of temperature for a) 2NDC, b) 20GDC, and c) 2GDC. The blue curve was obtained in 1 % O_2 and the red curve was measured in 1 % O_2 plus 1 % CO

Therefore, CO oxidation was also investigated by *in situ* by impedance spectroscopy on porous 2GDC and 20GDC pellets. The porosity allows fast equilibration of oxygen stoichiometry even at low temperature. The Nyquist plot for 2GDC at 350 °C in in 1 % O_2 and 1 % O_2/1 % CO is shown in figure 60.

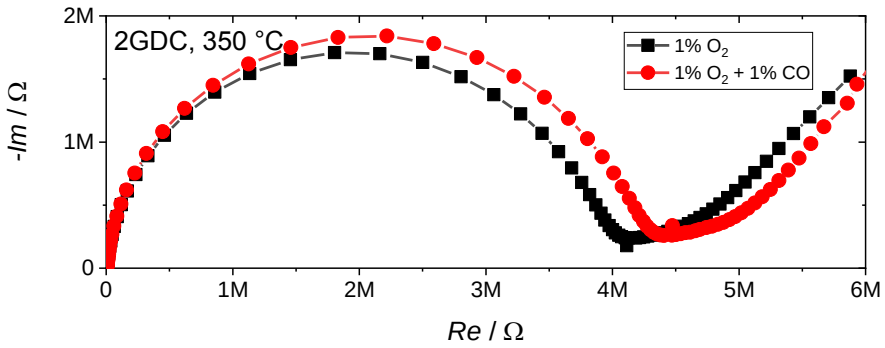

Figure 60: Nyquist plot for 2GDC at 350°C in 1 % O_2 and additional 1 % CO.

The low frequency arc in figure 60 is attributed to bulk processes with a capacity of about 10^{-12} F, whereas the low frequency arc represents processes at the Au electrode with a capacity of about 10^{-6} F. No clear separation of a grain boundary arc was observed. The extracted bulk resistance R_B of the first semicircle is plotted in figure 61a and b for 2GDC and 20GDC, respectively. In the presence of CO and O_2, the resistance increases, and decreases again when no CO is present (which is not fully reversible). In case of 2GDC the change of R_B is about 10 %, and is significantly higher compared to 20GDC (figure 62a). The increase of the bulk

resistance in the presence of CO can be explained by considering that GDC is a mixed ionic and p-type electronic conductor under oxidizing conditions with a small, but not completely negligible p–type contribution (literature data[35, 36] in figure 62b). It amounts to 3 % at 750 °C and 0.3 % at 600 °C in 10 % O_2 according to refs. [35, 36]; the data from ref [36] yields even higher values.

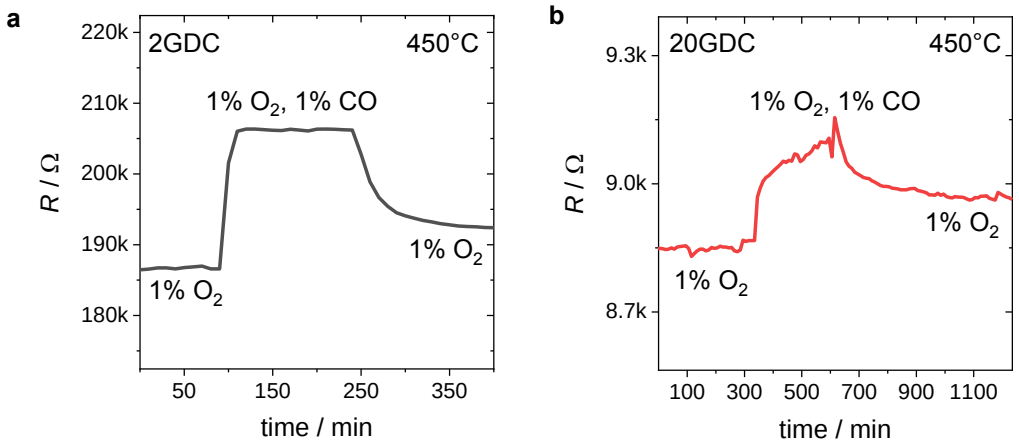

Figure 61: Extracted bulk resistance for a) 2GDC and b) 20GDC. Measurements were conducted in 1 % O_2 and additional 1 % CO.

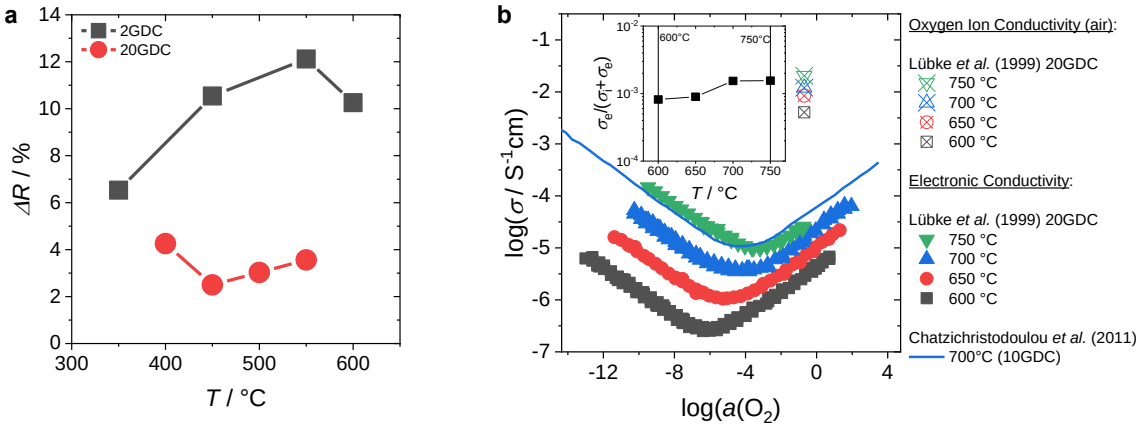

Figure 62: a) Relative difference of the bulk resistance of 2 and 20GDC. The reference point is the resistance measured in 1 % O_2. b) Electronic conductivities of GDC. The data was taken from ref.[35, 36], *a* denotes the oxygen activity. The inset displays the electronic transference number calculated from the ionic and electronic conductivity from ref.[36]

Since the oxidation of CO to CO_2 produces electrons (annihilation of electron holes), the conductivity in the p-type regime decreases (hence the resistance increases). Therefore, the data in figure 61 indicates that also the GDC particles experience an effective reduced oxygen partial pressure. For 20GDC, this relative increase of the bulk resistance is smaller compared to 2GDC, probably due to the smaller electronic transference number in 20GDC. However, impedance measurements of the present 20GDC porous pellets in 0.1 and 100 % O_2 did not show any change of the bulk conductivity (see figure 63), which would indicate p-type conductivity. Therefore, it should be mentioned here that the above

explanation is based on a comparison to literature values of samples with different history and should be taken with caution.

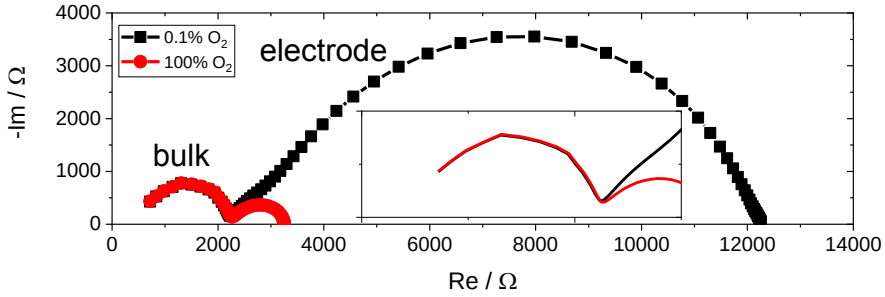

Figure 63: Impedance spectra of 20GDC porous pellet measured in 100% O_2 (red) and 0.1% O_2 (black). The inset shows the magnification of the first arc.

4.3.3.2 Mechanism of CO Oxidation on Ceria

At this point, a short summary of the results of the present study is given:

(i) The CO oxidation rates are similar for PDC and GDC, hence the intrinsic redox-activity of ceria is sufficient for a good CO oxidation performance.

(ii) R_{CO} depends on [Pr] in PDZ and on [Fe] in STF and the lowest R_{CO} was found on the redox-inactive YSZ, emphasizing the importance of redox properties/electronic defects of the catalyst.

(iii) The CO oxidation rate does not depend on [Pr] or [Gd]. Therefore, the increasing $[V_O^{\bullet\bullet}]$ over the intrinsic surface $[V_O^{\bullet\bullet}]$ of undoped ceria (in particular for decreased $p(O_2)_{eff}$) does not influence R_{CO}.

(iv) The observation of a zero reaction order of R_{CO} on $p(O_2)$ and a reaction order between 0.6 and 0.9 on $p(CO)$ indicates that the reduction of the catalyst by CO is the *rds*, not the re-oxidation.

(v) R_{CO} of GDC/PDC and 2NDC is higher compared to $\Re_0$. This induces a kinetically determined decreased effective $p(O_2)$, which the catalyst experiences until both rates – R_{CO} and $\Re_0$ – are equal (figure 58). With increasing T, $\Re_0$ increases more strongly than R_{CO} until $R_{CO} = \Re_0$ and $p(O_2) = p(O_2)_{eff}$

(vi) The decreased $p(O_2)_{eff}$ accelerates the re–oxidation until a steady-state is reached. This self-balanced process is the reason why O_2 incorporation is not the *rds* under steady state conditions, at least in doped ceria.

It is accepted that CO oxidation proceeds on ceria by the Mars-van-Krevelen mechanism[129] (MvKM) where CO forms CO_2 by extracting lattice oxygen and not by reacting with adsorbed oxygen species. Breysse *et al.*[132] first showed that CO oxidation proceeds on ceria by the MvKM. This is also confirmed in the present study by performing pulsed CO oxidation experiments in a CO/^{18}O atmosphere,

where no formation of $C^{18}O^{16}O$ could be observed on 20GDC, 20PDC, 2PDC, 2NDC, 2PDZ, 0.6STF, and YSZ (results are exemplarily shown for 20PDC and 20GDC in figure 64).

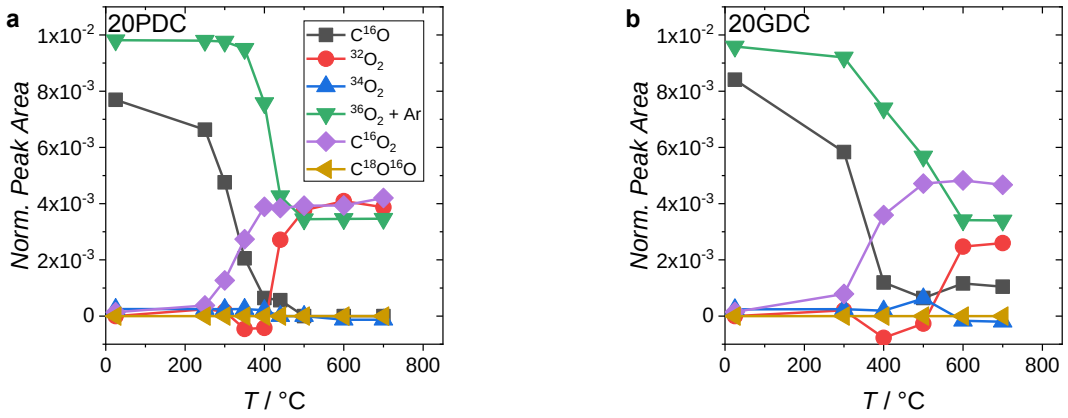

Figure 64: Pulsed CO / ^{18}O oxidation experiments performed on a) 20PDC and b) 20GDC. No formation of $C^{18}O^{16}O$ was observed.

The obtained peak areas could not be internally calibrated, hence no absolute concentrations could be extracted. The results clearly show the absence of $C^{18}O^{16}O$, *i.e.* the added O in the formed CO_2 comes from the lattice of the catalyst particles.

CO oxidation has been investigated in the literature for various oxides. XPS studies of CO oxidation on nanostructured Zr–doped ceria revealed the presence of a carbonate-like intermediate.[134] By *in situ*/*operando* spectroscopy on Mn–doped ceria[135] and *operando* DRIFTS measurements on undoped ceria[136] as well with IR spectroscopy on nanostructured Zr-doped ceria[137], formate, carboxylate, monodentate carbonate, bidentate carbonates and polydentate carbonate were found. Furthermore, Piumetti *el al.*[137] concluded that the carbonate-like intermediate formation facilitates the CO oxidation. ter Maar and coworkers[138] concluded from CO oxidation and temperature controlled reduction measurements and former ESR and IR studies for ThO_2 and UO_2 that CO oxidation on oxides with the fluorite or pyrochlore structure proceeds via an carbonate mediated MvKM. DFT calculations on Co–doped ceria haven been used to investigate a carbonate mediated MvKM. It was concluded that a carbonate–mediated MvKM is preferred on a (110) surface, whereas the CO oxidation on (111) and (100) surfaces follows the conventional MvKM.[139] Chen *et al.* showed by DFT calculation that on ceria (110) surfaces carbonate poisoning is most likely whereas the carbonate formation is not expected to occur on ceria (111). The results showed that the weak adsorption of CO to the surface (-0.2 eV) is followed by the reaction of CO with surface oxygen (which donates one electron to Ce) forming a bent $CO_{2\,ad}$ species and an oxygen vacancy, which represents the *rds*. No obvious barrier was observed when desorbing as CO_2 molecule.[140]

Additionally, the reducibility of the catalyst (which also correlates to the oxygen vacancy formation energy) is an important parameter. The presence of redox-active cations in the catalyst is crucial for the CO oxidation mechanism. For pristine Al_2O_3, the CO oxidation is endothermic and oxygen vacancies are formed *in* the *rds* of CO oxidation. On the other hand, on Ni-α-Al_2O_3 the overall reaction is exothermic and the oxygen vacancy formation proceeds *after* the *rds*[141]. This is in line with the observed absence of any $V_O^{\bullet\bullet}$ dependence of R_{CO} in the present study. Therefore, it is reasonable to assume that in case for ceria the formation of $V_O^{\bullet\bullet}$ occurs after the rate-determining step. The correlation of the low reaction rate for the present YSZ sample with the absence of reducible cations also emphasizes the importance of the catalyst to be an electron acceptor.

From the present experimental results and considering the literature, the mechanism suggested in figure 65 seems to be plausible:

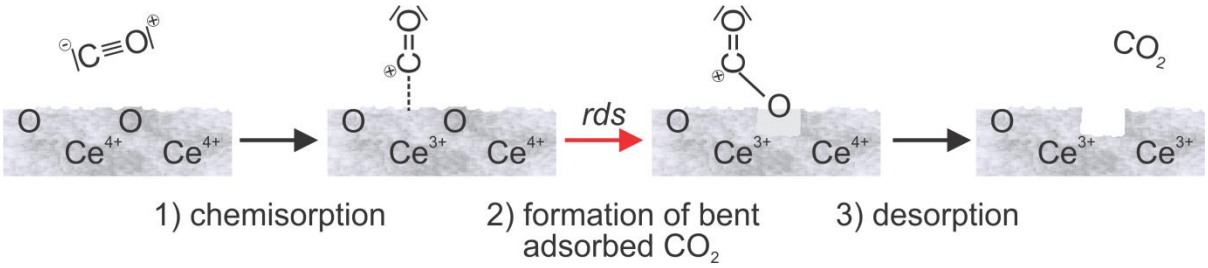

Figure 65: Reaction mechanism for CO oxidation for doped ceria, which is in accordance to the present experimental data and the literature findings mentioned in the main text.

The reaction step **1**, where CO chemisorbs at the surface by donating e' to the catalyst (reducing Ce^{4+} to Ce^{3+}) represents a fast preceding equilibrium. Since the replenishment of lattice oxygen by O_2 is not rate-determining and no dependence of R_{CO} on $[V_O^{\bullet\bullet}]$ was observed, and in line with the literature observations that the extraction of O_O^x is involved in the rate-determining step[133], elementary-step **2** represents an appropriate candidate as *rds*. Here, the adsorbed CO^+ species reacts with O_O^x to form the transition sate $\{CO_{ad}^+ - O_O^x\}$ where the oxygen is largely pulled out from the surface[142]. In step **3**, CO_2 desorbs from the surface by forming an oxygen vacancy and reduction of the second Ce. The expression for the rate–determining step yields:

$$R_{rds} = \vec{k}_2[CO^+][O_O^x] \qquad \text{eq. 51}$$

For the adsorption pre-equilibrium in step **1** one can formulate eq. 52:

$$K_1 = \frac{[CO^+][e']}{p(CO)} \qquad \text{eq. 52}$$

Inserting eq. 52 into eq. 51 yields for the *rds* the following relationship:

$$R_{\mathrm{rds}} = \vec{k}_2 p(\mathrm{CO})[\mathrm{O}_\mathrm{O}^\mathrm{x}][e']^{-1} \qquad \text{eq. 53}$$

Since the reduction of the catalyst by CO causes the formation of e', the electron concentration should increases with $p(\mathrm{CO})$. Hence, one can assign that $[e'] \propto p(\mathrm{CO})^m$ with $m > 0$. This also explains the observed $p(\mathrm{CO})$ with $R_{\mathrm{CO}} \propto p(\mathrm{CO})^{\sim 0.65}$, and the $p(\mathrm{O}_2)$ independence of R_{CO}. With this, eq. 53 turns into:

$$R_{\mathrm{CO}} \approx R_{\mathrm{rds}} = \vec{k}_2 p(\mathrm{CO})^{1-m}\,[\mathrm{O}_\mathrm{O}^\mathrm{x}] \qquad \text{eq. 54}$$

4.3.3.3 Conclusion

In conclusion, investigation of the CO oxidation kinetics on systematically Pr, Gd, Nb–doped ceria, Pr–doped zirconia, Fe–doped strontium titanate and YSZ revealed that the redox-activity (reducibility) is crucial for good CO oxidation performance. The absence of additional oxygen vacancies did not strongly decelerate the kinetics. Doping of an already redox-active metal oxide with a metal cation showing lower reduction enthalpies does not accelerate the CO oxidation, at least in ceria. A kinetically determined decreased effective oxygen partial pressure prevails inside the catalyst particles; the catalyst develops an increased steady–state oxygen non-stoichiometry (it is more reduced). This effect is stronger with decreasing dopant concentration. The induced increased oxygen non-stoichiometry accelerates the oxygen incorporation reaction until the CO oxidation and O incorporation reactions are balanced. From partial pressure and dopant concentration dependent measurements of the reaction rate, it is concluded that the rate–determining step of the CO oxidation involves the reaction of adsorbed CO^+ with surface lattice oxygen followed by a fast CO_2 desorption and oxygen vacancy formation.

4.3.4 Methane Oxidation

4.3.4.1 Results and Discussion

The conversion of methane is plotted in figure 66a as a function of reactor temperature in an atmosphere of 1 % O_2 and 0.25 % CH_4 (oxidizing conditions even for complete conversion) for PDC, GDC, 2NDC and YSZ.

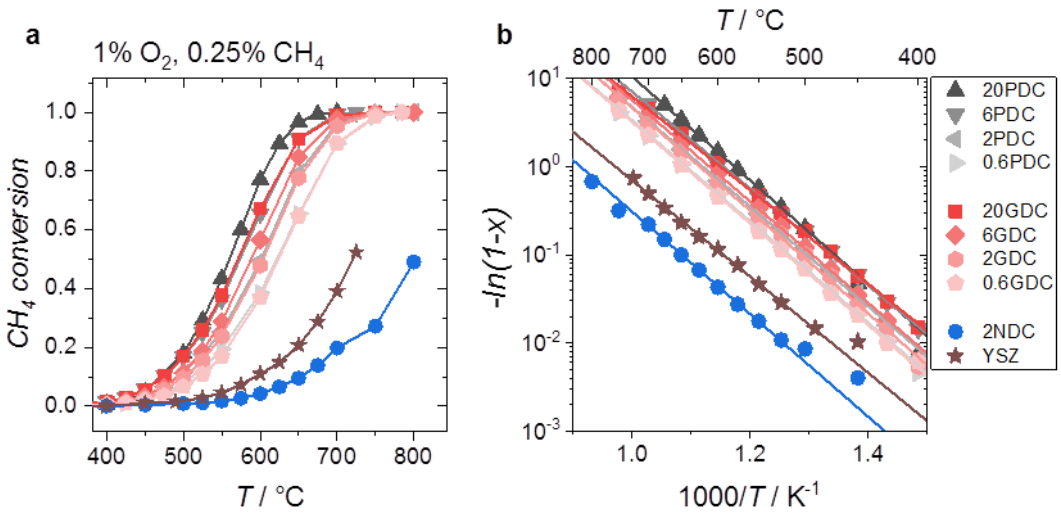

Figure 66: a) CH_4 conversion and b) Arrhenius plot for Pr–, Gd–, and Nb–doped ceria and 14 mol% Y stabilized zirconia (YSZ) powder samples.

No formation of CO was observed. All samples follow a temperature dependence of Arrhenius type (figure 66b). The apparent activation energy was found to be in the range of 1.05–1.16 eV. Methane oxidation proceeds in all cases at higher temperatures compared to CO oxidation. The onset temperature for CH_4 conversion of the series of Pr doped ceria (black symbols) shifts slightly to higher temperatures with decreasing Pr concentration. The reaction starts at around 450 °C and reaches full conversion at around 700 °C.

The samples of Gd–doped ceria (red symbols) behave similarly, but tend to be slightly less active compared to PDC. On 2NDC (blue), the on-set temperature for CH_4 conversion is shifted to higher temperatures, the reaction commenced at around 600 °C and full conversion is attained probably beyond 900 °C. For YSZ, which has no intrinsic redox behavior, the CH_4 conversion starts at 550 °C and reaches full conversion probably beyond 800 °C.

The activation energy for the samples are summarized in figure 67a, they are in a comparable range of 1.1 eV ±0.06 eV. The apparent reaction rates R_{CH_4} (see eq. 9) at low conversion (< 20 %) were calculated by normalizing to the surface area of the samples, and the apparent reaction rates were inter/extrapolated to a common temperature of 475 °C in figure 67b to compare the reactivity.

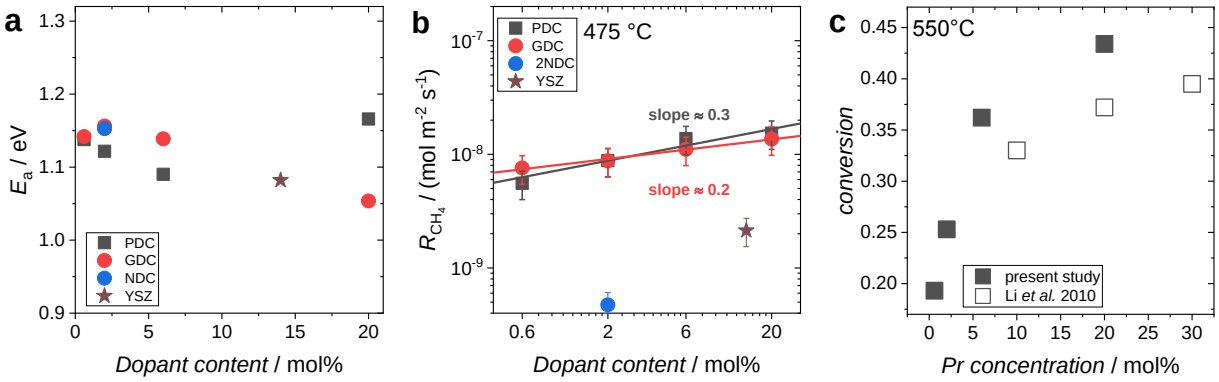

Figure 67: a) Dopant dependence of the activation energy of CH_4 oxidation. b) Dopant dependence of the apparent reaction rate R_{CH_4}. c) Conversion of CH_4 for PDC at 550 °C. Filled symbols: present study; open symbols: Literature data taken from Li *et al.*[143].

The reactivities of CH_4 oxidation are very similar for PDC and GDC. This is in line with data from Wiles *et al.*[93], they measured similar CH_4 oxidation rates for 20PDC and 20GDC. Only a small dopant dependence of R_{CH_4} was observed. For PDC, the rate R_{CH_4} is proportional to $[Pr]^{0.3}$, and for GDC a slightly lower dependence was measured with $R_{CH_4} \propto [Gd]^{0.2}$. The measured conversions of PDC are also in line with experimental results from Li *et al.*[143], the conversion shows a similar dependence to the Pr concentration at high [Pr] (see figure 67c).

It seems that Pr and Gd affect the CH_4 oxidation reaction similarly and that the better redox-performance of PDC hardly influences the reaction. The reaction rate for 2NDC is one order of magnitude smaller which might be related to the absence of any oxygen vacancy at the surface and/or to the less easy reducibility due to the n-type character of 2NDC. Ramírez-Cabrera and coworkers[144] found for Gd– and Nb–doped ceria, that Nb doping decreases the reaction rate for CH_4 oxidation. They attributed this deceleration to Nb segregation to the surface.

The redox-inactive YSZ shows a moderately higher reaction rate than 2NDC, but it is still one order of magnitude smaller compared to 20PDC emphasizing the importance of redox properties/electronic defects of the catalyst.

Methane and oxygen partial pressure dependences of the apparent reaction rates R_{CH_4} were measured only for 2 and 20PDC/GDC, *cf.* figure 68. R_{CH_4} is proportional to $p(CH_4)$ as $R_{CH_4} \propto p(CH_4)^{\sim 0.75}$. Only a weak $p(O_2)$ dependence was found with $R_{CH_4} \propto p(O_2)^{\sim 0.2}$. Similar reaction orders have been found by Wilkes *et al.* for La doped ceria where $R_{CH_4} \propto p(O_2)^{\sim 0.2}$ and $R_{CH_4} \propto p(CH_4)^{\sim 0.75}$ but the origin of these dependences remains unexplained in ref.[93].

Figure 69a shows that the rate for CH_4 oxidation R_{CH_4} for 2PDC is two orders of magnitude slower compared with the rate of CO oxidation R_{CO}, and about one order

of magnitude smaller compared with the oxygen exchange rate $\Re_0$. Hence, in contrast to CO oxidation no change of the oxygen non-stoichiometry is expected.

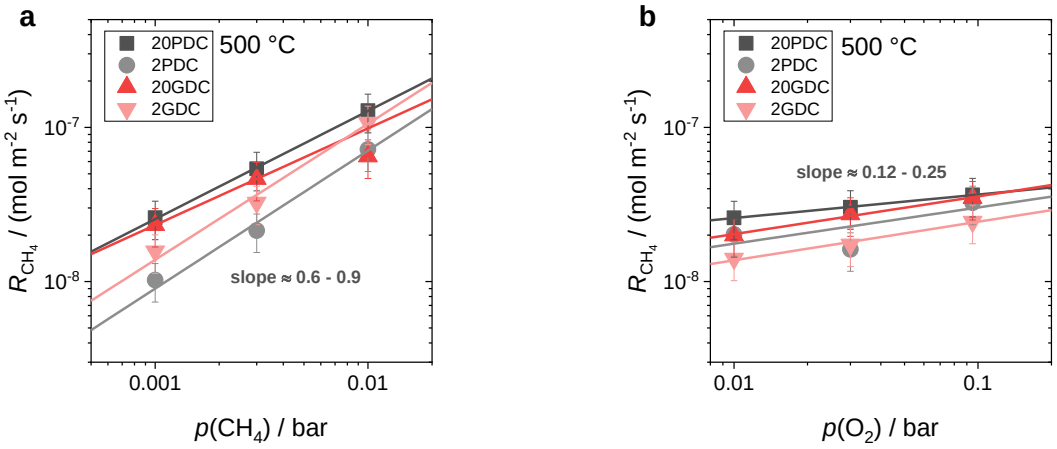

Figure 68: Dependence of the CH_4 oxidation reaction rate R_{CH_4} on a) CH_4 partial pressure, and b) oxygen partial pressure.

This was confirmed by thermogravimetric *in situ* CH_4 oxidation (*cf.* figure 69b). No mass deviation was found for 2PDC when comparing the behavior in O_2 and CH_4/O_2, the sample particles do not show a decreased oxygen stoichiometry while exposed to CH_4/O_2. Since this holds already for the relative weak doped 2PDC sample, it is reasonable to assume here that also inside the other doped ceria samples no kinetically determined effective $p(O_2)_{eff}$ is present.

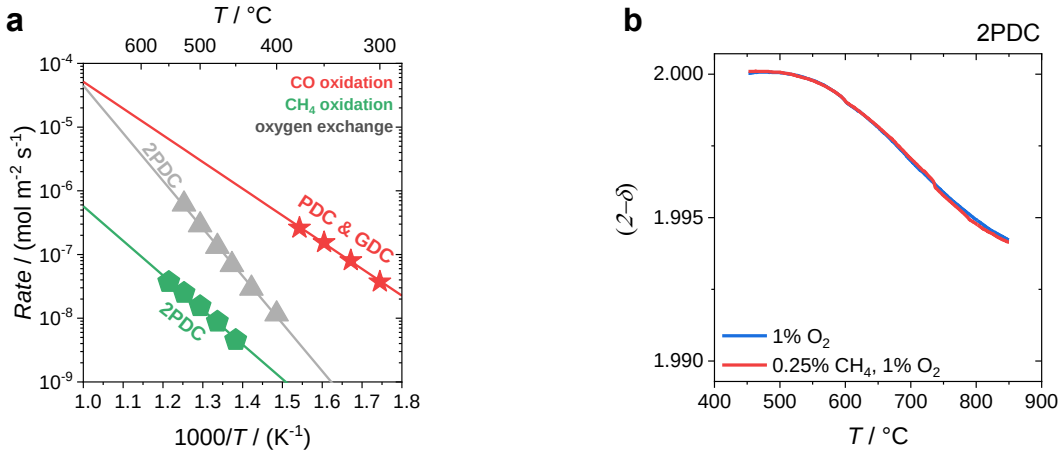

Figure 69: a) Plot of the apparent reaction rates R_{CO}/R_{CH_4} of CO/CH_4 oxidation of PDC powder samples and the equilibrium exchange rate $\Re_0$ of oxygen incorporation. (since PDC and GDC behave similar, the red colored data is also representative for GDC). b) Temperature dependent oxygen non-stoichiometry of 2PDC powder samples exposed to 1 % O_2 (blue) and 1 % O_2 plus 0.25 % CH_4 (red).

Similar to CO, CH_4 oxidation is suggested to proceed via the Mars-van-Krevelen mechanism (MvKM)[145, 146] where ceria is reduced by methane (formation of surface oxygen vacancies) and re-oxidized by oxygen.

CH_4 interacts only weakly with the surface[145]. The C-H bonds in methane are very stable (band energy 440 kJ/mol) and hence, the rate-determining step is the

abstraction of the first hydrogen atom by lattice oxygen[145, 147]. The fact that this C-H bond breaking is rather difficult also explains the general trend of lower reaction rates for CH_4 oxidation compared to CO. On stoichiometric ceria, DFT calculations indicate that the subsequent release of a methyl radical after the first H bond cleavage shows a moderate energy barrier of 1.44 eV and decreases with increasing dehydrogenation[145]. The adsorption of CH_x close to surface oxygen vacancies is less favorable than at lattice oxygen and Ce cations[148]. The importance of oxygen vacancies in the CH_4 oxidation only comes into play when the bulk oxygen non-stoichiometry is very large with $\delta > 0.15$[149], which is not the case in the present study. Hence, oxygen vacancies seem not to be involved in the rate–determining step. Using DFT, Salcedo *et al.* found that the energy barrier of the first cleavage of the hydrogen bond is reduced by 0.45 eV in case of 3.7 mol% Pr–doped ceria (111) surfaces compared to undoped ceria. Since Pr(4f) states are located at lower energies than Ce(4f), the electron transfer to Pr from the hydrogen that bonds to lattice oxygen is facilitated.[147] Identical partial pressure and dopant dependence for both materials indicate that the availability of Pr(4f) states do not strongly accelerates CH_4 oxidation. The reason why identical rates for PDC and GDC were obtained in the present study (and in literature) may originate from non-ideal behavior at higher Gd concentrations.

In the following, the measured dependence of R_{CH_4} to O_2 and CH_4 partial pressure and dopant concentration are interpreted semi-quantitatively by assuming a fast surface adsorption of CH_4 as pre-equilibrium, followed by the rate-determining step:

$$CH_{4\,ad} + O_O^x + h^\bullet \overset{\vec{k}}{\rightarrow} {}^\bullet CH_3 + OH_O^\bullet \qquad \text{eq. 55}$$

Here, the first hydrogen is abstracted by lattice oxygen and consumption of electron holes. The methyl radical ${}^\bullet CH_3$ is released to the gas phase and is not absorbed. The formation of the gas phase ${}^\bullet CH_3$ is energetically favorable as found by DFT calculations[145]. Considering fast adsorption, one can write for the rate of the limiting reaction step ($\vec{k}^*$ contains the rate of the *rds* and the adsorption equilibrium):

$$R_{CH_4} \approx R_{rds} = \vec{k}^* p(CH_4)[O_O^x][h^\bullet] \qquad \text{eq. 56}$$

The hole concentration is a function of $p(O_2)$ and dopant type and concentration. For the overall oxygen incorporation reaction the relationship $[h^\bullet] \propto p(O_2)^{0.25} \propto [V_O^{\bullet\bullet}]^{0.5}$ holds. Inserting the $p(O_2)$ dependence of $h^\bullet$ into eq. 56 yields $R_{CH_4} \propto p(O_2)^{0.25}$,

which is in good agreement to the measured dependence of $R_{CH_4} \propto p(O_2)^{\sim 0.2}$. On the other hand, doping with Gd and Pr increases the amount of oxygen vacancies. The condition $[h^\bullet] \propto [V_O^{\bullet\bullet}]^{0.5}$ than converts into $[h^\bullet] \propto [Gd]^{0.5}$, or to a good approximation for Pr into $[h^\bullet] \propto [Pr]_{tot}^{0.5}$. According to eq. 56, the dependence of the reaction rate on the dopant concentration yields $R_{CH_4} \propto [Gd]^{0.5}$ and $R_{CH_4} \propto [Pr]_{tot}^{0.5}$, which is close to the observed dependence of $R_{CH_4} \propto [Gd]^{0.2} \propto [Pr]_{tot}^{0.3}$. From eq. 56, R_{CH_4} is proportional to $p(CH_4)^1$, which is also close to the measured dependence of $R_{CH_4} \propto p(CH_4)^{\sim 0.75}$. Since no $p(O_2)_{eff}$ was found for 2PDC and is not assumed to be present in the doped ceria samples, the lower exponent of 0.75 cannot be explained by $h^\bullet$ annihilation as it was the case for CO oxidation. A reasonable hypothesis for this could be that due to the formation of H_2O, a higher concentration of surface hydroxides at higher methane concentration partially blocks the adsorption sites for CH_4.

4.3.4.2 Conclusion

Doped ceria is less active for methane oxidation compared to CO oxidation and oxygen incorporation. For GDC and PDC the CH_4 oxidation kinetics depends moderately on the dopant concentration and no significant difference between Gd– and Pr–doping was found. This indicates that the easy reducibility of Pr does not further promote CH_4 oxidation. Instead, electron holes produced by Gd and Pr doping (in case of Pr, electron holes are in equilibrium with the redox reaction) appear in *or* before the rate–determining step, which is the cleavage of the first C-H bond. In contrast to CO oxidation, inside the catalyst particles no decreased effective oxygen partial pressure develops, which is attributed to the lower methane oxidation rate compared to the rate of oxygen incorporation.

4.4 Propan-2-ol dehydration/dehydrogenation

According to the reaction scheme in r. 15, propan–2–ol can react to propene or propanone. The dehydration of propan-2-ol to propene occurs if the surface of the sample shows either acid sites or both acid and base sites. On the other hand, the formation of propanone proceeds if the surface shows base or redox–active properties.[150, 151] The formation of diisopropyl ether is not considered here, since it was not observed during the reactions. So far, no study on systematically doped ceria is available, which investigates the dehydration/dehydrogenation of propan–2–ol on the surface.

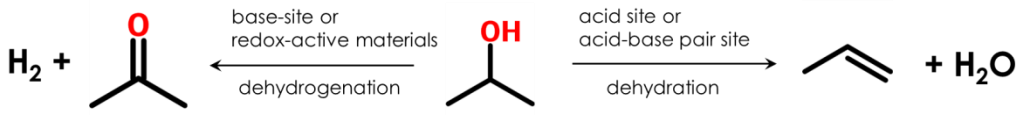

r. 15

For the dehydration of propan–2–ol to propene the reaction mechanism follows an elimination reaction according to an E1, E2, or E1cB mechanism, where the rupture of the C–H bound is most likely part of the rate–determining step[152, 153]. On a series of metal oxides with different types of active centers, it was observed that in case of a predominant Lewis acidity the strength of the present basic centers determines the rate of propene formation.[154]

For dehydrogenation, the rate–determining step is also assumed to be the cleavage of the C–H bond (which, however, there is part of a redox reaction).[155] In ref.[156] it was deduced from *in situ* IR measurements that the rate of dehydrogenation to propanone is controlled by the electronic mobility at the surface of ceria.

The selectivity of these reactions is often used to characterize the acid–base and redox–properties of a catalyst. But unambiguous interpretations are challenging since the dehydrogenation and dehydration can proceed over various active sites and different parallel reactions can occur. Furthermore, the reaction is not only influenced by the concentrations of the active sites but also on the strength and type (*e.g.* Lewis *vs.* Brønsted acid).[154]

In figure 70a and b, the conversion of propan–2–ol and the Arrhenius diagram for undoped ceria, 20GDC, 20PDC and 2NDC are plotted as a function of reactor temperature. The used catalyst masses (1.00 g), BET areas (0.014 m^2 g^-) and bed heights (≈ 5 mm) of the samples are identical. SEM images of the particles' surface are given in figure 25

At T > 350 °C, the conversion differs between the samples. At 400 °C, undoped ceria shows the lowest conversion of approximately 5 % and Pr–, and Gd–doped

ceria exhibit values of 10 – 12 %, and Nb–doped ceria shows the highest conversion of 22 %. The activation energy is small with 0.3 eV for undoped ceria and increases according to 20GDC < 20PDC < 2NDC.

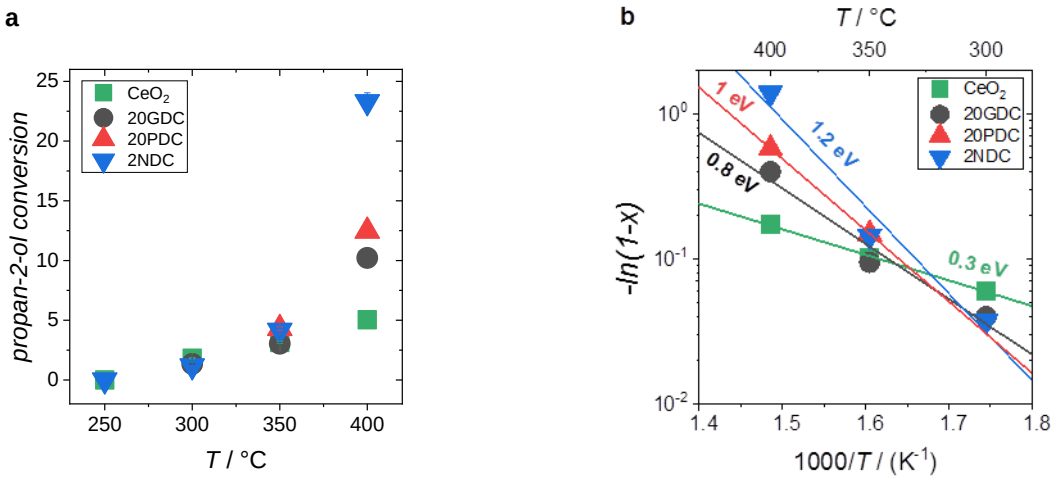

Figure 70: a) Propan-2-ol conversion, b) Arrhenius diagram calculated from propan-2-ol conversion. Note that the activation energy for 20PDC was extracted from only two data points.

Only on 20GDC, carbon deposition was observed. The amount of carbon was determined by TG in O_2 leading to CO_2 formation, which was monitored by MS. (using CO_2 formation from $CaCO_3$ as a reference). It was found that 0.31 mg carbon haven been deposited within 16 h of measurement on 20GDC particles, which is approx. a 15 fold monolayer of C (estimated adsorption cross–section ≈ 5 Å²).

The relative fractions of propane and propanone exiting the reactor for Pr–, Gd–doped ceria as well undoped ceria are plotted in figure 71. The formation of propene on GDC and PDC is significantly lower in comparison to Nb–doped ceria. Regarding the selectivity of propanone formation, the opposite trend was observed for NDC.

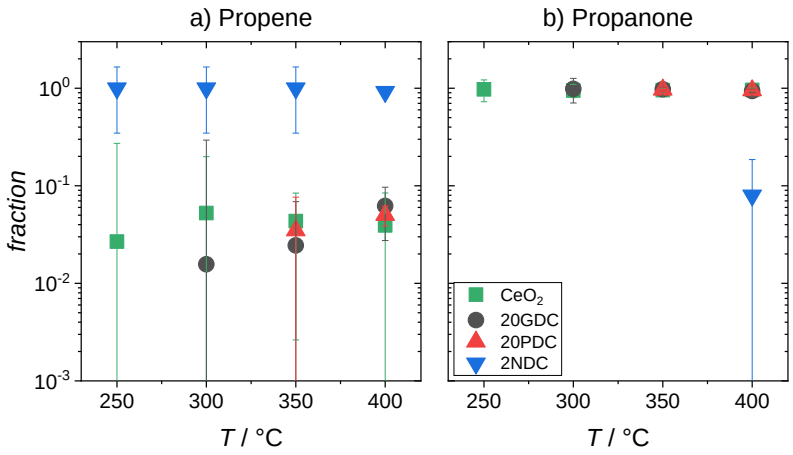

Figure 71: Relative fraction of a) propene and b) propanone as a function of reactor temperature for undoped ceria, 20GDC, 20PDC and 2NDC.

In ref.[157] it was suggested that acid–base properties (Brønsted or Lewis type) can be investigated when the reaction proceeds in an inert gas atmosphere and

redox–properties when oxygen is present. Since the experiment in the present work was conducted in N_2 atmosphere, it is considered that just acid and base centers are involved in the decomposition of propan–2–ol, but no distinction can be made about the nature of the active sites (Brønsted or Lewis).

The results in figure 70 and figure 71 suggest that undoped, Pr–, and Gd–doped ceria have predominantly basic surface properties since the reaction is selective for propanone formation. From defect chemical consideration, it is expected that those samples show a high concentration of surface oxygen vacancies, which represent acid centers. Therefore, it could be that propan–2–ol does not adsorb into an oxygen vacancy, but rather on a Ce cation and surface oxide ions that act as basic sites abstracting protons. On the other hand, 2NDC ceria seems to show predominantly surface acidity or acid–base properties. Under reducing conditions electronic compensation is expected $[Nb_{Ce}^{\bullet}] = [e'](Ce_{Ce}')$. Thus, the basicity should be increased, which apparently contradicts the results. The authors in ref.[156] stated that the rate of dehydrogenation to propanone decreased with decreasing electronic mobility at the surface of ceria. Therefore, on the present NDC sample other influences seem to cause the higher selective towards propene formation.

A profound explanation of the observed results in this work with respect to defect chemistry is not possible so far. Additional investigations such as *in situ* IR measurements, which could probe the preferred adsorption site of propan–2–ol on samples with different defect–chemical regimes might be necessary.

5 SUMMARY AND MAIN CONCLUSIONS

The scope of this work was to elucidate the influences of ionic and electronic point defects on the catalytic activity of oxides. The first reaction investigated is the oxygen exchange kinetics on an extended set of about 20 systematically doped ceria samples. This was subsequently complemented by more complex test reactions such as carbon monoxide and methane oxidation.

For oxygen exchange kinetics, a setup for pulsed $^{16}O/^{18}O$ isotope exchange was established and optimized. This setup allows for a comparably fast screening and thus systematic investigation of the dependence of oxygen exchange kinetics on point defects, which are modified by doping. Carbon monoxide and methane oxidation were studied in fixed bed reactors in the same experimental setup. Since the catalytic activity of an oxide is extremely sensitive to the exact surface conditions (not only surface point defects, but also potentially contaminating or accelerating unintended impurities) it was important to establish a consistent data set from samples prepared and measured under the same experimental conditions as the basis for further conclusions.

Bulk point defect concentrations can be tuned by homogeneous chemical doping. The concentrations of surface defects that are decisive for the catalytic activity are closely coupled to the bulk concentrations. Doping of ceria with Gd^{3+} leads to oxygen vacancy formation, Pr doping creates oxygen vacancies $V_O^{\bullet\bullet}$ and additional capability of valance change ($Pr^{3+/4+}$) influencing the redox-activity, and substitution of Ce^{4+} by Nb^{5+} causes the formation of conduction electrons and/or oxygen interstitials. Surface sensitive H_2O and CO_2 sorption experiments show that the amount of adsorbed molecules correlates similarly with surface oxygen vacancy concentration in both GDC and PDC. In contrast, CO_2 and H_2O adsorption is not favorable on NDC. Regarding electronic defects (redox-active centers), UV-Vis spectroscopy indicates the formation of a Pr impurity band in Pr–doped ceria and zirconia at high Pr concentration.

From the dependence of the equilibrium oxygen exchange rate $\Re_0$ on oxygen partial pressure $p(O_2)$ and dopant type and concentration, important conclusions on the rate-determining step (*rds*) could be derived. The $p(O_2)$ dependence was found to be $\Re_0 \propto p(O_2)^{>0.5}$ in all cases. The fact that the exponent of the overall $p(O_2)$ dependence is between 0.5 and 1 indicates that molecular oxygen species are involved in the *rds*, and at least one electron is consumed ore one hole is produced before *or* in the *rds*. The equilibrium oxygen exchange rate $\Re_0$ on GDC shows a proportionality of $\Re_0 \propto [Gd]^1 \propto [V_O^{\bullet\bullet}]^1$. For PDC, where approximately also

$[V_O^{\bullet\bullet}] \propto [Pr]$ holds, an even stronger increase of $\Re_0 \propto [Pr]^{3.5}$ was found. This indicates that in Gd/Pr single and double doped ceria oxygen vacancies are involved in *or* before the *rds*. Together with the $p(O_2)$ dependence the conclusion is that on GDC and most likely on PDC either the encounter of adsorbed O_2^- and $V_O^{\bullet\bullet}$, the subsequent incorporation of O_2^- into $V_O^{\bullet\bullet}$, or the vacancy assisted dissociation of molecular oxygen species is rate-limiting.

The highest oxygen exchange reaction rates were found when oxygen vacancies as well as redox-active centers are available. The presence of redox-active cations such as Pr or Tb drastically increases the rate of oxygen incorporation significantly compared to pure donor or acceptor dopants. At 700 °C, 20PDC increases $\Re_0$ by almost five orders of magnitude relative to undoped ceria. This steep increase of $\Re_0$ for PDC was related to the formation of an impurity band facilitating charge transfer to adsorbed oxygen species. Interestingly, oxygen bulk diffusivity is also facilitated in Pr–doped ceria, which is tentatively attributed to a decreased oxygen migration barrier along Pr^{3+}/Pr^{4+} sites.

CO and methane oxidation using doped ceria samples and related materials as catalyst follow a Mars-van-Krevelen mechanism, in which CO or CH_4 is oxidized using lattice oxygen of the catalyst, and the reduced catalyst is subsequently re-oxidized by O_2. If the latter is the *rds* of the overall reaction, similar trends as for oxygen exchange are expected. The Mars-van-Krevelen mechanism is confirmed by the observation that no $C^{18}O^{16}O$ was observed during CO oxidation in ^{18}O enriched gas atmosphere.

The CO oxidation rate R_{CO} is similar for undoped ceria, PDC, and GDC (also for different Gd and Pr concentrations), but decreased for NDC. The fact that the reaction order for CO is between 0.6 and 0.9, but almost independent of $p(O_2)$, indicates that the reduction of the catalyst by CO is the *rds*, not the re-oxidation. The depletion of the reaction rate for NDC might be related to the suppression of surface oxygen vacancies, and/or to the less easy reducibility due to its n-type character. The importance of redox properties and electronic defects of the catalyst shows up for related materials which exhibit more pronounced dependences on the reducibility of the material ($R_{CO} \propto [Pr]^{1.3}$ in Pr-doped zirconia, and $R_{CO} \propto [Fe]^{0.2 \text{ to } 2.3}$ in $SrTi_{1-x}Fe_xO_{3-\delta}$). From the present experimental observations it was concluded that the rate–determining step of CO oxidation involves the reaction of adsorbed CO^+ with surface lattice oxygen forming a transition state of $\{CO^+_{ad}-O^x_O\}$, where O^x_O is partially pulled out of the lattice. This is followed by fast CO_2 desorption (oxygen vacancy formation) and also fast re-oxidation.

The CO oxidation rate R_{CO} of GDC, PDC and NDC is higher compared to the equilibrium oxygen exchange rate $\Re_0$. The surface oxygen depletion together with fast bulk diffusion induces a kinetically determined decreased effective $p(O_2)_{eff}$ within the catalyst's interior, which accelerates $\Re_0$ until both rates – R_{CO} and $\Re_0$ – are equal in the steady state. With increasing T, $\Re_0$ increases more steeply until $R_{CO} = \Re_0$ and $p(O_2)_{eff} = p(O_2)$. This self-balanced process is the reason why O_2 incorporation is not the *rds* under steady state conditions, at least in doped ceria.

The reaction rate of methane oxidation R_{CH_4} for PDC and GDC is about three orders of magnitude smaller compared to R_{CO}. The dependence on Gd, Pr, and Nb dopant concentration is similar to CO oxidation. Also the partial pressure dependencies are similar, with $R_{CH_4} \propto p(CH_4)^{\sim 0.75}$ and $R_{CH_4} \propto p(O_2)^{\sim 0.2}$ for PDC and GDC. These dependencies were explained by assuming that the rate-determining step is the cleavage of the first C–H bond such that the hydrogen is abstracted by lattice oxygen and electron holes are consumed. Since in the investigated temperature range, R_{CH_4} is always smaller than $\Re_0$, no appearance of a decreased kinetically determined effective $p(O_2)_{eff}$ is expected, which was confirmed thermogravimetrically for 2PDC.

Overall, it can be concluded that doping strongly affects the catalytic activity and that ionic and electronic point defects affect the gas-solid reaction kinetics in doped–ceria differently.

The reaction rates of O_2 exchange can be modified by orders of magnitude upon doping. The combination of ionic defects ($V_O^{\bullet\bullet}$) and electronic defects achieved by doping with, *e.g.,* a mixed-valent cation such as $Pr^{3+/4+}$ had the strongest effect. Oxygen exchange was increased by almost a factor 100000 compared with undoped ceria.

CO and CH_4 are less sensitive to dopant concentrations in ceria because within the Mars-van-Krevelen mechanism rather the CO and CH_4 oxidation than the O incorporation into the formed oxygen vacancy is limiting. However, the kinetically determined decreased $p(O_2)_{eff}$ for CO oxidation on PDC depends strongly on the oxygen exchange rate and thus the Pr dopant concentration.

REFERENCES

[1] J. Maier, *Chem. Eur. J.* **2001**, *7*, 4762.
[2] G. Simkovich, C. Wagner, *J. Catal.* **1962**, *1*, 521.
[3] P. Unnikrishnan, D. Srinivas, in *Industrial Catalytic Processes for Fine and Specialty Chemicals* Eds.: S. S. Joshi, V. V. Ranade), Elsevier, Amsterdam, **2016**, p. 41.
[4] P. L. Gai-Boyes, *Catalysis Reviews* **1992**, *34*, 1.
[5] M. Vračar, Dissertation, University of Stuttgart, Stuttgart, Germany, **2008**.
[6] R. Merkle, J. Maier, *Top. Catal.* **2006**, *38*, 141.
[7] H. Inaba, H. Tagawa, *Solid State Ion.* **1996**, *83*, 1.
[8] M. Melchionna, P. Fornasiero, *Mater. Today* **2014**, *17*, 349.
[9] T. Montini, M. Melchionna, M. Monai, P. Fornasiero, *Chem. Rev.* **2016**, *116*, 5987.
[10] R. J. Gorte, *AlChE J.* **2010**, *56*, 1126.
[11] J. A. Rodriguez, D. C. Grinter, Z. Liu, R. M. Palomino, S. D. Senanayake, *Chem. Soc. Rev.* **2017**, *46*, 1824.
[12] Q. Wang, K. L. Yeung, M. A. Bañares, *Catal. Today* **2019**
[13] R. Merkle, J. Maier, *Angew. Chem. Int. Ed.* **2008**, *47*, 3874.
[14] S. R. Bishop, T. S. Stefanik, H. L. Tuller, *J. Mater. Res.* **2012**, *27*, 2009.
[15] S. R. Bishop, T. S. Stefanik, H. L. Tuller, *Phys. Chem. Chem. Phys.* **2011**, *13*, 10165.
[16] T. S. Stefanik, H. L. Tuller, *J Electroceram* **2004**, *13*, 799.
[17] C. Chatzichristodoulou, P. V. Hendriksen, *J. Electrochem. Soc.* **2010**, *157*, B481.
[18] S. R. Bishop, K. L. Duncan, E. D. Wachsman, *Electrochim. Acta* **2009**, *54*, 1436.
[19] S. Wang, H. Inaba, H. Tagawa, T. Hashimoto, *J. Electrochem. Soc.* **1997**, *144*, 4076.
[20] D. Schneider, M. Godickemeier, L. J. Gauckler, *J Electroceram* **1997**, *1*, 165.
[21] M. Mogensen, N. M. Sammes, G. A. Tompsett, *Solid State Ion.* **2000**, *129*, 63.
[22] I. K. Naik, T. Y. Tien, *J. Electrochem. Soc.* **1979**, *126*, 562.
[23] K. Yashiro, T. Suzuki, A. Kaimai, H. Matsumoto, Y. Nigara, T. Kawada, J. Mizusaki, J. Sfeir, J. Van herle, *Solid State Ion.* **2004**, *175*, 341.
[24] C. Balaji Gopal, M. García-Melchor, S. C. Lee, Y. Shi, A. Shavorskiy, M. Monti, Z. Guan, R. Sinclair, H. Bluhm, A. Vojvodic, W. C. Chueh, *Nat. Commun.* **2017**, *8*, 15360.
[25] W. C. Chueh, A. H. McDaniel, M. E. Grass, Y. Hao, N. Jabeen, Z. Liu, S. M. Haile, K. F. McCarty, H. Bluhm, F. El Gabaly, *Chem. Mater.* **2012**, *24*, 1876.
[26] C. B. Gopal, F. E. Gabaly, A. H. McDaniel, W. C. Chueh, *Adv. Mater.* **2016**, *28*, 4692.
[27] Q. Lu, G. Vardar, M. Jansen, S. R. Bishop, I. Waluyo, H. L. Tuller, B. Yildiz, *Chem. Mater.* **2018**, *30*, 2600.
[28] I. Riess, H. Janczikowski, J. Nölting, *J. Appl. Phys.* **1987**, *61*, 4931.
[29] F. A. Kröger, H. J. Vink, in *Solid State Physics, Vol. 3* Eds.: F. Seitz, D. Turnbull), Academic Press, **1956**, p. 307.
[30] H. L. Tuller, A. S. Nowick, *J. Phys. Chem. Solids* **1977**, *38*, 859.
[31] G. Zhou, P. R. Shah, T. Montini, P. Fornasiero, R. J. Gorte, *Surf. Sci.* **2007**, *601*, 2512.
[32] C. Chatzichristodoulou, P. V. Hendriksen, A. Hagen, *J. Electrochem. Soc.* **2010**, *157*, B299.
[33] P. Shuk, M. Greenblatt, *Solid State Ion.* **1999**, *116*, 217.
[34] I. Navarro, F. Marques, J. Frade, *J. Electrochem. Soc.* **1997**, *144*, 267.

[35] C. Chatzichristodoulou, P. V. Hendriksen, *Phys. Chem. Chem. Phys.* **2011**, *13*, 21558.
[36] S. Lübke, H. D. Wiemhöfer, *Solid State Ion.* **1999**, *117*, 229.
[37] H. L. Tuller, S. J. Litzelman, W. Jung, *Phys. Chem. Chem. Phys.* **2009**, *11*, 3023.
[38] S. Kim, J. Maier, *J. Electrochem. Soc.* **2002**, *149*, J73.
[39] G. Gregori, R. Merkle, J. Maier, *Prog. Mater Sci.* **2017**, *89*, 252.
[40] M. C. Göbel, G. Gregori, J. Maier, *Phys. Chem. Chem. Phys.* **2014**, *16*, 10175.
[41] D. S. D. Gunn, J. A. Purton, S. Metz, *Solid State Ion.* **2018**, *324*, 128.
[42] M. A. Frechero, M. Rocci, G. Sanchez-Santolino, A. Kumar, J. Salafranca, R. Schmidt, M. R. Diaz-Guillen, O. J. Dura, A. Rivera-Calzada, R. Mishra, S. Jesse, S. T. Pantelides, S. V. Kalinin, M. Varela, S. J. Pennycook, J. Santamaria, C. Leon, *Sci. Rep.* **2015**, *5*, 9.
[43] Z. A. Feng, F. El Gabaly, X. Ye, Z.-X. Shen, W. C. Chueh, *Nat Commun* **2014**, *5*
[44] M. Nolan, J. E. Fearon, G. W. Watson, *Solid State Ion.* **2006**, *177*, 3069.
[45] A. F. Zurhelle, X. R. Tong, A. Klein, D. S. Mebane, R. A. De Souza, *Angew. Chem. Int. Ed.* **2017**, *56*, 14516.
[46] I. Denk, J. Claus, J. Maier, *J. Electrochem. Soc.* **1997**, *144*, 3526.
[47] M. Nolan, S. Grigoleit, D. C. Sayle, S. C. Parker, G. W. Watson, *Surf. Sci.* **2005**, *576*, 217.
[48] L. Yan, K. R. Balasubramaniam, S. Wang, H. Du, P. A. Salvador, *Solid State Ion.* **2011**, *194*, 9.
[49] L. Zhang, S. Wang, H. Huang, Y. Li, Y. Lu, C. Xia, *J. Electrochem. Soc.* **2017**, *164*, F610.
[50] M. Baerns, A. Behr, H. Hofmann, U. Onken, A. Renken, *Technische Chemie,* WILEY-VCH, Weinhaim, **2008**.
[51] J. Maier, *Solid State Ion.* **1998**, *112*, 197.
[52] J. Maier, *Solid State Ion.* **2000**, *135*, 575.
[53] C.-Y. Yoo, B. A. Boukamp, H. J. M. Bouwmeester, *J. Solid State Electrochem.* **2011**, *15*, 231.
[54] C.-Y. Yoo, Universiteit Twente, Twente, The Netherlands, **2012**.
[55] C.-Y. Yoo, H. J. M. Bouwmeester, *Phys. Chem. Chem. Phys.* **2012**, *14*, 11759.
[56] H. J. M. Bouwmeester, C. Song, J. Zhu, J. Yi, M. v. S. Annaland, B. A. Boukamp, *Phys. Chem. Chem. Phys.* **2009**, *11*, 9640.
[57] C. Yang, X. Yu, S. Heißler, P. G. Weidler, A. Nefedov, Y. Wang, C. Wöll, T. Kropp, J. Paier, J. Sauer, *Angew. Chem. Int. Ed.* **2017**, *56*, 16399.
[58] R. Merkle, J. Maier, H. J. M. Bouwmeester, *Angew. Chem. Int. Ed.* **2004**, *43*, 5069.
[59] A. V. Berenov, A. Atkinson, J. A. Kilner, E. Bucher, W. Sitte, *Solid State Ion.* **2010**, *181*, 819.
[60] A. Schmid, G. M. Rupp, J. Fleig, *Chem. Mater.* **2018**, *30*, 4242.
[61] M. Balaguer, C.-Y. Yoo, H. J. M. Bouwmeester, J. M. Serra, *J. Mat. Chem. A* **2013**, *1*, 10234.
[62] Y. A. Mastrikov, R. Merkle, E. Heifets, E. A. Kotomin, J. Maier, *J. Phys. Chem. C* **2010**, *114*, 3017.
[63] L. W. Tai, P. A. Lessing, *J. Mater. Res.* **1992**, *7*, 511.
[64] L. W. Tai, P. A. Lessing, *J. Mater. Res.* **1992**, *7*, 502.
[65] J. Fleig, S. Rodewald, J. Maier, *J. Appl. Phys.* **2000**, *87*, 2372.
[66] J. Fleig, J. Maier, *J. Eur. Ceram. Soc.* **1999**, *19*, 693.
[67] J. Crank, *The mathematics of diffusion,* Clarendon Press, Oxford, **1975**.
[68] Y.-L. Huang, C. Pellegrinelli, E. D. Wachsman, *ACS Catalysis* **2016**, *6*, 6025.
[69] J. R. McBride, K. C. Hass, B. D. Poindexter, W. H. Weber, *J. Appl. Phys.* **1994**, *76*, 2435.

[70] L. Li, F. Chen, J.-Q. Lu, M.-F. Luo, *J. Phys. Chem. A* **2011**, *115*, 7972.
[71] K. Ahn, D. S. Yoo, D. H. Prasad, H.-W. Lee, Y.-C. Chung, J.-H. Lee, *Chem. Mater.* **2012**, *24*, 4261.
[72] M. Guo, J. Lu, Y. Wu, Y. Wang, M. Luo, *Langmuir* **2011**, *27*, 3872.
[73] D. N. Durgasri, T. Vinodkumar, P. Sudarsanam, B. M. Reddy, *Catal Lett* **2014**, *144*, 971.
[74] X. Lin, S. Yan, L. Zhu, L. Li, W. Su, *Acta Chim. Sinica* **2009**, *67*, 1389.
[75] A. Bensalem, J. C. Muller, F. Bozon-Verduraz, *J. Chem. Soc., Faraday Trans.* **1992**, *88*, 153.
[76] A. Bensalem, F. Bozonverduraz, M. Delamar, G. Bugli, *Appl. Catal. A* **1995**, *121*, 81.
[77] Z.-Y. Pu, J.-Q. Lu, M.-F. Luo, Y.-L. Xie, *J. Phys. Chem. C* **2007**, *111*, 18695.
[78] G. Del Nero, G. Cappelletti, S. Ardizzone, P. Fermo, S. Gilardoni, *J. Eur. Ceram. Soc.* **2004**, *24*, 3603.
[79] L. Sandhya Kumari, P. Prabhakar Rao, M. Lakshmipathy Reddy, *J. Alloys Compd.* **2008**, *461*, 509.
[80] J. A. Badenes, J. B. Vicent, M. Llusar, M. A. Tena, G. Monr, *J. Mater. Sci.* **2002**, *37*, 1413.
[81] M. Fronzi, S. Piccinin, B. Delley, E. Traversa, C. Stampfl, *Phys. Chem. Chem. Phys.* **2009**, *11*, 9188.
[82] D. Fernandez-Torre, K. Kosmider, J. Carrasco, M. V. Ganduglia-Pirovano, R. Perez, *J. Phys. Chem. C* **2012**, *116*, 13584.
[83] D. R. Mullins, P. M. Albrecht, T.-L. Chen, F. C. Calaza, M. D. Biegalski, H. M. Christen, S. H. Overbury, *J. Phys. Chem. C* **2012**, *116*, 19419.
[84] A. Kossoy, H. Cohen, T. Bendikov, E. Wachtel, I. Lubomirsky, *Solid State Ion.* **2011**, *194*, 1.
[85] H. Y. Chen, A. Aleksandrov, Y. F. Chen, S. Zha, M. L. Liu, T. M. Orlando, *J. Phys. Chem. B* **2005**, *109*, 11257.
[86] A. L. McClellan, H. F. Harnsberger, *J. Colloid Interface Sci.* **1967**, *23*, 577.
[87] K. Yoshikawa, H. Sato, M. Kaneeda, J. N. Kondo, *J Co2 Util* **2014**, *8*, 34.
[88] K. Yoshikawa, M. Kaneeda, H. Nakamura, *Enrgy Proced* **2017**, *114*, 2481.
[89] Z. Cheng, B. J. Sherman, C. S. Lo, *J. Chem. Phys.* **2013**, *138*
[90] S.-C. Yang, W.-N. Su, J. Rick, S. D. Lin, J.-Y. Liu, C.-J. Pan, J.-F. Lee, B.-J. Hwang, *ChemSusChem* **2013**, *6*, 1326.
[91] M. J. Li, U. Tumuluri, Z. L. Wu, S. Dai, *ChemSusChem* **2015**, *8*, 3651.
[92] F. Rouquerol, J. Rouquerol, K. Sing, in *Adsorption by Powders and Porous Solids* Eds.: F. Rouquerol, J. Rouquerol, K. Sing), Academic Press, London, **1999**, p. 171.
[93] M. F. Wilkes, P. Hayden, A. K. Bhattacharya, *J. Catal.* **2003**, *219*, 286.
[94] J. Maier, *Physical Chemistry of Ionic Materials,* Wiley, Chichester, **2004**.
[95] E. Ruiz-Trejo, J. D. Sirman, Y. M. Baikov, J. A. Kilner, *Solid State Ion.* **1998**, *113-115*, 565.
[96] P. S. Manning, J. D. Sirman, J. A. Kilner, *Solid State Ion.* **1996**, *93*, 125.
[97] K. Kowalski, *Defect Diffus. Forum* **2009**, *289-292*, 769.
[98] D. P. Fagg, A. L. Shaula, V. V. Kharton, J. R. Frade, *J. Membr. Sci.* **2007**, *299*, 1.
[99] G. E. Murch, *Solid State Ion.* **1982**, *7*, 177.
[100] M. Schaube, R. Merkle, J. Maier, *J. Mat. Chem. A* **2019**, *7*, 21854.
[101] H. J. Avila-Paredes, K. Choi, C.-T. Chen, S. Kim, *J. Mater. Chem.* **2009**, *19*, 4837.
[102] L. Vegard, *Z. Phys.* **1921**, *5*, 17.
[103] R. D. Shannon, *Acta Crystallogr., Sect. A* **1976**, *32*, 751.
[104] P.-L. Chen, I.-W. Chen, *J. Am. Ceram. Soc.* **1994**, *77*, 2289.
[105] J. A. Lane, J. A. Kilner, *Solid State Ion.* **2000**, *136*, 927.

[106] D. Chen, S. R. Bishop, H. L. Tuller, *J Electroceram* **2012**, *28*, 62.
[107] T. S. Zhang, J. Ma, H. Cheng, S. H. Chan, *Mater. Res. Bull.* **2006**, *41*, 563.
[108] H. J. Avila-Paredes, K. Choi, C. T. Chen, S. Kim, *J. Mater. Chem.* **2009**, *19*, 4837.
[109] R. K. Lenka, T. Mahata, A. K. Tyagi, P. K. Sinha, *Solid State Ion.* **2010**, *181*, 262.
[110] P. P. Dholabhai, J. B. Adams, P. A. Crozier, R. Sharma, *J. Mater. Chem.* **2011**, *21*, 18991.
[111] E. N. Armstrong, K. L. Duncan, E. D. Wachsman, *Phys. Chem. Chem. Phys.* **2013**, *15*, 2298.
[112] L. Wang, R. Merkle, Y. A. Mastrikov, E. A. Kotomin, J. Maier, *J. Mater. Res.* **2012**, *27*, 2000.
[113] M. M. Kuklja, E. A. Kotomin, R. Merkle, Y. A. Mastrikov, J. Maier, *Phys. Chem. Chem. Phys.* **2013**, *15*, 5443.
[114] A. Rothschild, W. Menesklou, H. L. Tuller, E. Ivers-Tiffée, *Chem. Mater.* **2006**, *18*, 3651.
[115] V. Metlenko, W. Jung, S. R. Bishop, H. L. Tuller, R. A. De Souza, *Phys. Chem. Chem. Phys.* **2016**, *18*, 29495.
[116] A. Schmid, G. M. Rupp, J. Fleig, *Chem. Mater.* **2018**, *30*, 4242.
[117] Y. M. Choi, H. Abernathy, H. T. Chen, M. C. Lin, M. L. Liu, *ChemPhysChem* **2006**, *7*, 1957.
[118] Z. Wu, M. Li, J. Howe, H. M. Meyer, S. H. Overbury, *Langmuir* **2010**, *26*, 16595.
[119] Y. A. Mastrikov, R. Merkle, E. A. Kotomin, Maija M. Kuklja, J. Maier, *J. Mat. Chem. A* **2018**, *6*, 11929.
[120] H.-T. Chen, J.-G. Chang, H.-L. Chen, S.-P. Ju, *J. Comput. Chem.* **2009**, *30*, 2433.
[121] M. V. Anan'ev, E. K. Kurumchin, G. K. Vdovin, N. M. Bershitskaya, *Russ. J. Electrochem.* **2012**, *48*, 871.
[122] P. Simons, H. I. Ji, T. C. Davenport, S. M. Haile, *J. Am. Ceram. Soc.* **2017**, *100*, 1161.
[123] C. Nicollet, A. Flura, V. Vibhu, A. Rougier, J.-M. Bassat, J.-C. Grenier, *Int. J. Hydrogen Energy* **2016**, *41*, 15538.
[124] Y. Ma, J. D. Nicholas, *ECS Trans.* **2017**, *78*, 395.
[125] Y. Ma, J. D. Nicholas, *Phys. Chem. Chem. Phys.* **2018**, *20*, 27350.
[126] J. J. Kim, S. R. Bishop, N. J. Thompson, H. L. Tuller, *ECS Trans.* **2013**, *57*, 1979.
[127] E. Bucher, W. Sitte, F. Klauser, E. Bertel, *Solid State Ion.* **2011**, *191*, 61.
[128] L. Zhao, N. H. Perry, T. Daio, K. Sasaki, S. R. Bishop, *Chem. Mater.* **2015**, *27*, 3065.
[129] P. Mars, D. W. van Krevelen, *Chem. Eng. Sci.* **1954**, *3*, 41.
[130] M. F. Wilkes, P. Hayden, A. K. Bhattacharya, *J. Catal.* **2003**, *219*, 295.
[131] K. Yin, R. J. Davis, S. Mahamulkar, C. W. Jones, P. Agrawal, H. Shibata, A. Malek, *AlChE J.* **2017**, *63*, 725.
[132] M. Breysse, J. Veron, B. Claudel, Latreill.H, M. Guenin, *J. Catal.* **1972**, *27*, 275.
[133] Y. Liu, C. Wen, Y. Guo, G. Lu, Y. Wang, *J. Mol. Catal. A: Chem.* **2010**, *316*, 59.
[134] M. Piumetti, T. Andana, S. Bensaid, D. Fino, N. Russo, R. Pirone, *AlChE J.* **2017**, *63*, 216.
[135] X. M. Zhang, Y. Q. Deng, P. F. Tian, H. H. Shang, J. Xu, Y. F. Han, *Appl Catal B-Environ* **2016**, *191*, 179.
[136] A. Kaftan, F. Kollhoff, T.-S. Nguyen, L. Piccolo, M. Laurin, J. Libuda, *Catal. Sci. Technol.* **2016**, *6*, 818.

[137] M. Piumetti, S. Bensaid, D. Fino, N. Russo, *Appl. Catal., B* **2016**, *197*, 35.
[138] J. H. H. Termaat, M. P. Vandijk, G. Roelofs, H. Bosch, G. M. H. Vandevelde, P. J. Gellings, A. J. Burggraaf, *Mater. Res. Bull.* **1984**, *19*, 1271.
[139] B. Liu, W. Li, W. Song, J. Liu, *Phys. Chem. Chem. Phys.* **2018**, *20*, 16045.
[140] F. Chen, D. Liu, J. Zhang, P. Hu, X.-Q. Gong, G. Lu, *Phys. Chem. Chem. Phys.* **2012**, *14*, 16573.
[141] T. Kropp, M. Mavrikakis, *J. Catal.* **2019**, *377*, 577.
[142] Y. G. Wang, D. H. Mei, J. Li, R. Rousseau, *J. Phys. Chem. C* **2013**, *117*, 23082.
[143] H. Li, G. Lu, Y. Wang, Y. Guo, Y. Guo, *Catal. Commun.* **2010**, *11*, 946.
[144] E. Ramírez-Cabrera, A. Atkinson, D. Chadwick, *Appl. Catal., B* **2002**, *36*, 193.
[145] D. Knapp, T. Ziegler, *J. Phys. Chem. C* **2008**, *112*, 17311.
[146] D. R. Mullins, *Surf. Sci. Rep.* **2015**, *70*, 42.
[147] A. Salcedo, I. Iglesias, F. Marino, B. Irigoyen, *Appl. Surf. Sci.* **2018**, *458*, 397.
[148] M. Fronzi, S. Piccinin, B. Delley, E. Traversa, C. Stampfl, *RSC Adv.* **2014**, *4*, 12245.
[149] K. J. Warren, J. R. Scheffe, *J. Phys. Chem. C* **2019**, *123*, 13208.
[150] D. Haffad, A. Chambellan, J. C. Lavalley, *J Mol Catal a-Chem* **2001**, *168*, 153.
[151] S. Bernal, R. Garcia, F. Ramirez, J. M. Rodriguezizquierdo, *Z Phys Chem Neue Fol* **1983**, *138*, 229.
[152] M. J. Kang, J. F. DeWilde, A. Bhan, *Acs Catalysis* **2015**, *5*, 602.
[153] H. Noller, W. Kladnig, *Catal Rev* **1976**, *13*, 149.
[154] W. Turek, A. Krowiak, *Appl. Catal. A* **2012**, *417*, 102.
[155] L. Nondek, J. Sedlacek, *J. Catal.* **1975**, *40*, 34.
[156] M. I. Zaki, N. Sheppard, *J. Catal.* **1983**, *80*, 114.
[157] A. Ouqour, G. Coudurier, J. C. Vedrine, *J. Chem. Soc. Faraday Trans.* **1993**, *89*, 3151.
[158] M. W. den Otter, B. A. Boukamp, H. J. M. Bouwmeester, *Solid State Ion.* **2001**, *139*, 89.

APPENDIX

Appendix 1: Derivation of M1 and M2

The treatment here largely follows the procedure in refs. [54, 55, 158] (however, please note that here ${}^{1}\Re_{\mathrm{da}}$ is given in units of oxygen molecules per unit time and surface area, not atoms). The following reaction mechanism at equilibrium with $p(O_2)$ is assumed:

$$O_2 \underset{\overleftarrow{k}_{\mathrm{da}}}{\overset{\vec{k}_{\mathrm{da}}}{\rightleftharpoons}} 2O_{\mathrm{ad}}^{-} + 2h^{\bullet} \qquad K_{\mathrm{ad}} = \frac{\vec{k}_{\mathrm{da}}}{\overleftarrow{k}_{\mathrm{da}}} = \frac{\widehat{[O_{\mathrm{ad}}^{-}]}^{2}\widehat{[h^{\bullet}]}^{2}}{\widehat{[O_2]}} \qquad \text{eq. 57}$$

$$O_{\mathrm{ad}}^{-} + V_O^{\bullet\bullet} \underset{\overleftarrow{k}_{\mathrm{i}}}{\overset{\vec{k}_{\mathrm{i}}}{\rightleftharpoons}} O_O^{\mathrm{x}} + h^{\bullet} \qquad K_{\mathrm{i}} = \frac{\vec{k}_{\mathrm{i}}}{\overleftarrow{k}_{\mathrm{i}}} = \frac{\widehat{[O_O^{\mathrm{x}}]}\widehat{[h^{\bullet}]}}{\widehat{[O_{\mathrm{ad}}^{-}]}\widehat{[V_O^{\bullet\bullet}]}} \qquad \text{eq. 58}$$

Square brackets indicate concentrations and $\widehat{\ }$ denotes values in equilibrium. Since in equilibrium the forward and back reaction rates are equal the equilibrium exchange rates for dissociative-adsorption (${}^{1}\Re_{\mathrm{da}}$) and incorporation (${}^{1}\Re_{\mathrm{i}}$) can be defined:

$${}^{1}\Re_{\mathrm{da}} = \vec{k}_{\mathrm{da}}\widehat{[O_2]} = \overleftarrow{k}_{\mathrm{da}}\widehat{[O_{\mathrm{ad}}^{-}]}^{2}\widehat{[h^{\bullet}]}^{2} \qquad \text{eq. 59}$$

$${}^{1}\Re_{\mathrm{i}} = \vec{k}_{\mathrm{i}}\widehat{[O_{\mathrm{ad}}^{-}]}\widehat{[V_O^{\bullet\bullet}]} = \overleftarrow{k}_{\mathrm{i}}\widehat{[O_O^{\mathrm{x}}]}\widehat{[h^{\bullet}]} \qquad \text{eq. 60}$$

During the reaction, mass is conserved and for oxygen isotopologues eq. 61 – eq. 63 hold.

$$\widehat{[O_2]} = [{}^{36}O_2] + [{}^{34}O_2] + [{}^{32}O_2] \qquad \text{eq. 61}$$

$$[{}^{18}O_{\mathrm{g}}] = 2[{}^{36}O_2] + [{}^{34}O_2] \qquad \text{eq. 62}$$

$$[{}^{18}O_{\mathrm{ad}}] = [{}^{18}O_{\mathrm{tot}}] - [{}^{18}O_{\mathrm{g}}] - [{}^{18}O_O^{\mathrm{x}}] \qquad \text{eq. 63}$$

The consumption of ${}^{36}O_2$, ${}^{32}O_2$ and ${}^{18}O_O^{\mathrm{x}}$ (in molecules/atoms per unit time (t) and surface area (S)) can be directly formulated by considering eq. 57 and eq. 58.

$$\frac{1}{S}\frac{d\left[{}^{36}O_2\right]}{dt} = -\vec{k}_{da}\left[{}^{36}O_2\right] + \overleftarrow{k}_{da}\left[{}^{18}O_{ad}^{-}\right]^2[\widehat{h^{\bullet}}]^2 \qquad \text{eq. 64}$$

$$\frac{1}{S}\frac{d\left[{}^{32}O_2\right]}{dt} = -\vec{k}_{da}\left[{}^{32}O_2\right] + \overleftarrow{k}_{da}\left[{}^{16}O_{ad}^{-}\right]^2[\widehat{h^{\bullet}}]^2 \qquad \text{eq. 65}$$

$$\frac{1}{S}\frac{d\left[{}^{18}O_O^{x}\right]}{dt} = \vec{k}_{i}\left[{}^{18}O_{ad}\right][\widehat{V_O^{\bullet\bullet}}] - \overleftarrow{k}_{i}\left[{}^{18}O_O^{x}\right][\widehat{h^{\bullet}}] \qquad \text{eq. 66}$$

Inserting eq. 57 and eq. 58 into the corresponding rate laws of eq. 64 – eq. 66 and considering the definition of the equilibrium exchange rates in eq. 59 and eq. 60 yields eq. 67 – eq. 69.

$$\frac{1}{S}\frac{d\left[{}^{36}O_2\right]}{dt} = {}^{1}\Re_{da}\left(\frac{\left[{}^{36}O_2\right]}{\widehat{[O_2]}} - \frac{\left[{}^{18}O_{ad}^{-}\right]^2}{\widehat{\left[O_{ad}^{-}\right]}^2}\right) \qquad \text{eq. 67}$$

$$\frac{1}{S}\frac{d\left[{}^{32}O_2\right]}{dt} = {}^{1}\Re_{da}\left(\frac{\left[{}^{32}O_2\right]}{\widehat{[O_2]}} - \frac{\left[{}^{16}O_{ad}^{-}\right]^2}{\widehat{\left[O_{ad}^{-}\right]}^2}\right) \qquad \text{eq. 68}$$

$$\frac{1}{S}\frac{d\left[{}^{18}O_O^{x}\right]}{dt} = {}^{1}\Re_{i}\left(\frac{\left[{}^{18}O_{ad}\right]}{\widehat{\left[O_{ad}^{-}\right]}} - \frac{\left[{}^{18}O_O^{x}\right]}{\widehat{[O_O^{x}]}}\right) \qquad \text{eq. 69}$$

Introducing the oxygen isotope fractions ${}^{18}f_{lat}$, ${}^{18}f_{ad}$, ${}^{32}f_g$ and ${}^{36}f_g$, eq. 67 – eq. 69. can be simplified (for the sake of simplicity the indicator for equilibrium values ($\widehat{\ }$) will be omitted from now on):

$$\frac{d\,{}^{36}f_g}{dt} = \frac{{}^{1}\Re_{da}S}{[O_2]}\left({}^{36}f_g - {}^{18}f_{ad}^2\right) \qquad \text{eq. 70}$$

$$\frac{d\,{}^{32}f_g}{dt} = \frac{{}^{1}\Re_{da}S}{[O_2]}\left({}^{36}f_g - {}^{18}f_{ad}^2\right) \qquad \text{eq. 71}$$

$$\frac{d\,{}^{18}f_{lat}}{dt} = \frac{{}^{1}\Re_{i}S}{[O_O^{x}]}\left({}^{18}f_{ad} - {}^{18}f_{lat}\right) \qquad \text{eq. 72}$$

The rate law for ${}^{34}f_g$ is obtained by considering eq. 61 and ${}^{16}f_{ad} = 1 - {}^{18}f_{ad}$:

$$\frac{d\,{}^{34}f_g}{dt} = -\frac{d\,{}^{36}f_g}{dt} - \frac{d\,{}^{32}f_g}{dt} = \frac{{}^{1}\Re_{da}S}{[O_2]}\left({}^{34}f_g - 2\,{}^{18}f_{ad}\left(1 - {}^{18}f_{ad}\right)\right) \qquad \text{eq. 73}$$

The isotope conservation in the gas phase (eq. 62) can be rewritten as

$$\frac{d^{18}f_{\mathrm{g}}}{dt} = \frac{d^{36}f_{\mathrm{g}}}{dt} + \frac{1}{2}\frac{d^{34}f_{\mathrm{g}}}{dt} \qquad \text{eq. 74}$$

Substitution of eq. 70 and eq. 73 into eq. 74 yields the ^{18}O consumption in the gas phase:

$$\frac{d^{18}f_{\mathrm{ad}}}{dt} = -\frac{[\mathrm{O_O^x}]}{[\mathrm{O_{ad}}]}\frac{d^{18}f_{\mathrm{lat}}}{dt} - \frac{2[\mathrm{O_2}]}{[\mathrm{O_{ad}}]}\frac{d^{18}f_{\mathrm{g}}}{dt} \qquad \text{eq. 75}$$

$$\frac{d^{18}f_{\mathrm{ad}}}{dt} = -\frac{^{1}\Re_{\mathrm{i}}S}{[\mathrm{O_{ad}}]}\left(^{18}f_{\mathrm{ad}} - {}^{18}f_{\mathrm{lat}}\right) + \frac{^{1}\Re_{\mathrm{da}}S}{[\mathrm{O_{ad}}]}\left(2\,^{18}f_{\mathrm{g}} - 2\,^{18}f_{\mathrm{ad}}\right) \qquad \text{eq. 76}$$

Assuming that $[^{18}\mathrm{O_{ad}}]$ is at steady-state, eq. 76 turns into eq. 77:

$$^{18}f_{ad} = \frac{^{1}\Re_{\mathrm{i}}\,^{18}f_{lat} + 2\,^{1}\Re_{\mathrm{da}}\,^{18}f_{g}}{^{1}\Re_{\mathrm{i}} + 2\,^{1}\Re_{\mathrm{da}}} \qquad \text{eq. 77}$$

Substitution of eq. 77 into eq. 74 and assuming that $^{18}f_{\mathrm{lat}} \approx 0$ yields an expression for $^{18}f_{\mathrm{g}}$ in terms of the effective overall equilibrium exchange rate $^{1}\Re_{0}$:

$$\frac{d^{18}f_{\mathrm{g}}}{dt} = -\frac{^{1}\Re_{\mathrm{da}}S}{2[\mathrm{O_2}]}\left(2\,^{18}f_{\mathrm{g}} - 2\left(\frac{2\,^{1}\Re_{\mathrm{da}}\,^{18}f_{g}}{^{1}\Re_{\mathrm{i}} + 2\,^{1}\Re_{\mathrm{da}}}\right)\right) = -\frac{S\,^{1}\Re_{0}}{2[\mathrm{O_2}]}\,^{18}f_{g} \qquad \text{eq. 78}$$

$$^{1}\Re_{0} = \frac{2\Re_{\mathrm{a}}\Re_{\mathrm{i}}}{\Re_{\mathrm{i}} + 2\Re_{\mathrm{a}}} \qquad \text{eq. 79}$$

The equation in eq. 78 can be solved by integration from $t = 0$ to $t = \tau_{\mathrm{r}}$, where τ_{r} defines the residence time of the pulse, yielding eq. 80:

$$^{18}f_{\mathrm{g,e}} = {}^{18}f_{\mathrm{g,i}}\exp\left(-\frac{^{1}\Re_{0}S\tau_{\mathrm{r}}}{n_{\mathrm{O}}}\right) \quad \Leftrightarrow \quad \Re_{0} = \frac{n_{\mathrm{O}}}{S\tau_{\mathrm{r}}}\ln\left(\frac{^{18}f_{\mathrm{g,i}}}{^{18}f_{\mathrm{g,e}}}\right) \qquad \text{eq. 80}$$

In order to calculate $^{1}\Re_{\mathrm{da}}$ and $^{1}\Re_{\mathrm{i}}$ from measured isotope fractions, one has to find an expression for $^{36}f_{\mathrm{g}}(t)$, which can be obtained by substitution of eq. 77 and eq. 80 into eq. 70 and subsequent integration, assuming again that $^{18}f_{\mathrm{lat}} \approx 0$. eq. 81 can then be solved numerically to obtain $^{1}\Re_{\mathrm{i}}$.

$$ {}^{36}f_{\mathrm{g,e}} = B\exp\left(\frac{-2\tau_{\mathrm{r}}S\ {}^{1}\Re_{0}}{n_{\mathrm{O}}}\right) + \left({}^{36}f_{\mathrm{g,i}} - B\right)\exp\left(\frac{\tau_{\mathrm{r}}S\ {}^{1}\Re_{0}\ {}^{1}\Re_{\mathrm{i}}}{\left({}^{1}\Re_{0} - {}^{1}\Re_{\mathrm{i}}\right)n_{\mathrm{O}}}\right) $$

$$ B = \frac{\left({}^{18}f_{\mathrm{g,i}}\ {}^{1}\Re_{0}\right)^{2}}{{}^{1}\Re_{\mathrm{i}}\left(2\ {}^{1}\Re_{0} - {}^{1}\Re_{\mathrm{i}}\right)} \qquad \text{eq. 81} $$

For the mechanism M2, the following reaction mechanism at equilibrium is assumed:

$$ \mathrm{O_2} + \mathrm{V_O^{\bullet\bullet}} \underset{\overleftarrow{k}_{\mathrm{da}}}{\overset{\vec{k}_{\mathrm{da}}}{\rightleftharpoons}} \mathrm{O_{ad}^{-}} + \mathrm{O_O^{x}} + 3h^{\bullet} \qquad K_{\mathrm{da}} = \frac{\vec{k}_{\mathrm{da}}}{\overleftarrow{k}_{\mathrm{da}}} = \frac{\widehat{[\mathrm{O_{ad}^{-}}]}\widehat{[\mathrm{O_O^{x}}]}\widehat{[h^{\bullet}]^{3}}}{\widehat{[\mathrm{O_2}]}\widehat{[\mathrm{V_O^{\bullet\bullet}}]}} \qquad \text{eq. 82} $$

$$ \mathrm{O_{ad}^{-}} + \mathrm{V_O^{\bullet\bullet}} \underset{\overleftarrow{k}_{\mathrm{i}}}{\overset{\vec{k}_{\mathrm{i}}}{\rightleftharpoons}} \mathrm{O_O^{x}} + h^{\bullet} \qquad K_{\mathrm{i}} = \frac{\vec{k}_{\mathrm{i}}}{\overleftarrow{k}_{\mathrm{i}}} = \frac{\widehat{[\mathrm{O_O^{x}}]}\widehat{[h^{\bullet}]}}{\widehat{[\mathrm{O_{ad}^{-}}]}\widehat{[\mathrm{V_O^{\bullet\bullet}}]}} \qquad \text{eq. 83} $$

The equilibrium exchange rates for dissociative-adsorption (${}^{2}\Re_{\mathrm{da}}$) and incorporation (${}^{2}\Re_{\mathrm{i}}$) can be defined as:

$$ {}^{2}\Re_{\mathrm{da}} = \vec{k}_{\mathrm{da}}\widehat{[\mathrm{O_2}]}\widehat{[\mathrm{V_O^{\bullet\bullet}}]} = \overleftarrow{k}_{\mathrm{da}}\widehat{[\mathrm{O_{ad}^{-}}]}\widehat{[\mathrm{O_O^{x}}]}\widehat{[h^{\bullet}]^{3}} \qquad \text{eq. 84} $$

$$ {}^{2}\Re_{\mathrm{i}} = \vec{k}_{\mathrm{i}}\widehat{[\mathrm{O_{ad}^{-}}]}\widehat{[\mathrm{V_O^{\bullet\bullet}}]} = \overleftarrow{k}_{\mathrm{i}}\widehat{[\mathrm{O_O^{x}}]}\widehat{[h^{\bullet}]} \qquad \text{eq. 85} $$

Applying the same approach as above, the following key equations are obtained:

$$ \frac{d\,{}^{36}f_{\mathrm{g}}}{dt} = \frac{{}^{2}\Re_{\mathrm{da}}S}{[\mathrm{O_2}]}\left({}^{36}f_{\mathrm{g}} - {}^{18}f_{\mathrm{ad}}\,{}^{18}f_{\mathrm{lat}}\right) \qquad \text{eq. 86} $$

$$ \frac{d\,{}^{32}f_{\mathrm{g}}}{dt} = \frac{{}^{2}\Re_{\mathrm{da}}S}{[\mathrm{O_2}]}\left({}^{32}f_{\mathrm{g}} - {}^{16}f_{\mathrm{ad}}\,{}^{16}f_{\mathrm{lat}}\right) \qquad \text{eq. 87} $$

$$ \frac{d\,{}^{18}f_{\mathrm{lat}}}{dt} = \frac{{}^{2}\Re_{\mathrm{i}}S}{[\mathrm{O_O^{x}}]}\left({}^{18}f_{\mathrm{ad}} - {}^{18}f_{\mathrm{lat}}\right) + \frac{{}^{2}\Re_{\mathrm{da}}S}{[\mathrm{O_O^{x}}]}\left({}^{18}f_{\mathrm{g}} - {}^{18}f_{\mathrm{lat}}\right) \qquad \text{eq. 88} $$

$$ \frac{d\,{}^{34}f_{\mathrm{g}}}{dt} = -\frac{{}^{2}\Re_{\mathrm{da}}S}{[\mathrm{O_2}]}\left({}^{34}f_{\mathrm{g}} - {}^{18}f_{\mathrm{ad}} - {}^{18}f_{\mathrm{lat}}\right) \qquad \text{eq. 89} $$

$$ \frac{d\,{}^{18}f_{\mathrm{g}}}{dt} = -\frac{{}^{2}\Re_{\mathrm{da}}S}{2[\mathrm{O_2}]}\left(2\,{}^{18}f_{\mathrm{g}} - {}^{18}f_{\mathrm{lat}} - {}^{18}f_{\mathrm{ad}}\right) \qquad \text{eq. 90} $$

$$ \frac{d\,{}^{18}f_{\mathrm{ad}}}{dt} = -\frac{{}^{2}\Re_{\mathrm{i}}S}{[\mathrm{O_{ad}}]}\left({}^{18}f_{\mathrm{ad}} - {}^{18}f_{\mathrm{lat}}\right) + \frac{{}^{2}\Re_{\mathrm{da}}S}{[\mathrm{O_{ad}}]}\left({}^{18}f_{\mathrm{g}} - {}^{18}f_{\mathrm{ad}}\right) \qquad \text{eq. 91} $$

$$^{18}f_{ad} = \frac{^{2}\Re_i \, ^{18}f_{lat} + \, ^{2}\Re_{da} \, ^{18}f_g}{^{2}\Re_i + \, ^{2}\Re_{da}} \qquad \text{eq. 92}$$

$$\frac{d\,^{18}f_g}{dt} = -\frac{^{2}\Re_0 S}{2[O_2]} \, ^{18}f_g \qquad \text{eq. 93}$$

$$^{2}\Re_0 = \, ^{2}\Re_{da}\left(1 + \frac{^{2}\Re_i}{^{2}\Re_i + \, ^{2}\Re_{da}}\right) \qquad \text{eq. 94}$$

Since $^{18}f_{lat} \approx 0$, the approach to find a solution for eq. 86 is simple and yields:

$$^{36}f_{g,e} = \, ^{36}f_{g,i} \exp\left(-\frac{^{2}\Re_{da} S \tau_r}{[O_2]}\right) \quad \Leftrightarrow \quad ^{2}\Re_{da} = \frac{[O_2]}{S\tau_r} \ln\left(\frac{^{36}f_{g,i}}{^{36}f_{g,e}}\right) \qquad \text{eq. 95}$$

This equation shows clearly that when no $^{34}O_2$ is formed, because $^{2}\Re_i$ is much faster than $^{2}\Re_{da}$, i.e. $^{36}f_g$ and $^{18}f_{g,i}$ are identical, $^{2}\Re_{da}$ becomes identical to $\Re_0$ (eq. 18 main text). Assuming that $^{2}\Re_{da}$ in eq. 94 becomes significantly lower than $^{2}\Re_i$ the equilibrium exchange rate yields $\Re_0 \approx 2 \, ^{2}\Re_{da}$, and the values of $^{2}\Re_i$ determined from this equation acquire huge error bars.

Appendix 2: Curriculum Vitae

Personal Information

Name:	Maximilian Schaube
Date of birth:	20. June 1987
Place of birth:	Haselünne, Lower Saxony, Germany
E–Mail:	mail@maximilian-schaube.de

Education

2015–2020	Ph.D., Physical Chemistry of Solids Max–Planck–Institute for Solid State Research, Stuttgart
2010–2015	B.Sc. & M.Sc. Chemistry Carl von Ossietzky Universität, Oldenburg
2004–2007	Certificate of Chamber of Industry and Commerce Chemical Laboratory Technician Remmers Gruppe AG, Löningen

Publications

2019	Oxygen Exchange Kinetics on Systematically Doped Ceria: A Pulsed Isotope Exchange Study *M. Schaube, R. Merkle, J. Maier* Journal of Materials Chemistry A, **2019**, 7, 21854
2019	Point Defects and CO Oxidation Kinetics: A Study on Systematically Doped Ceria *submitted*